NASA Contractor Report 4685

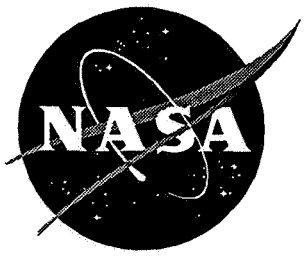

Low-Speed Wind-Tunnel Investigation of a Porous Forebody and Nose Strakes for Yaw Control of a Multirole Fighter Aircraft

Scott P. Fears

Contract NAS1-19000
Prepared for Langley Research Center

August 1995

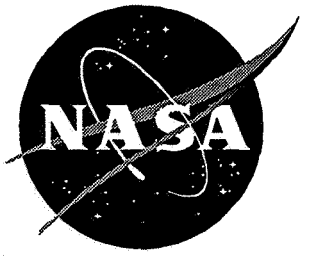

NASA Contractor Report 4685

Low-Speed Wind-Tunnel Investigation of a Porous Forebody and Nose Strakes for Yaw Control of a Multirole Fighter Aircraft

Scott P. Fears
Lockheed Engineering & Sciences Company • Hampton, Virginia

National Aeronautics and Space Administration
Langley Research Center • Hampton, Virginia 23681-0001

Prepared for Langley Research Center
under Contract NAS1-19000

August 1995

Printed copies available from the following:

NASA Center for AeroSpace Information
800 Elkridge Landing Road
Linthicum Heights, MD 21090-2934
(301) 621-0390

National Technical Information Service (NTIS)
5285 Port Royal Road
Springfield, VA 22161-2171
(703) 487-4650

Summary

Low-speed wind-tunnel tests were conducted in the Langley 12-Foot Low-Speed Tunnel on a model of the Boeing Multirole Fighter (BMRF) aircraft. This single-seat, single-engine configuration was intended to be an F-16 replacement that would incorporate many of the design goals and advanced technologies of the F-22. Its mission requirements included supersonic cruise without afterburner, reduced observability, and the ability to attack both air-to-air and air-to-ground targets. So that it would be effective in all phases of air combat, the ability to maneuver at angles of attack up to and beyond maximum lift was also desired. Traditional aerodynamic yaw controls, such as rudders, are typically ineffective at these higher angles of attack because they are usually located in the wake from the wings and fuselage. For this reason, this study focused on investigating forebody-mounted controls that produce yawing moments by modifying the strong vortex flowfield being shed from the forebody at these high angles of attack. Two forebody strakes were tested that varied in planform and chordwise location. Various patterns of porosity in the forebody skin were also tested that differed in their radial coverage and chordwise location. The tests were performed at a dynamic pressure of 4 lb/ft^2 over an angle-of-attack range of -4° to 72° and a sideslip range of -10° to 10°. Static force data, static pressures on the surface of the forebody, and flow-visualization using laser-illuminated smoke were obtained.

Both the strakes and porous forebody generated yawing moments at angles of attack above maximum lift that were equal to or better than the low-angle-of-attack rudder effectiveness. The porous forebody generated yawing moments when the portion of the porosity pattern on the upper surfaces of the forebody was asymmetric between the left and right sides of the model. These yawing moments could be modulated by varying the radial coverage of the porosity. The effectiveness of either the strakes or porosity was increased by locating the control farther forward on the forebody, and both the strakes and porous forebody remained effective when at sideslip. The presence of the vertical tails caused small reductions in the yaw control produced by the strakes but resulted in slight improvements in the effectiveness of the porous forebody.

All the effective yaw-control concepts altered the forebody vortex flowfield such that it was highly asymmetric between the left and right sides of the model. These controls typically reduced the suction pressures on the side on which they were deployed, and the suction on the other side was generally maintained or increased slightly. The resultant side force caused a yawing moment away from the side containing the control.

The combination of rudder deflections at low angles of attack and asymmetric forebody skin porosity at high angles of attack gave this configuration good levels of yaw control for a large portion of the test angle-of-attack range. But at the intermediate angles of attack around maximum lift, neither of these controls was very effective, and a region of diminished yaw control existed that may limit the maneuverability of this design.

Introduction

The advent of technologies such as thrust vectoring, advanced aerodynamic controls, and digital flight control laws has enabled new fighter aircraft to achieve unprecedented levels of maneuverability. When used in combination, these new capabilities can give the resulting fighter a very high level of agility about all axes that may include the ability to fly at angles of attack well beyond maximum lift. The tactical utility of these highly agile aircraft has been investigated using flight simulators for the past two decades (refs. 1 to 4). Recent flight tests of the F-16MATV (F-16 Multi-Axis Thrust Vectoring), X-31, and NASA F-18 HARV (High-Angle-of-Attack Research Vehicle) have also begun to investigate how high agility can be used effectively during air combat. Both the simulation studies and flight tests have shown that high agility can provide an advantage during the close-in arena of air combat, especially at the shorter ranges and slower speeds where guns are typically employed. As a result, the desire for high agility has influenced most new fighter designs (i.e., the F-22 that has thrust vectoring and digital control laws).

For a fighter to achieve angles of attack beyond maximum lift, it must have powerful pitch controls that remain effective for all the angles of attack that will be encountered. Some of this control power may be provided by thrust vectoring, but sufficient aerodynamic control to recover from an extreme angle of attack is often desired to protect the aircraft in case of a loss of engine power. To take full advantage of these high angles of attack, the fighter must also possess good lateral-directional control throughout its flight envelope. Powerful yaw controls are needed to minimize the sideslip caused by kinematic and inertial coupling that may occur during rolls at high angles of attack (fig. 1). They may also be required to prevent a departure or a spin entry. Thrust vectoring may be used to obtain yawing moments. But similar to the pitch axis, some degree of aerodynamic yaw control is usually desired as a safety-of-flight consideration.

Aerodynamic yaw control at high angles of attack is often difficult to obtain by using traditional methods (ref. 5). A rudder usually provides reduced or negligible yaw control at high angles of attack because it is typically located in the low-energy wake of the wings and fuselage (fig. 1). In contrast, the forebody is immersed in the freestream flow and often produces powerful vortex flowfields, especially for modern fighters with sharp chines that result from reduced-radar-cross-section considerations. If modified into an asymmetric pattern, these vortex flowfields may be capable of generating significant side forces on the forebody along with corresponding yawing moments. In addition, the forebody often has a long directional moment arm because many modern fighters have a farther aft c.g. that is required for reduced static longitudinal stability (fig. 2). For these reasons, devices that are designed to produce yawing moments by altering the forebody vortex flowfield are currently being investigated at high angles of attack as alternatives to conventional aerodynamic yaw controls.

Depending on the overall aircraft configuration, several potential problems exist that may occur when attempting to use a given type of forebody control. As stated previously, these devices produce control moments by modifying the vortex flowfield produced by the forebody. These changes in the flow may occur abruptly as angle of attack is varied or the character of the control device is altered. As a result, modulating the control moment produced by a given forebody control concept may be difficult. Another potential problem that may occur relates to the performance of the fighter's radar that is normally mounted in the nose cone. Any metallic hardware associated with a forebody control that is forward of the radar has the potential of interfering with the desired antenna scan pattern. For this reason, aircraft designers typically wish to locate the forebody controls as far aft as possible. In contrast, a more forward location is usually desirable for maximum aerodynamic effectiveness. As a result, a design challenge exists to formulate a device that produces the necessary aerodynamic control without detrimentally affecting the performance of the radar.

The aircraft investigated during the subject study was a multirole fighter configuration (BMRF) that was designed by the Boeing Military Aircraft Company (fig. 3). This aircraft was intended to be a replacement for the F-16. As a result, its mission requirements included both air-to-air and air-to-ground capabilities. So that it would complement the F-22, it was desired that the BMRF should share many of the F-22's design goals and advanced technologies. The resulting layout was a single-seat, single-engine configuration that incorporated an internal weapons bay and a thrust-vectoring/thrust-reversing nozzle. The design was also strongly influenced by the requirements for super-cruise (supersonic cruise without afterburner) and reduced observability. In efforts to maximize the agility level of the aircraft, the effectiveness of several yaw-control concepts was investigated during low-speed wind-tunnel tests. These devices consisted of forebody strakes of different shapes and locations and various patterns of porosity in the forebody skin. This report summarizes the low-speed effectiveness of these yaw-control concepts.

Symbols

All longitudinal forces and moments are referred to the stability-axis system, and all lateral-directional forces and moments are referred to the body-axis system. All the aerodynamic data is referred to a moment reference center that was located longitudinally 44 inches (FS 59.375) aft of the nose at a vertical position of WL 17.0625 (fig. 3).

b wing span, ft or in.

C_L lift coefficient, $\frac{\text{Lift force}}{\bar{q}S}$

C_l rolling-moment coefficient, $\frac{\text{Rolling moment}}{\bar{q}Sb}$

C_m pitching-moment coefficient, $\frac{\text{Pitching moment}}{\bar{q}S\bar{c}}$

C_n yawing-moment coefficient, $\frac{\text{Yawing moment}}{\bar{q}Sb}$

C_p static surface pressure coefficient, $\frac{p_l - p_s}{\bar{q}}$

C_Y side-force coefficient, $\frac{\text{Side force}}{\bar{q}S}$

$\bar{c}$ mean aerodynamic chord, ft or in.

d_l distance around one half of lower surface of forebody cross section, used to define Φ_p (see fig. 9)

d_u distance around one half of upper surface of forebody cross section, used to define Φ_p (see fig. 9)

l_{pf} total chordwise length of porous section of forebody, 8.25 in. (see fig. 9)

p_l local static pressure measured at given pressure port, psi

p_s free-stream static pressure, psi

$\bar{q}$ free-stream dynamic pressure, lb / ft^2 or psi

S reference area, ft^2 or in^2

X longitudinal body axis (see fig. 3)

X_p chordwise location of region of forebody porosity, expressed in percentage of length of porous nose piece (l_{pf}), 0% corresponded to tip of forebody and 100% corresponded to aft end of porous nose piece (see fig. 9)

Y lateral body axis (see fig. 3)

Z vertical body axis (see fig. 3)

α angle of attack, deg

β angle of sideslip, deg

ΔC_l incremental rolling-moment coefficient, $C_{l_{\text{control deflected}}} - C_{l_{\text{control undeflected}}}$

ΔC_n incremental yawing-moment coefficient, $C_{n_{\text{control deflected}}} - C_{n_{\text{control undeflected}}}$

ΔC_Y incremental side-force coefficient, $C_{Y_{\text{control deflected}}} - C_{Y_{\text{control undeflected}}}$

δ_a aileron deflection angle, positive with trailing edge down, measured normal to hinge line, deg

δ_L leading-edge flap deflection angle, positive with leading edge down, measured normal to hinge line, deg

δ_r rudder deflection angle, positive with trailing edge left, deg

Φ_p radial location of region of forebody porosity, described using clock face positions when looking downstream (see fig. 9)

Derivatives:

C_{l_β} lateral stability parameter, $\frac{\partial C_l}{\partial \beta}$, $\frac{C_{l_{(\beta=5)}} - C_{l_{(\beta=-5)}}}{10}$, per deg

C_{n_β} directional stability parameter, $\frac{\partial C_n}{\partial \beta}$, $\frac{C_{n_{(\beta=5)}} - C_{n_{(\beta=-5)}}}{10}$, per deg

C_{Y_β} side force parameter, $\frac{\partial C_Y}{\partial \beta}$, $\frac{C_{Y_{(\beta=5)}} - C_{Y_{(\beta=-5)}}}{10}$, per deg

Abbreviations:

BL	butt line
BMRF	Boeing Multirole Fighter
ESP	electronically sensed pressure
FS	fuselage station
HARV	High-Angle-of-Attack Research Vehicle
L.E.D.	leading edge down
MATV	Multi-Axis Thrust Vectoring
RSS	relaxed static stability
T.E.D.	trailing edge down
T.E.L.	trailing edge left
T.E.R.	trailing edge right
T.E.U.	trailing edge up
VG3	aft-mounted forebody strake
VG6	fore-mounted forebody strake
WL	waterline

Model Description

An aluminum model of the BMRF was constructed using an NC-machine. The BMRF configuration consisted of a fuselage with sharp nose chines, a chin-mounted inlet, modified delta wings that were drooped down at a dihedral angle of -10°, horizontal tails, and twin vertical tails that were canted outward 30° (fig. 3). Figure 4 shows a detailed drawing of the wing planform, and figure 5 shows the dimensions of the horizontal and vertical tails. Photographs of the model are shown in figure 6, and the geometric characteristics are summarized in table 1.

The wings had leading-edge flaps and trailing-edge flaps for improved longitudinal characteristics at high angles of attack (fig. 4). The leading-edge flaps were tested at deflection angles of 0° and 30° (L.E.D.), but the trailing-edge flaps were not deflected during the subject tests. To obtain roll control, the wings had conventional ailerons that were tested at deflection angles between 30° (T.E.D.) and -45° (T.E.U.).

The twin vertical tails incorporated rudders for yaw control (figs. 3 and 5(b)). To provide a comparison to the effectiveness of the forebody yaw controls, the rudders were tested at a deflection angle of -30°. The configuration had conventional all-moving horizontal tails for pitch control (figs. 3 and 5(a)). The horizontal tails were not deflected during these tests because this study was primarily concerned with lateral-directional control.

Two forebody strakes (VG3 and VG6) were tested by simply bolting or taping them to the model (fig. 7). These strakes were intended to be deployed on only one side of the aircraft at a time, depending on the direction of the desired control. The VG3 strake planform, location, and deflection scheme were formulated by Boeing during the original configuration design. To minimize interference with the fighter's

radar, the VG3 was located aft of the nose cone. When not in use, this strake was intended to fold upwards and lie flush with the fuselage contour. The VG3 was tested at a deflection angle of 45° out from the vertical (fig. 7(a)). The VG6 strake was located at the tip of the nose to determine if a farther forward strake would be more effective on the BMRF configuration. The curved planform of the VG6 was intended to model a strake that would pivot outwards about a hinge point at the tip of the nose (fig. 7(b)). The VG6 was mounted such that it extended straight out from the chine line with no upward or downward deflection. The VG6 was tested on both the right and left sides of the model.

To test the effects of forebody porosity, the original solid nose of the model was replaced with a similarly shaped piece that had a porous outer skin and an inner solid section located 0.2 inches beneath the surface (fig. 8). The porous skin contained approximately 1089 0.016-inch-diameter holes per square inch, which corresponded to a porosity value of 22 percent. The chordwise length of the new nose (l_{pf}) was 8.25 inches. To obtain regions of asymmetric porosity, the areas that were not desired to be porous were sealed with tape. The resulting regions of porosity were described by a chordwise location (X_p) and a radial coverage (Φ_p). Figure 9 illustrates the nomenclature used to describe the forebody porosity regions, and figure 10 shows the radial and chordwise coverages of the porosity regions that were tested. The endpoints of the chordwise location (X_p) of the porous region were described as percentages of the total length of the porous nose (l_{pf}). The tip of the nose corresponded to $X_p=0\%l_{pf}$, and the aft edge of the porous nose corresponded to $X_p=100\%l_{pf}$. The endpoints of the radial coverage of the porous region (Φ_p) were described in a clockwise direction using clock face positions when looking downstream. The Φ_p's of 3, 6, 9, and 12 corresponded respectively to the left chine, bottom edge, right chine, and topmost point on a given forebody cross section. For a given quadrant, the intermediate Φ_p's (1 and 2, 4 and 5, 7 and 8, or 10 and 11) corresponded to 1/3 and 2/3 of the distance around the surface of the forebody between the endpoints of the quadrant.

To better understand the changes in the flowfield produced by the strakes and porous forebody, the porous nose piece contained two sets of static pressure ports on the upper surface that were referred to as the fore and middle rings (fig. 11). The model contained a third set, called the aft ring, that was located behind the porosity region, the inlet, and the aftmost strake position (VG3). The aft ring of ports completely encircled the fuselage. Figure 11 contains the coordinates of the pressure port locations. When portions of the porous forebody were sealed with tape, any pressure ports located within this area were opened using a straight pin. The model also had a flow-through inlet within which a ring of total pressure ports was located, but these ports were not used during the subject study.

Test Techniques and Conditions

The aerodynamic testing was performed in the Langley 12-Foot Low-Speed Tunnel. This tunnel is a continuous-flow facility with a nominal 12-ft-diameter octagonal test section contained within a sphere; the walls of the sphere make up the outer bound of the return passage. The model and balance were mounted onto a sting that passed through the nozzle opening at the rear of the model (fig. 12). The sting was attached to a C-strut arrangement that was used to set the desired sideslip and angle of attack. A six-component internally mounted strain-gauge balance (Langley FF11A) was used to measure the aerodynamic loads. The tests were conducted at a freestream dynamic pressure of 4 lb/ft^2, which corresponded to a test Reynolds number of 0.80×10^6 based on the mean aerodynamic chord of the wing. The static force and moment data were measured over an angle-of-attack range of -4° to 72° and over a sideslip range of -10° to 10°. The data at sideslip angles of -5° and 5° were used to calculate the lateral-directional stability derivatives (C_{l_β}, C_{n_β}, and C_{Y_β}) using a linear calculation between these two angles. Flow upwash corrections were included during the angle-of-attack calibration, but no corrections were made for flow sidewash, wall effects, or test section blockage.

The model surface pressure data was taken using an electronically sensed pressure (ESP) system that was

referenced to the freestream static pressure. Flexible plastic tubing was used to connect the individual ports to transducers that were contained within the model. The ESP's used for these tests had a range of ±1.5 psi.

Flow-visualization tests using smoke were also conducted in the 12-Foot Tunnel. The smoke was generated by heating a light mineral oil and mixing it with pressurized air to force it to enter the tunnel flow. The smoke emanated from a wand that was positioned upstream such that the smoke initially encountered the model at the tip of the nose. The flow-visualization runs were conducted at a lower dynamic pressure ($\bar{q}\approx0.5$) than the force and pressure tests so that the resulting smoke flows would be thicker and easier to see. As a result, the Reynolds number of the flow-visualization tests (0.28×10^6) was reduced from the value for the force tests (0.80×10^6). Despite this lower Reynolds number, the qualitative results from the flow-visualization tests were considered to be applicable when interpreting the quantitative force and pressure data because the separation point of the forebody flow was essentially fixed at the sharp chine. The smoke was illuminated by a translatable laser light sheet that was aligned parallel to the Y-Z plane of the model. This orientation enabled the laser to reveal cross sections of the forebody vortex flow. During a typical test, the laser light sheet was slowly translated aft from the tip of the nose until it was located behind the aft pressure ring. Videotapes of the flow-visualization were recorded from a camera located above the tunnel that looked through the Plexiglas roof of the test section. When the model was at the higher angles of attack, the camera viewed the model from approximately a head-on aspect.

Results and Discussion

Basic Aerodynamic Characteristics of BMRF Configuration

The initial tests performed during this study documented the baseline aerodynamics of the BMRF configuration without any forebody yaw controls added. Figure 13(a) shows the effects of leading-edge flap deflections on the longitudinal characteristics. The data exhibit maximum lift coefficients of 1.33 for $\delta_L=0°$ and 1.38 for $\delta_L=30°$ that both occurred at an angle of attack of 40°. The effects of increased maximum lift and reduced lift at the lower angles of attack are typical of leading-edge flap deflections (ref. 6). The low-angle-of-attack lift losses would be minimized on an actual aircraft by appropriately scheduling the leading-edge flaps with angle of attack. The pitching-moment data show the relaxed static stability (RSS) design approach that was adopted to minimize trim drag at supersonic speeds. The resulting low-angle-of-attack static margin was approximately -0.053 $\bar{c}$ (unstable) when the leading-edge flaps were undeflected. Because they increased lift at the higher angles of attack where the forebody yaw controls were conjectured to be used, the leading-edge flaps were deflected at 30° for all the forebody yaw control testing.

The effects of leading-edge flap deflections on the lateral-directional stability of the BMRF are shown in figure 13(b). The BMRF possessed relatively small (≈0.001) stable values of directional stability (positive C_{n_β}) for angles of attack below 12°. As angle of attack was increased above 12°, the directional stability was reduced, and very large unstable values (-0.003 to -0.004) existed for angles of attack between 36° and 56°. This reduction in directional stability occurred when the vertical tails became ineffective because they were immersed in the low-energy air of the wing and fuselage wakes. In addition, the large magnitude of the directional instability was possibly due in part to the forward placement of the inlet that resulted in increased projected side area in front of the moment reference center. The BMRF was laterally stable (negative C_{l_β}) for all the positive angles of attack tested. Deflection of the leading-edge flaps caused small increases in both lateral and directional stability for most of the angles of attack below 28°.

To provide a comparison to the forebody yaw controls, the rudders were tested at a nominal maximum deflection of -30° (fig. 14). This deflection produced a moderate level of yaw control (≈0.03) that was essentially constant for angles of attack up to 24°. Similar to the decay in directional stability, the rudder effectiveness decayed at angles of attack above 24° as the vertical tails became shielded by the wings and fuselage.

As stated in the introduction, this lack of rudder-produced yaw control at the higher angles of attack is one of the primary reasons for the interest in the development of forebody-mounted yaw controls. In addition to the yawing moments, small adverse rolling moments were produced by rudder deflection for most of the angles of attack tested.

Because yaw-control devices often produce an accompanying rolling moment when they are deployed, the ailerons were tested at nominal intermediate (δa_{left}=15° and δa_{right}=-15°) and maximum deflections (δa_{left}=30° and δa_{right}=-45°) to provide a comparison to the rolling moments produced by the forebody yaw controls and to determine the ability of the ailerons to counteract any adverse rolling moments produced by yaw control deployment (fig. 15). Both deflections produced good levels of low-angle-of-attack roll control effectiveness that decayed somewhat as angle of attack was increased. For angles of attack above 24°, the roll-control effectiveness was roughly 50 percent of the low-angle-of-attack value. Aileron deflections also produced small proverse yawing moments.

Forebody Strakes

The initial forebody-mounted yaw controls that were tested on the BMRF consisted of strakes that, depending on the direction of the desired control, were intended to be deployed on only one side of the aircraft at a time (fig. 7). By articulating in this way, the strakes would create an asymmetric forebody geometry. The goal of this altered forebody shape was to create an asymmetric flowfield that would result in side forces on the forebody along with accompanying yawing moments. So that they would not detrimentally affect the cruise performance or radar signature of the aircraft, the strakes were intended to lie flush within the existing contours of the fuselage when they were not in use.

An extensive investigation of forebody strakes on the BMRF configuration was performed during a different study. For this reason, an abbreviated examination of only two strakes was performed during these tests to provide a comparison to the effectiveness of the porous forebody, and no attempts were made to optimize a given strake design.

Aft-mounted strake (VG3). As stated previously in the model description section of this report, the VG3 strake planform, location, and deflection scheme were formulated by Boeing during the original design of the BMRF. To minimize interference with the fighter's radar scan pattern, the VG3 was located aft of the nose cone on the side of the fuselage underneath the canopy (fig. 7(a)). The VG3 was designed to deflect downwards about its bottom edge.

The aerodynamic effectiveness of the VG3 at maximum deflection (45°) on the left side of the fuselage is shown in figure 16. The VG3 produced yawing moments in two distinct ranges of angle of attack. A region of yaw control with a relatively small peak magnitude of 0.01 was produced at the lower angles of attack between 8° and 32°. These positive yawing moments were not accompanied by significant positive side forces. This result indicated that these yawing moments may have been caused by the effects of the flow downstream of the strakes on the wings or tails, rather than by forces acting on the forebody. A second region of yaw control was produced at the higher angles of attack between 40° and 68°. A peak magnitude of 0.03 was produced within this region that was comparable to the maximum yaw control generated by the rudders (fig. 14), but these values occurred for only a small range of angles of attack near 60°. For this reason, the angle-of-attack range over which this strake could be used effectively will most likely be limited. Small adverse rolling moments were generated by the VG3 at angles of attack below 24°, and slightly larger proverse rolling moments were produced for angles of attack between 24° and 56°. Figure 16(b) shows that deployment of the VG3 resulted in minimal longitudinal effects.

The VG3 was tested with the vertical tails off to investigate the effects of this part of the downstream configuration on the VG3's effectiveness (fig. 17). The primary effects of removing the verticals were an increase in yawing moment at the intermediate angles of

attack between the two yaw-control peaks and a reduction in the proverse rolling moments that occurred at these same angles of attack. These results indicate that the reduced yaw-control effectiveness of the VG3 that occurred at the intermediate angles of attack was due in part to an adverse effect of the flow over the verticals with the VG3 deployed. Removing the verticals also reduced the magnitude of the smaller yaw control peak that occurred at angles of attack near 20°. The combination of these changes made the variation of yawing moment with angle of attack much more linear for angles of attack below 52°. Figure 17(b) shows that removing the verticals caused significant increases in maximum lift, which provided further evidence that the verticals were affecting the upstream flow. The reduction in lift caused by the vertical tails was most likely the result of a fence effect in which the verticals interfered with vortex flow that the wings were experiencing. These results illustrate the importance of considering the downstream effects when evaluating a potential forebody-mounted yaw-control concept.

The effects of sideslip on the yaw control produced by the VG3 at some representative angles of attack is shown in figure 18. Because the VG3 generated positive yawing moments when deployed on the left side of the forebody, this control setting would most likely be used when the aircraft is at a positive sideslip angle to bring the nose back to zero sideslip. For this reason, the $+\beta$ and $+\Delta C_n$ quadrant warrants the most consideration for this control setting. The data for this quadrant show a favorable result; the yawing moments were generally increased when at sideslip. Within the other quadrant, the data show that, except for the α=20° case, the yaw control was also increased at negative sideslip angles.

A comparison of the pressure data at some representative angles of attack for the VG3-off and VG3-on configurations is shown in figure 19, and photographs of the laser-illuminated smoke flow are shown in figure 20. Because the solid nose did not have the fore and middle rings of pressure ports, both the pressure data and flow-visualization pictures were taken using the porous forebody sealed with tape instead of the original solid nose. Both the quantitative pressure data and qualitative flow visualization pictures indicate that the VG3 did not significantly alter the forebody flowfield. The pressure data was essentially identical for the VG3-on and VG3-off cases, and this data was symmetric between the left and right sides of the model. The flow-visualization photographs show a symmetric flowfield for each case that consisted of vortices located just above each chine that were positioned close to the upper surface of the forebody. The pressure data shows the aerodynamic effects of these vortices; large suction peaks occurred at the two farthest outboard ports on the fore and middle rings. In summary, these data illustrate that the yaw-control effectiveness of the VG3 was marginal because it did not result in significant changes in the vortex flowfield generated by the forebody.

Fore-mounted strake (VG6). In general, the effectiveness of a forebody-mounted control may be increased by locating it farther forward (ref. 7). Moving the control forward enables the device to influence the flow earlier in its development, which may be more effective than attempting to alter a better established flowfield. Also, a farther forward control has a longer moment arm about both the yaw and pitch axes. For these reasons, the VG6 was located at the tip of the nose to investigate whether a farther forward strake would be more effective on the BMRF configuration. The curved planform of the VG6 was intended to model a strake that would pivot outwards about a hinge point at the strake's front tip (fig. 7(b)). The VG6 was mounted on either the left or right chine such that it extended straight out with no upward or downward deflection. The VG6 was tested primarily for research purposes, and no plans existed at the time of these tests for incorporating the VG6 into the BMRF design.

The aerodynamic effectiveness of the VG6 when mounted on either the left or right side of the fuselage is shown in figure 21. As expected because of its farther forward location, the VG6 produced larger yawing moments than the VG3 (fig. 16) for an extensive angle-of-attack range between 20° and 68°. Proverse rolling moments were also produced at these angles of attack. The peak yawing moments generated by the VG6 at the higher angles of attack between 52° and 62° were greater than the maximum value (0.03) generated by the rudders (fig. 14). The side forces produced by the VG6 were also much larger than those generated by the VG3, and they were in the appropriate direction to indicate that they

were acting on the forebody to yield the observed yawing moments. These results provided evidence that the VG6 had a more pronounced effect on the forebody flowfield than the VG3. Further evidence that the VG6 was affecting the forebody flowfield was seen in the longitudinal results (fig. 21(b)); addition of the VG6 resulted in a small maximum lift increase and a corresponding nose-up pitching-moment increment. These effects were caused primarily by an increase in the forebody planform area that resulted from addition of the VG6 (fig. 7(b)).

The VG6 was also tested with the vertical tails off (fig. 22). Removing the vertical tails on the VG6 configuration had similar effects to those seen for the VG3 (fig. 17): yawing moment was decreased at the lower angles of attack, yawing moment was increased at the intermediate and high angles of attack, the variation of yawing moment with angle of attack was more linear, the proverse rolling moments were reduced, and maximum lift was increased. These results indicate that, similar to the VG3, the VG6 also had reduced yaw-control effectiveness for a fairly large angle-of-attack range as the result of an adverse effect of the flow over the verticals with the VG6 deployed.

The effects of sideslip on the yaw control produced by the VG6 at some representative angles of attack is shown in figure 23. The data shown is for the VG6 on the left side of the model, which produced positive yawing moments. As discussed previously, the $+\beta$ and $+\Delta C_n$ quadrant warrants the most consideration for this control setting. The data for this quadrant show a similar favorable result to that for the VG3; the yawing moments were significantly increased when at these sideslip angles. In contrast to the VG3, the data within the other quadrant show that the yaw control was generally decreased at negative sideslip angles.

Porous Forebody

Upon completion of the strakes testing, the original solid nose of the BMRF model was replaced with a similarly shaped piece that had a porous outer skin and an inner solid section (fig. 8). This new nose was used to test the yaw-control effectiveness of various patterns of forebody porosity (fig. 10). These patterns were obtained by taping over the areas that were not desired to be porous. At the time of these tests, a method for mechanizing the opening and closing of the porous areas on either the model or full-scale aircraft had not been developed. The rationale behind the porosity was to allow air to flow from the bottom surface through the nose to the upper surface when the model was at an angle of attack. This air flow was intended to reduce the pressure differential that occurs across the sharp chine, thereby affecting the vortex formation and separation patterns of the forebody flowfield. Similar to the strakes, porosity would be applied primarily to one side of the aircraft at a time, depending on the direction of the desired control, to create an asymmetric flowfield.

Symmetric porosity configurations. Before asymmetric regions of porosity were investigated, the porous forebody was tested fully open and fully sealed to compare the aerodynamic characteristics of these symmetric configurations with those for the original solid nose (fig. 24). With the exception of yawing moment, the data show minimal differences between the original solid nose and either of the porous forebody configurations. On the sealed porous forebody, moderate yawing moments were produced at angles of attack between 52° and 64°. This aerodynamic asymmetry was attributed to the sensitivity of yawing moment to small imperfections near the tip of the nose in the tape that was used to seal the porous forebody. Repeat runs were made in which the model was re-taped each time. Despite care being taken to insure that the tape was smooth and as uniform as possible between the right and left sides, the magnitude of this asymmetry varied within the different runs between zero and the values shown in figure 24.

A comparison of the pressure data at some representative angles of attack for the open and sealed porous forebody configurations is shown in figure 25, and photographs of the corresponding laser-illuminated smoke flow are shown in figure 26. As seen previously (VG3-off photos in figure 20), the flow-visualization photos for the sealed nose show a symmetric flowfield that consisted of a vortex located immediately above each chine. The corresponding pressure data shows that suction peaks occurred at the two farthest outboard ports on the fore and middle rings as a result of these vortices.

When the porous forebody was fully open, the pressure data was significantly different. The pressure distribution on the upper surface of the forebody was essentially uniform with no large-magnitude suction peaks. This result indicated that the porosity was successful in reducing the pressure differential across the sharp chine and in decreasing the likelihood that vortices would form on the upper surfaces of the forebody. The flow-visualization photos for the open porous forebody show that this flowfield was also symmetric but different from that for the sealed forebody. This flowfield contained vortices that appeared to form aft of the porous region, and they were positioned much higher on the model near the canopy.

Required radial porosity coverage. The initial tests of asymmetric porosity consisted of varying the radial pattern of the porous region while holding the chordwise coverage constant at the maximum value. The objective of this set of tests was a gross determination of the radial pattern that would generate the largest yawing moments. Figure 27 shows the aerodynamic effects of increasing the radial porosity coverage by quadrant when starting from the top centerline (Φ_p = 9-12, 6-12, and 3-12), and figure 28 shows the results that occurred when starting from the bottom centerline (Φ_p = 6-9, 6-12, and 6-3). When considered together, these data suggest two primary conclusions. The configurations with asymmetric porosity on the upper surfaces (Φ_p = 9-12, 6-12, and 3-12) generated yawing moments, but the configurations that were symmetric on the top, whether sealed (Φ_p = 6-9) or porous (Φ_p = 6-3), did not. Secondly, the yawing moments were made larger by increasing the radial porosity coverage on the bottom surfaces. On each of the effective configurations, yawing moments were produced for angles of attack above 16°, but the largest values occurred for angles of attack between 44° and 64°. The peak magnitudes of these yawing moments were equal to or greater than those produced by the VG6 strake. Small proverse rolling moments were also generated on the effective configurations, and small nose-up pitching-moment increments occurred for angles of attack above maximum lift. Based on these results, the Φ_p=6-12 configuration was chosen for further study because it generated relatively high yawing moments and required significantly less area of the forebody to be porous than the slightly more effective Φ_p=3-12 configuration.

A comparison of the pressure data at some representative angles of attack for the sealed forebody and the porous configuration with Φ_p=6-12 is shown in figure 29, and photographs of the corresponding laser-illuminated smoke flow are shown in figure 30. As discussed previously, the pressure data and flow-visualization photos for the sealed forebody indicate a symmetric flowfield that consisted of a vortex located immediately above each chine. On the Φ_p=6-12 configuration, both the pressure data and flow-visualization photos show that this porosity pattern was highly successful at creating an asymmetric flowfield. For angles of attack below 40°, the effects of porosity were primarily seen in the pressure data for the fore and middle rings. On the sealed side (right side on figures), the pressure distribution was essentially unchanged from the values for the fully sealed configuration. On the porous side (left side on figures), the pressure data did not contain a suction peak, and the pressure distribution was uniform at a relatively small value. Consequently, the suction peak remaining on the non-porous side caused a resultant side force and a corresponding yawing moment away from the porous side. At the higher angles of attack between 40° and 60°, the pressure data contained several characteristics that explained the increased yaw-control effectiveness that occurred at these angles of attack. On the sealed side, the suction peaks were increased from the values that occurred on the fully sealed configuration. Also, the aft ring showed asymmetries in the pressure data, which indicated that the porosity was influencing the pressure distribution on a larger chordwise section of the forebody. The flow-visualization photos show that the flow on the non-porous side contained a similar vortex to the case when the forebody was fully sealed. On the porous side, the flow near the chine contained a poorly defined vortex that appeared to form aft of the porous region. The flow on the porous side also contained a detached second vortex that was located higher up on the forebody. This vortex appeared to be fed by flow from the non-porous side which crossed over the top of the forebody and entered this vortex from above.

When incorporating porosity into an actual aircraft, it will probably be desirable to minimize the total porous area to reduce the complexity and cost of the required mechanization or to limit any adverse effects of porosity on the radar performance or aircraft radar cross section. As a result of this concern, the next objective of these tests was a more detailed investigation into whether the radial porosity coverage of the Φ_p=6-12 configuration could be reduced while maintaining a similar level of yaw control. Because porosity was intended to reduce the pressure differential that occurs across the sharp chines, tests were made using the Φ_p=7-10 configuration to determine if confining the porosity to an area near the chine would maintain the majority of the effectiveness of the Φ_p=6-12 configuration. Figure 31 compares the aerodynamic effectiveness of the Φ_p=7-10 and Φ_p=6-12 configurations. The data show that this change in the radial porosity coverage significantly reduced the generated yawing moments. The Φ_p=7-10 pattern was effective over a smaller angle-of-attack range than the Φ_p=6-12 pattern, and the peak magnitude that it generated was roughly half of the Φ_p=6-12 configuration value. These reductions in yaw-control effectiveness were judged to be too large for the Φ_p=7-10 configuration to be a viable porosity pattern for the BMRF, and consequently the Φ_p=6-12 pattern was used in most of the subsequent studies.

Required chordwise porosity coverage. In keeping with the objective to minimize the total porosity area, the next set of tests investigated reductions in the chordwise porosity coverage. The previously developed radial pattern of Φ_p=6-12 was used for all of these tests. Because locating a forebody control farther forward generally makes if more effective (ref. 7), configurations were tested in which the chordwise porosity coverage was reduced from the rear to 1/2 {X_p=(0-50)%l_{pf}} and 1/4 {X_p=(0-25)%l_{pf}} of its maximum value. A configuration was also tested in which the porosity was confined to only the aft half of the porous piece {X_p=(50-100)%l_{pf}}. The purpose of this pattern was to investigate the effectiveness of a configuration on which a small radar could be mounted in the nose ahead of the porous region.

Figure 32 compares the aerodynamic effectiveness of the configurations on which the chordwise porosity coverage was varied. Reducing the chordwise coverage by half {X_p=(0-50)%l_{pf}} reduced the yaw-control effectiveness by approximately 40 percent at the higher angles of attack between 44° and 68°. Reducing the chordwise coverage further to 1/4 of its maximum value {X_p=(0-25)%l_{pf}} caused an additional 10 percent reduction at these same angles of attack, and this configuration therefore had roughly half of the yaw-control effectiveness of the X_p=(0-100)%l_{pf} configuration. The X_p=(50-100)%l_{pf} configuration was very unsuccessful. This pattern generated minimal yawing moments that were roughly equivalent to the asymmetry that occurred on the fully sealed configuration. This result was consistent with the strake data that showed that a forebody control should be located as close to the tip of the nose as possible for maximum effectiveness. Based on these results, it was judged that the chordwise porosity coverage could not be reduced on the BMRF without detrimentally affecting the yaw-control effectiveness, and therefore the maximum chordwise coverage was used during all subsequent testing.

Modulation of yaw control from asymmetric porosity. To effectively use the porous forebody to control an aircraft, a procedure will be required for varying the porosity pattern, and hence modulating the generated yawing moment, between the baseline symmetric configuration (nominally fully sealed) and the asymmetric pattern used for maximum control. Based on the results discussed in the previous section (fig. 32), chordwise variation of the porosity coverage did not appear to be a promising modulation scheme because the variation of yawing moment was not linear with changes in the chordwise length of the porosity region. For this reason, gradual variation of the radial coverage of the porous region was explored as a way to modulate the yaw control produced by the porous forebody.

Figure 33 shows the effects of starting from the top centerline on the Φ_p=6-12 configuration and systematically closing off the radial porosity coverage on

the upper surfaces. Changing the porosity pattern in this way is analogous to a fully deflected rudder being gradually brought back to zero deflection. At angles of attack between 16° and 52°, these variations in the porosity pattern produced corresponding reductions in yawing moment. Although these changes in yawing moment were not entirely linear with reductions in the radial porosity coverage, the incremental nature of the behavior indicated that this method could possibly be used to modulate yaw control at these angles of attack. More detailed analysis involving actuation rates and the complete aircraft dynamics would be required to make this determination. As angle of attack was increased above 52°, the yawing moments produced by the various configurations coalesced, and this scheme would therefore not be effective at these angles of attack. Figure 34 shows the results that occurred when a similar scheme was applied to the Φ_p=9-12 configuration. Considering the overall lower level of yaw-control effectiveness on this configuration, the trends were generally similar to those seen when starting from the Φ_p=6-12 pattern.

Most effective asymmetric porosity configuration. The configuration with Φ_p=6-12 and X_p=(0-100)%l_{pf} generated a good level of yaw control that could be modulated by varying the radial coverage of the porosity on the upper surfaces. If a way of mechanizing the opening and closing of the porous areas can be developed, this porosity pattern may be a viable concept for obtaining high-angle-of-attack yaw control on advanced fighters. For these reasons, this configuration was judged to be the most successful of all the variations tested, and it was therefore selected for more in-depth testing.

The Φ_p=6-12 configuration was tested with the vertical tails off to investigate the effects of this part of the downstream configuration on its effectiveness (fig. 35). Removing the verticals caused a reduction in the yawing moment generated by the porous forebody over a small range of angles of attack between approximately 46° and 56°. This effect was different from that seen for the strake configurations (figs. 17 and 22) on which removing the verticals generally increased the strake-generated yawing moments at these same angles of attack. Therefore unlike the strakes, this porous forebody configuration had slightly improved effectiveness at some angles of attack as the result of a favorable interaction between the verticals and the porous forebody flowfield.

The effects of sideslip on the yaw control produced by the Φ_p=6-12 porosity pattern at some representative angles of attack are shown in figure 36. This configuration produced negative yawing moments, which were opposite in sign to the strake data discussed previously (figs. 18 and 23). Because these yawing moments would most often be needed when the aircraft was at a negative β to bring the nose back to zero sideslip, the $-\beta$ and $-\Delta C_n$ quadrant warrants the most consideration for this configuration. Also, the data for an angle of attack of 52° is the most important of the data shown because the porous forebody was most effective at this angle of attack. At both negative and positive sideslip angles, yawing moment varied nonlinearly between values slightly above and below the zero sideslip level. Despite these variations, this porosity pattern maintained a good level of effectiveness at all the sideslip angles tested.

The porous forebody was tested in conjunction with rudder deflections to determine the total yaw control available on the BMRF throughout the test angle-of-attack range (fig. 37). The data show that the effectiveness generated by the two devices when deployed separately could essentially be added together to obtain the yaw control produced when they were deployed together, which indicated minimal interaction between the two controls. At the lower angles of attack below 24°, the porous forebody was ineffective, and the rudder provided all the yaw control. At angles of attack above 44°, the opposite was true. The rudder was ineffective, and the porous forebody produced all the yaw control. At the intermediate angles of attack between 24° and 44°, neither control was very effective, and a region of significantly reduced yaw control existed. Because maximum lift lies within this angle-of-attack range, this reduced yaw control could seriously limit the maneuvering capability of this configuration. This problem could be addressed by either redesigning the vertical tails and rudders so that they remain effective to

a higher angle of attack or altering the forebody shape or porosity pattern to produce a forebody control that becomes effective at a lower angle of attack.

Summary of Results

Low-speed wind-tunnel tests were conducted in the Langley 12-Foot Low-Speed Tunnel on a model of the Boeing Multirole Fighter (BMRF) aircraft. The ability to maneuver at angles of attack up to and beyond maximum lift was desired for this aircraft so that it would be more effective in the close-in arena of air combat. Because traditional aerodynamic yaw controls, such as rudders, are typically ineffective at these higher angles of attack, this study focused on investigating forebody-mounted controls that produce yawing moments by modifying the strong vortex flowfield being shed from the forebody. Two forebody strakes were tested that varied in planform and chordwise location. Various patterns of porosity in the forebody skin were also tested that differed in their radial coverage and chordwise location. The results of this investigation may be summarized as follows:

1. The aftmost strake (VG3), which was formulated during the original BMRF design process, produced yawing moments at angles of attack near 60° with peak values that were comparable to the maximum effectiveness generated by the rudders at low angles of attack. The usefulness of this control may be limited however by the fairly small angle-of-attack range over which it was effective.

2. A strake mounted farther forward at the tip of the nose (VG6) produced yawing moments over a much larger angle-of-attack range than the VG3, and the maximum yawing moments produced by this control were higher than those generated by either the VG3 or the rudders. Although aerodynamically more successful than the VG3, this strake design may not be usable if the hardware required interferes with the performance of the nose-mounted air-to-air radar.

3. Porosity generated yawing moments at the higher angles of attack when the portion of the porosity pattern on the upper surfaces of the forebody was asymmetric between the left and right sides of the model. These yawing moments were made larger by increasing the radial porosity coverage on the bottom surfaces of the forebody.

4. Similar to the strakes, the effectiveness of porosity was increased by locating it farther forward on the forebody.

5. The porosity pattern in which either the left or right half of the forebody was porous and the other half was sealed generated yawing moments at the higher angles of attack that were comparable to the values produced by the VG6 strake. This yaw control could be modulated by gradually closing off the porosity from the top. If a way of mechanizing the opening and closing of the porous areas can be developed, this porosity pattern may be a viable concept for obtaining high-angle-of-attack yaw control on advanced fighters.

6. Both the pressure data and the flow-visualization studies showed that all the effective yaw-control concepts altered the forebody vortex flowfield such that it was highly asymmetric between the left and right sides of the model. The pressure data showed that these controls typically reduced the suction pressures on the side on which they were deployed, and the suction on the other side was generally maintained or increased slightly. The resultant side force caused a yawing moment away from the side containing the control.

7. An unfavorable interaction of the flowfield produced by the strakes with the downstream vertical tails caused small reductions in the yawing moments produced by the strakes. In contrast, the yawing moments produced by the porous forebody were increased slightly by the presence of the vertical tails.

8. At angles of attack where they produced yaw control, both the strakes and porous forebody remained effective when at sideslip.

9. The combination of rudder deflections at low angles of attack and porosity at high angles of attack gave this configuration good levels of yaw control for a large portion of the test angle-of-attack range. But at the

intermediate angles of attack around maximum lift, neither of these controls was very effective, and a region of diminished yaw control existed that may limit the maneuverability of this design.

References

1. Doane, P. M.; Gay, C. H.; Fligg, J. A.; et al: *Multi-System Integrated Control (MuSIC) Program.* WRDC-TR-90-6001, 1990.

2. Lynch, U. H. P.; Ettinger, R. C.; Palt, J. V.; and Skow, A. M.: *Tactical Evaluation of the Air-To-Air Combat Effectiveness of Supermaneuverability.* WRDC-TR-90-3035, 1990.

3. Hoffler, K. D.; Ogburn, M. E.; Nguyen, L. T.; Brown, P. W.; and Phillips, Lt. Col. M. R.: *Utilization and Benefits of Advanced Aerodynamic and Propulsive Controls: A Simulator Study.* NASA CP-3150 Volume II, October 1990, pp. 87-119.

4. Ogburn, Marilyn E.; Nguyen, Luat T.; Wunschel, Alfred J.; Brown, Philip W.; and Carzoo, Susan W.: *Simulation Study of Flight Dynamics of a Fighter Configuration With Thrust-Vectoring Controls at Low Speeds and High Angles of Attack.* NASA TP 2750, 1988.

5. Chambers, Joseph R. and Grafton, Sue B.: *Aerodynamic Characteristics of Airplanes at High Angles of Attack.* NASA TM 74097, 1977.

6. Talay, Theodore A.: *An Introduction to the Aerodynamics of Flight.* NASA SP-367, 1975.

7. Murri, Daniel G.; Biedron, Robert T.; Erickson, Gary E.; Jordan, Frank L., Jr.; and Hoffler, Keith H.: *Development of Actuated Forebody Strake Controls For the F-18 High Alpha Research Vehicle.* NASA CP-3149 Volume I, October 1990, pp. 335-380.

Table 1. Model Geometric Characteristics

Fuselage:	
Length, in.	76.86
Wings:	
Area, in^2	1046.25
Span, in.	48.00
Mean aerodynamic chord, in.	26.10
Root chord, in.	38.61
Tip chord, in.	3.72
Aspect ratio	2.20
Taper ratio	0.10
Leading-edge sweep, deg	47.15
Trailing-edge sweep, deg	-16.80
Dihedral, deg	-10.00
Incidence, deg	0.00
Leading-edge flap area (per wing), in^2	45.11
Trailing-edge flap area (per wing), in^2	33.20
Aileron area (per wing), in^2	18.46
Leading-edge flap deflection, deg	0 to 45 (L.E.D.)
Trailing-edge flap deflection, deg	-45 (T.E.U.) to 45 (T.E.D.)
Aileron deflection, deg	-45 (T.E.U.) to 45 (T.E.D.)
Horizontal tails:	
Area (each), in^2	75.95
Leading-edge sweep, deg	47.50
Trailing-edge sweep, deg	17.00
Deflection, deg	-30 (T.E.U.) to 30 (T.E.D.)
Vertical tails:	
Area (each), in^2	92.15
Leading-edge sweep, deg	42.78
Trailing-edge sweep, deg	27.10
Outward cant angle, deg	30.00
Rudder area, in^2	19.22
Rudder deflection, deg	-45 (T.E.R.) to 45 (T.E.L.)

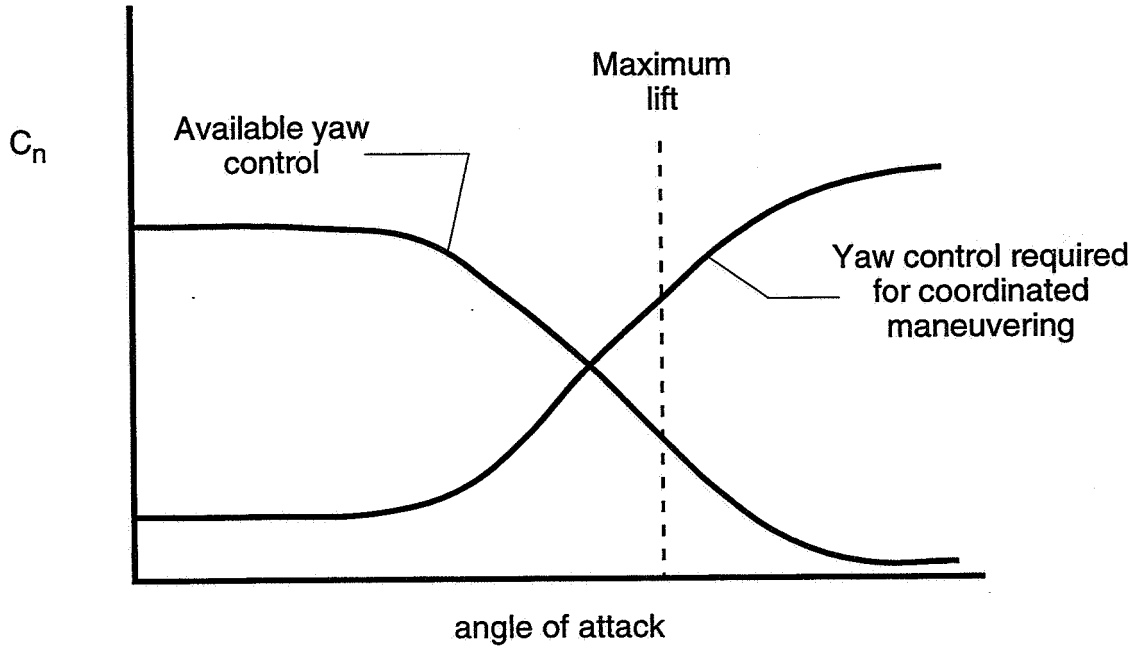

Figure 1. Typical variation of yawing moment with angle of attack for conventional rudders.

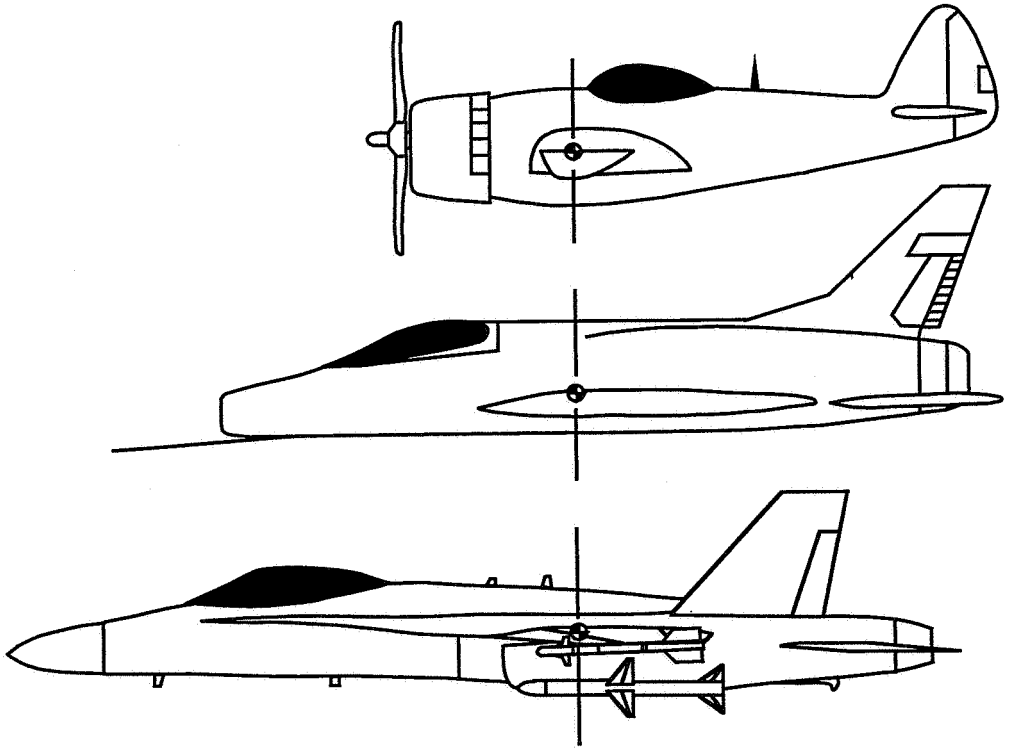

Figure 2. Illustration of fighter design trend towards farther aft center of gravity and longer forebody.

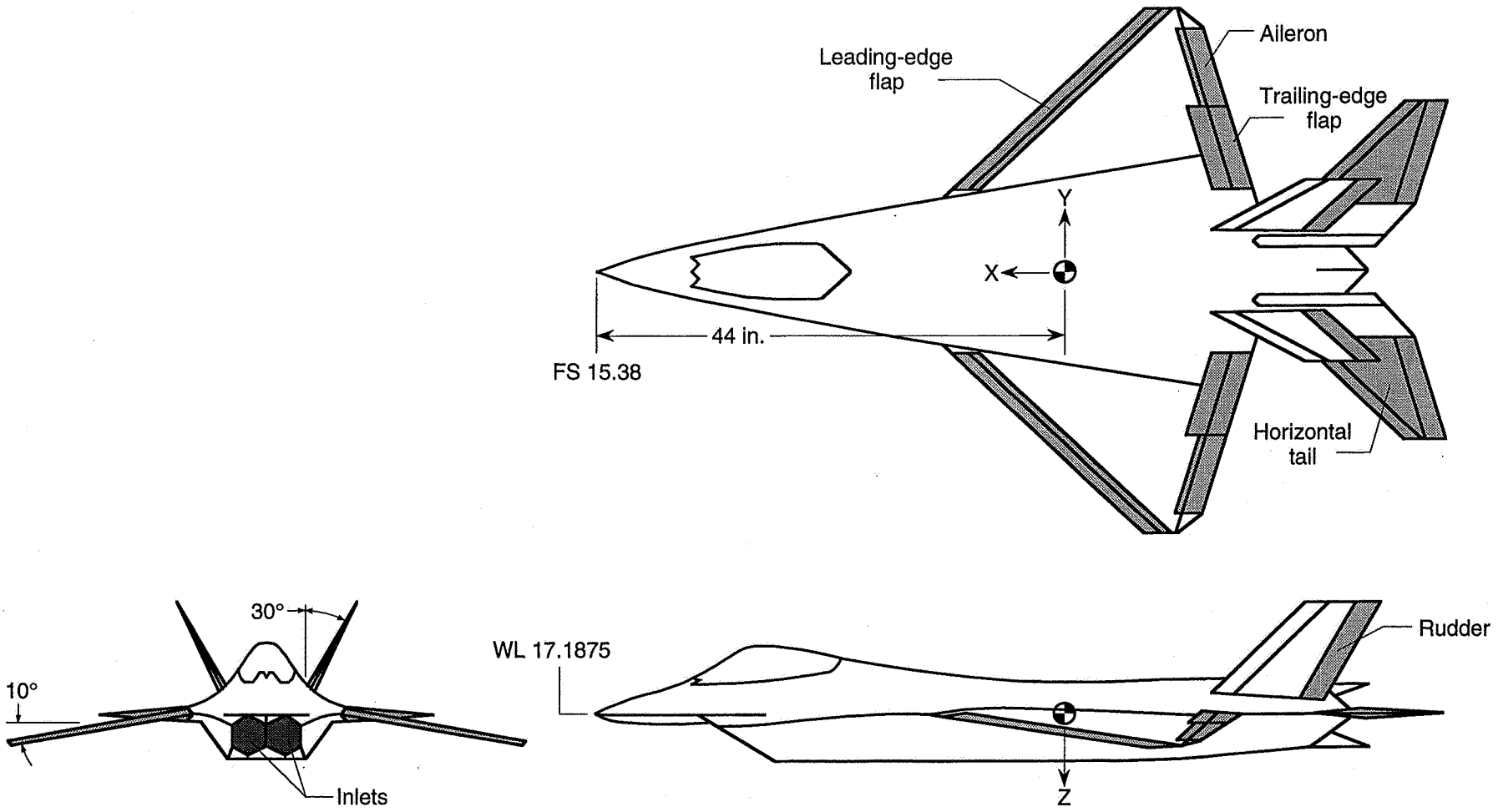

Figure 3. Boeing Multirole Fighter (BMRF) configuration.

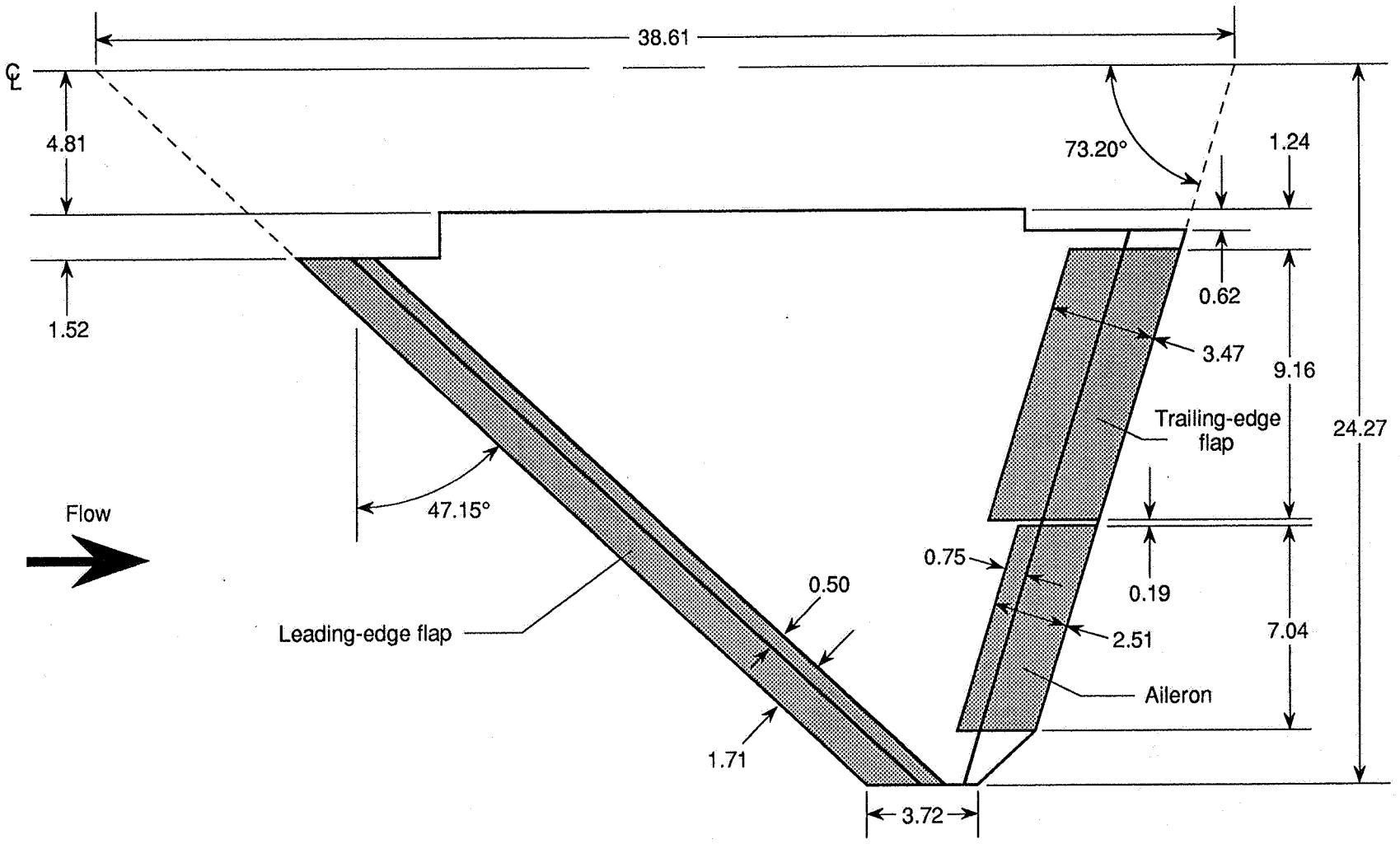

Figure 4. Wing planform. Shaded areas indicate movable surfaces. Linear dimensions are in inches.

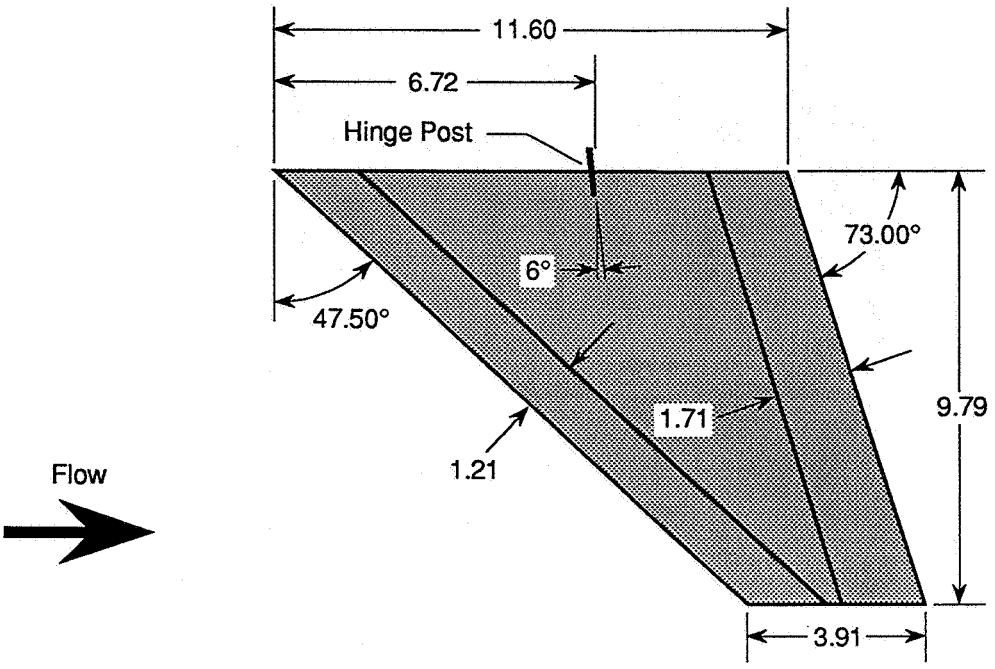

(a) Left horizontal tail.

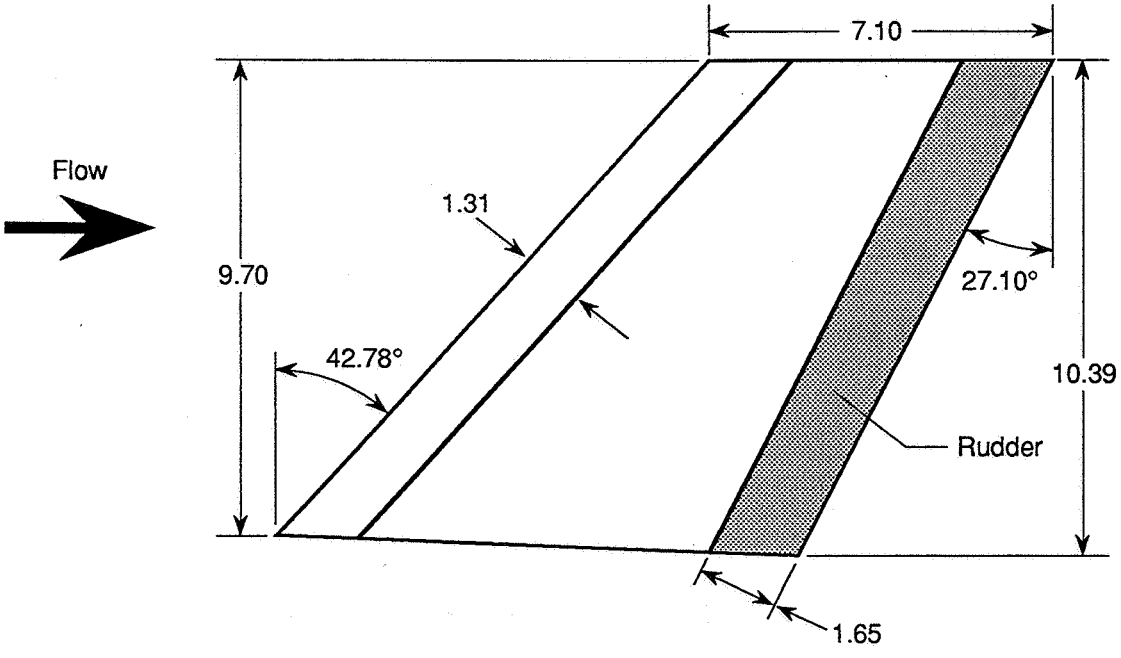

(b) Vertical tail.

Figure 5. Planform views of tails. Shaded areas indicate movable surfaces. Linear dimensions are in inches.

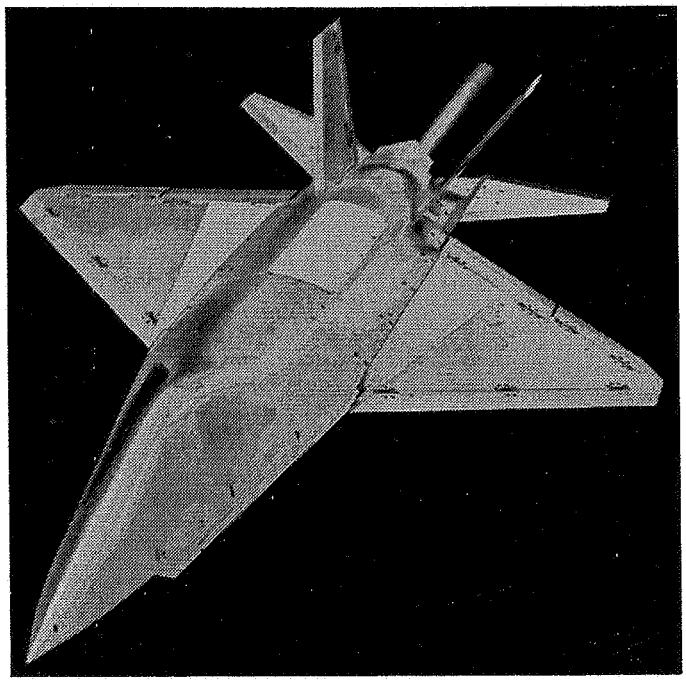

(a) 3/4 front view of model.

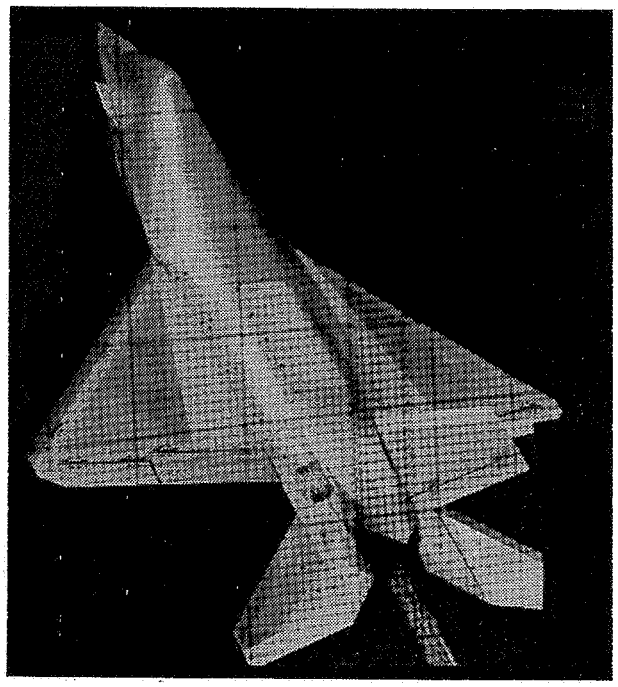

(b) Rear view of model mounted in tunnel with strake deployed.

Figure 6. Photographs of model.

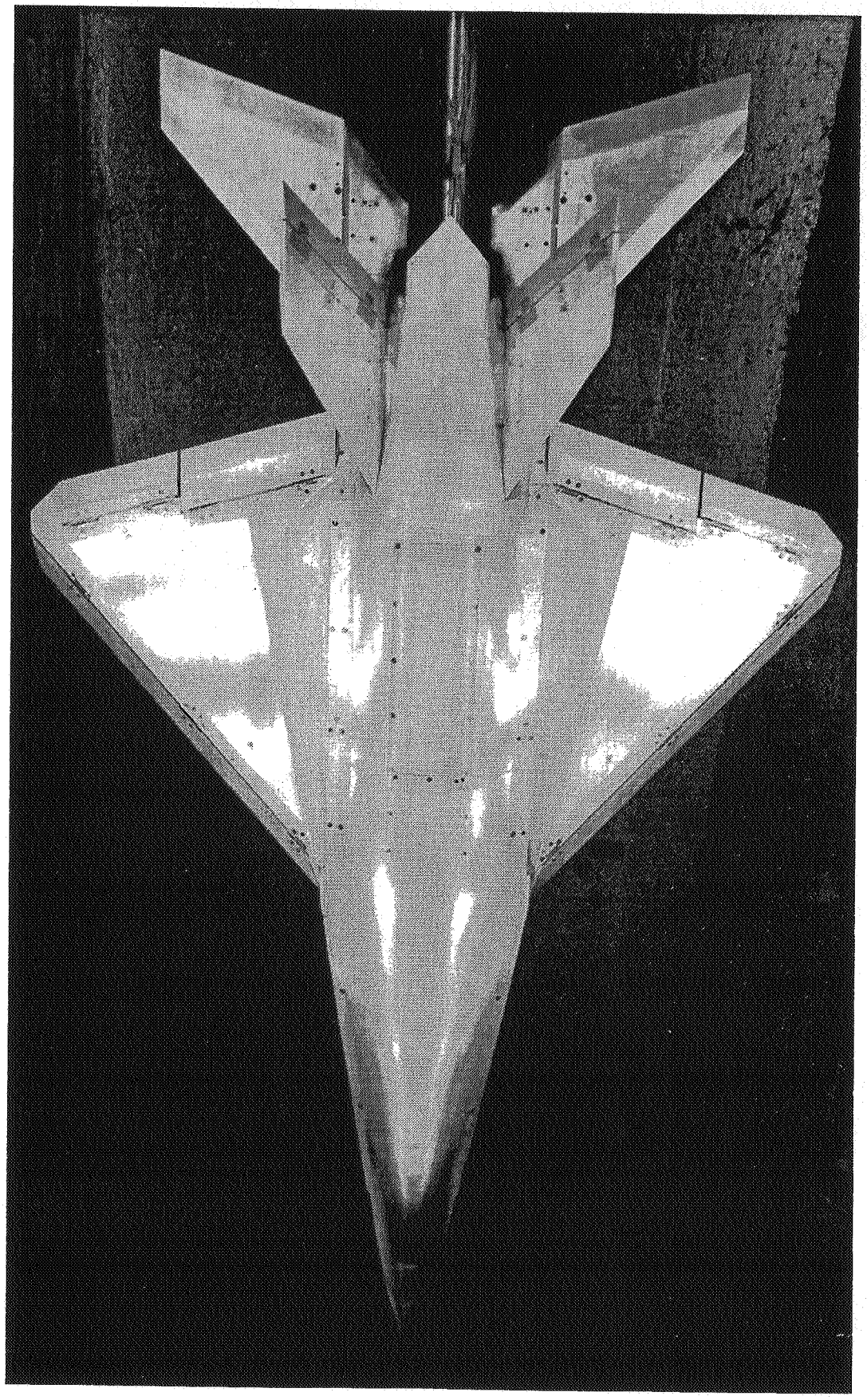

(c) Top view of model mounted in tunnel.

Figure 6. Continued.

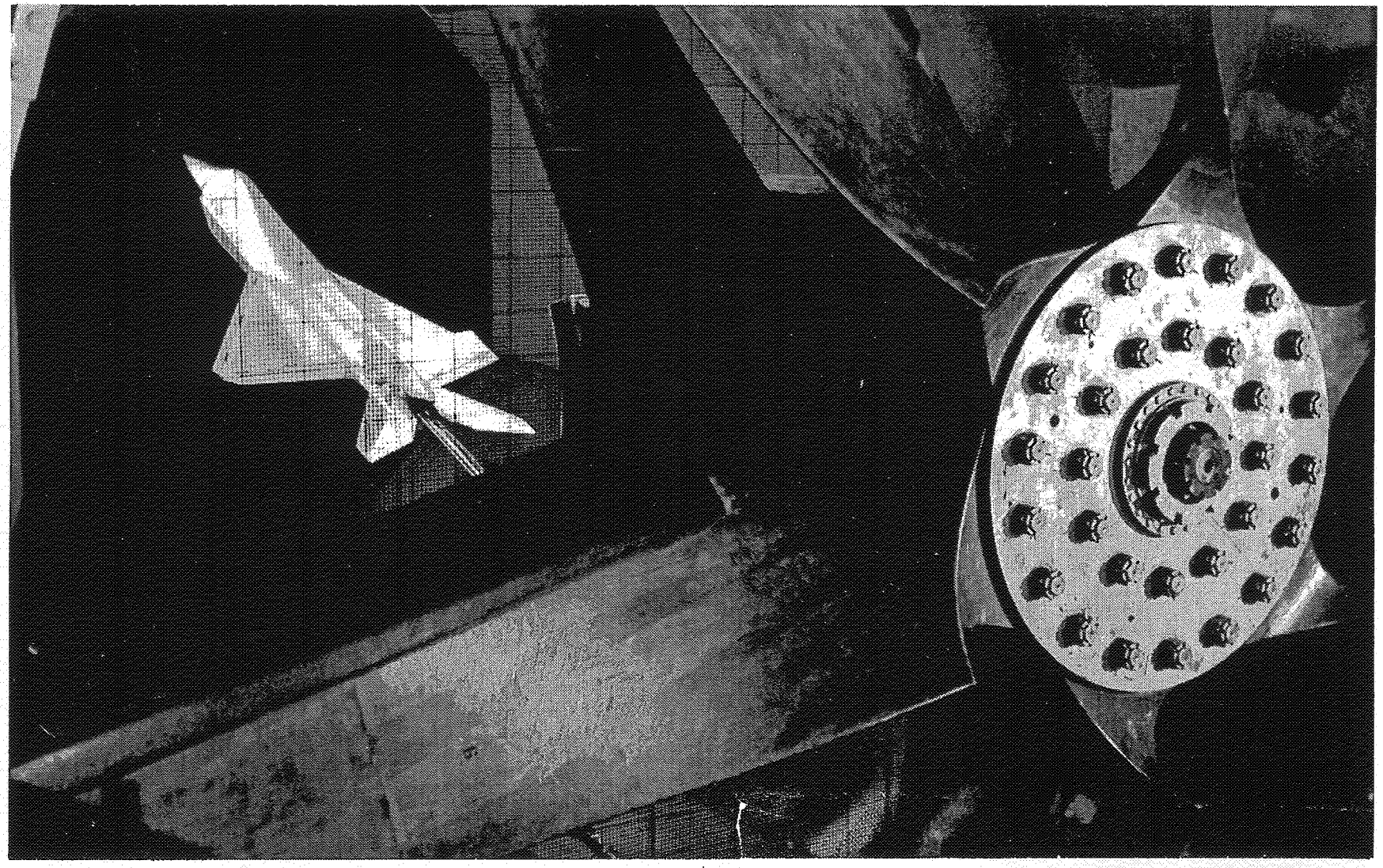

(d) View through fan blades of model mounted in tunnel.

Figure 6. Continued.

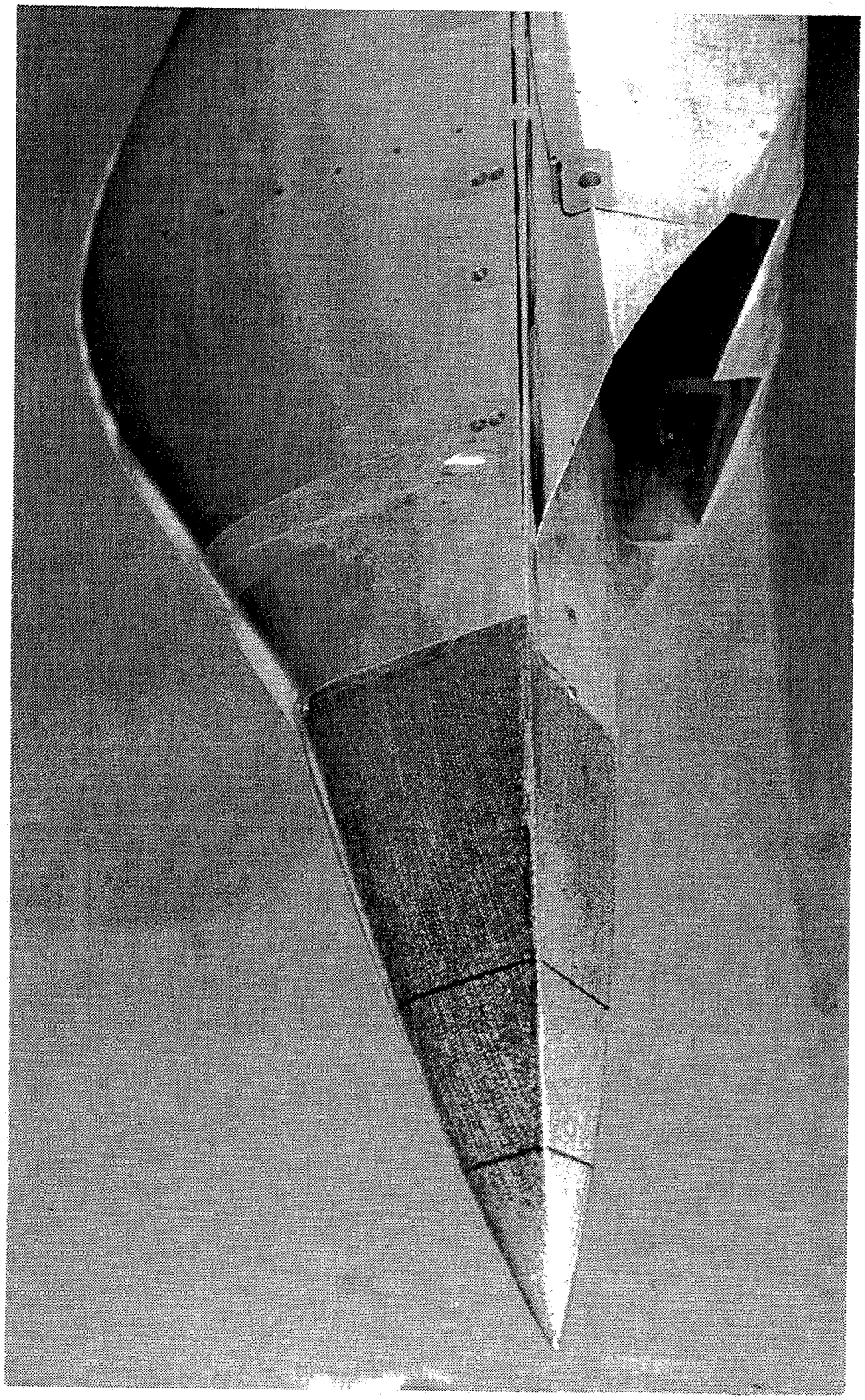

(e) Side view of porous forebody.

Figure 6. Concluded.

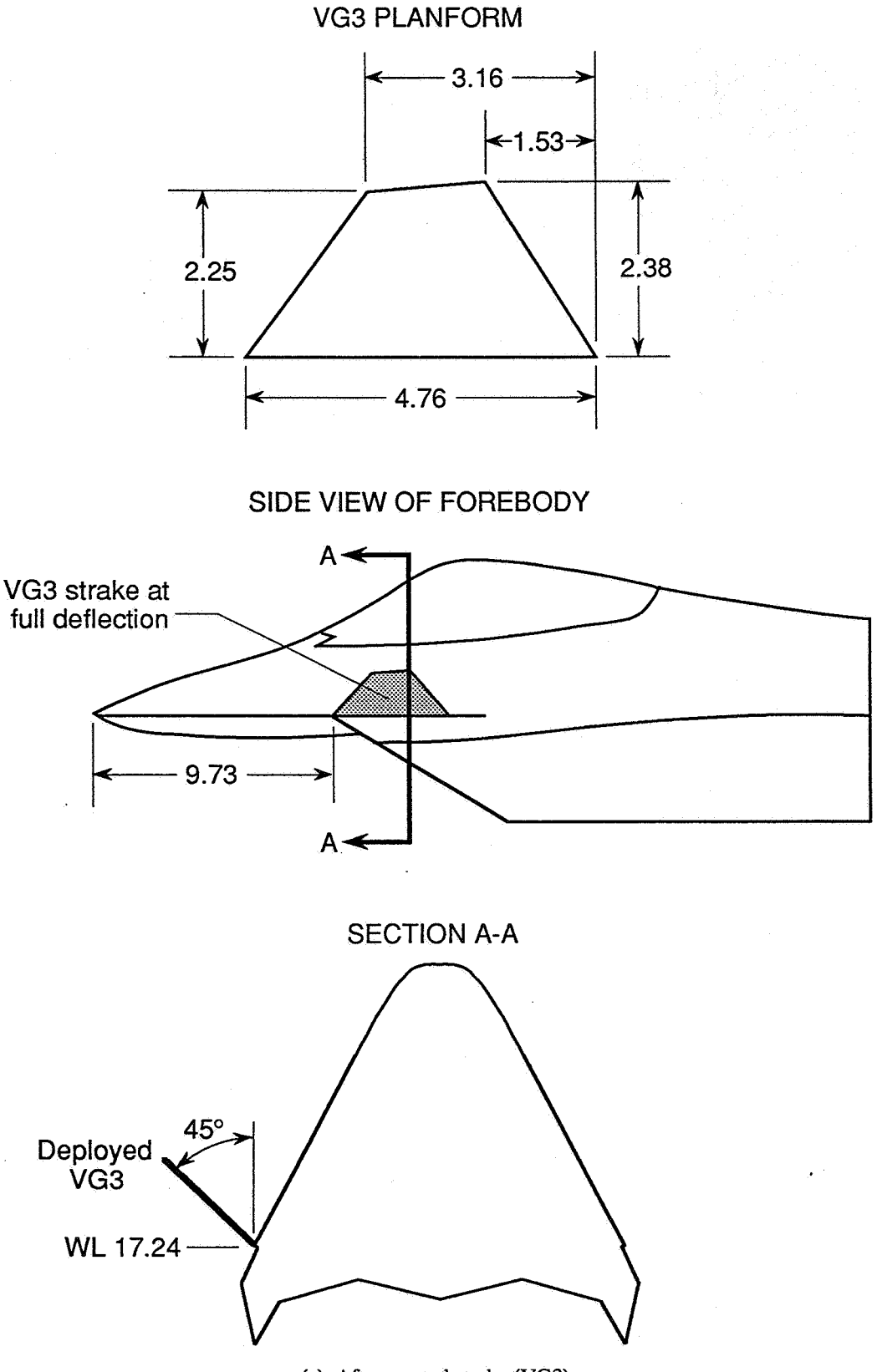

(a) Aft-mounted strake (VG3).

Figure 7. Forebody strakes. Linear dimensions are in inches.

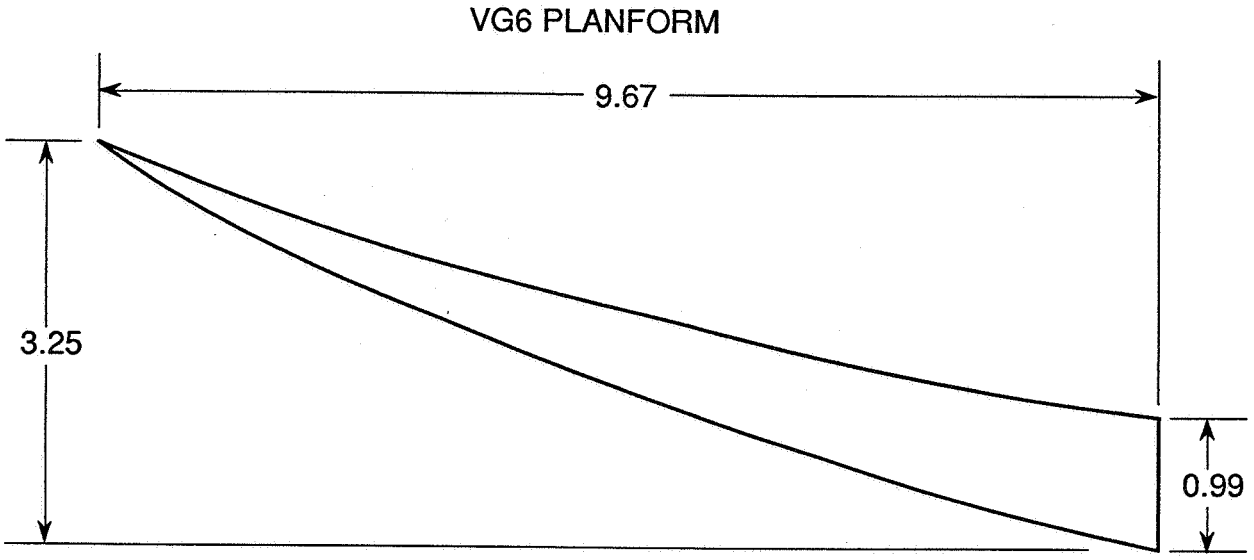

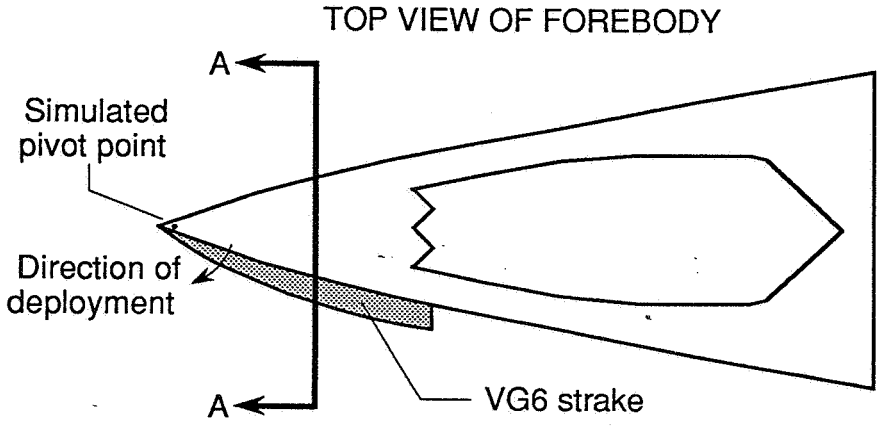

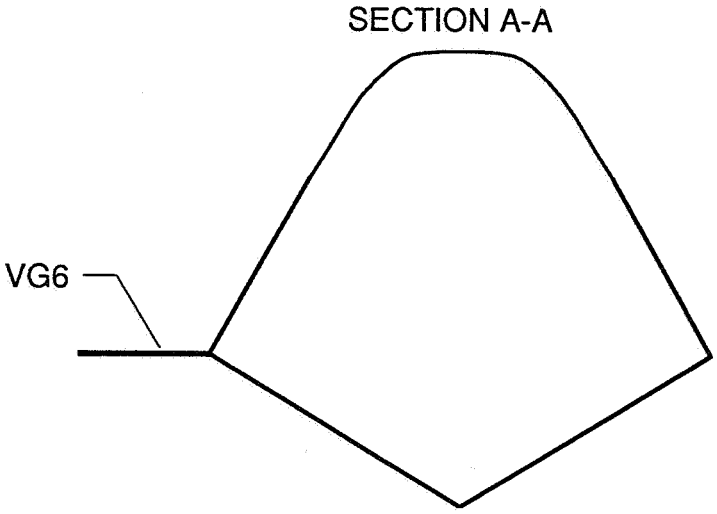

(b) Fore-mounted strake (VG6).

Figure 7. Concluded.

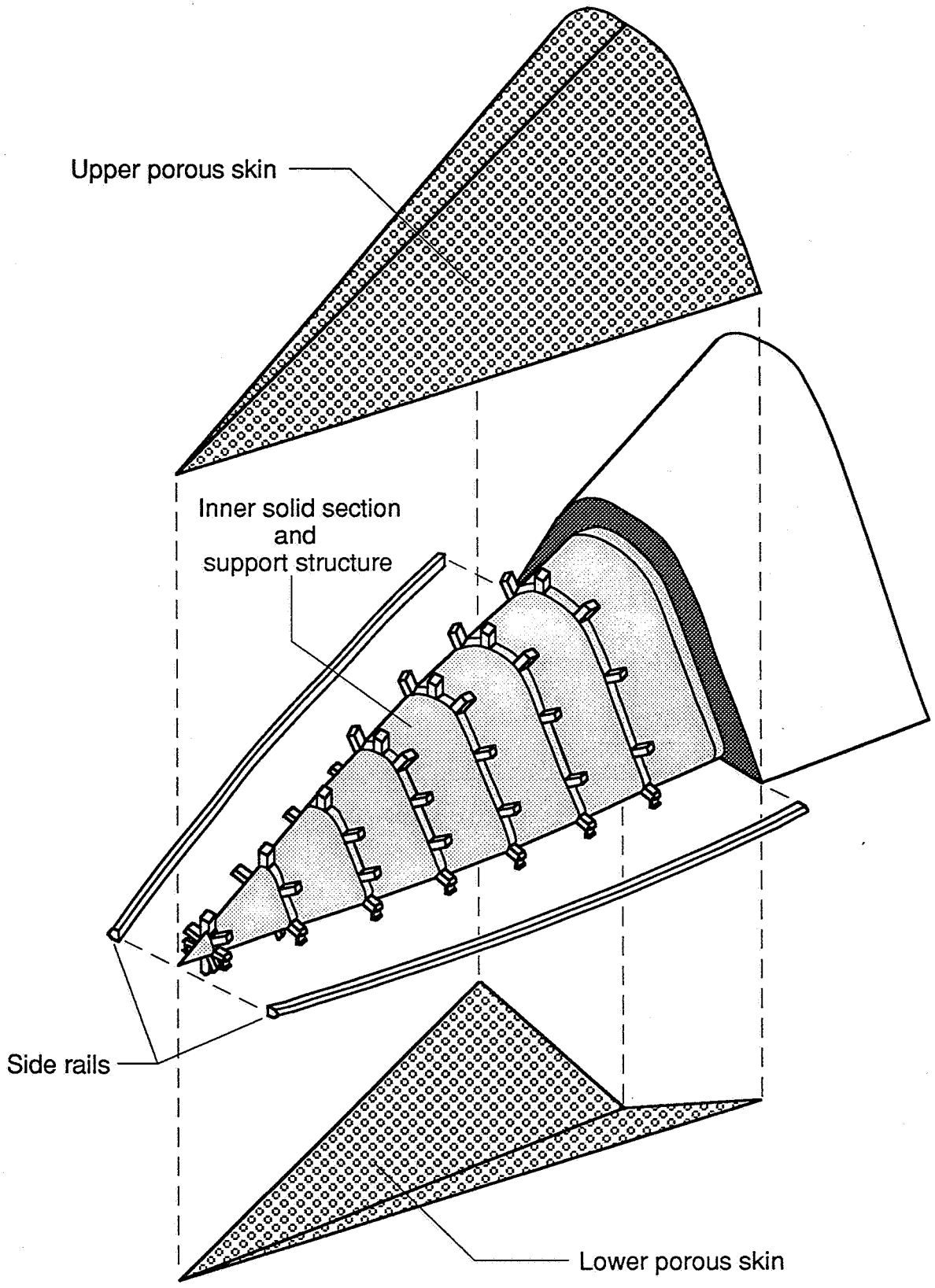

Figure 8. Exploded view of porous nose piece.

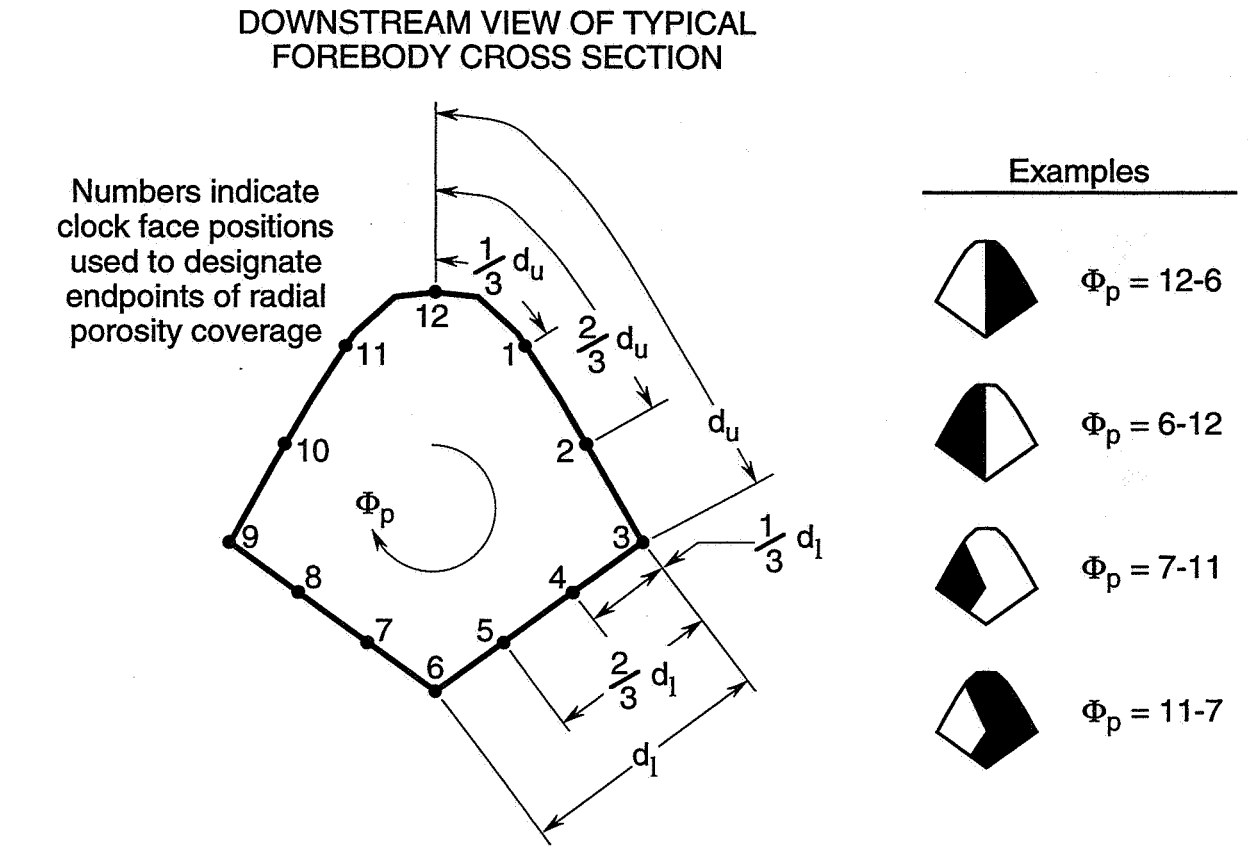

(a) Φ_p , variable used to designate radial porosity coverage.

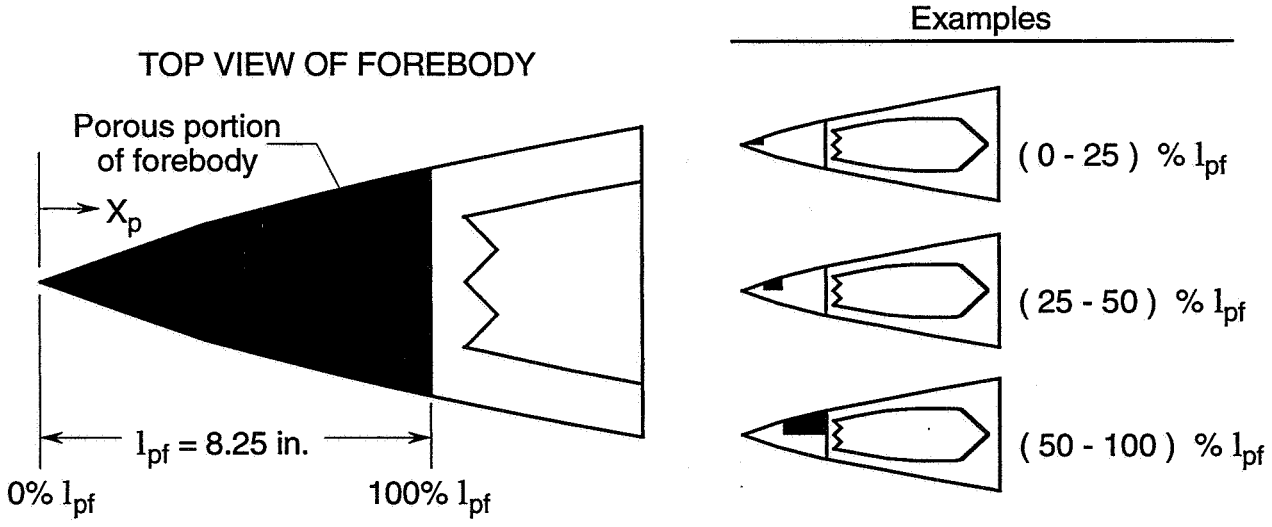

(b) X_p , variable used to designate chordwise porosity coverage.

Figure 9. Nomenclature used to describe porosity patterns. Shaded areas indicate porous regions.

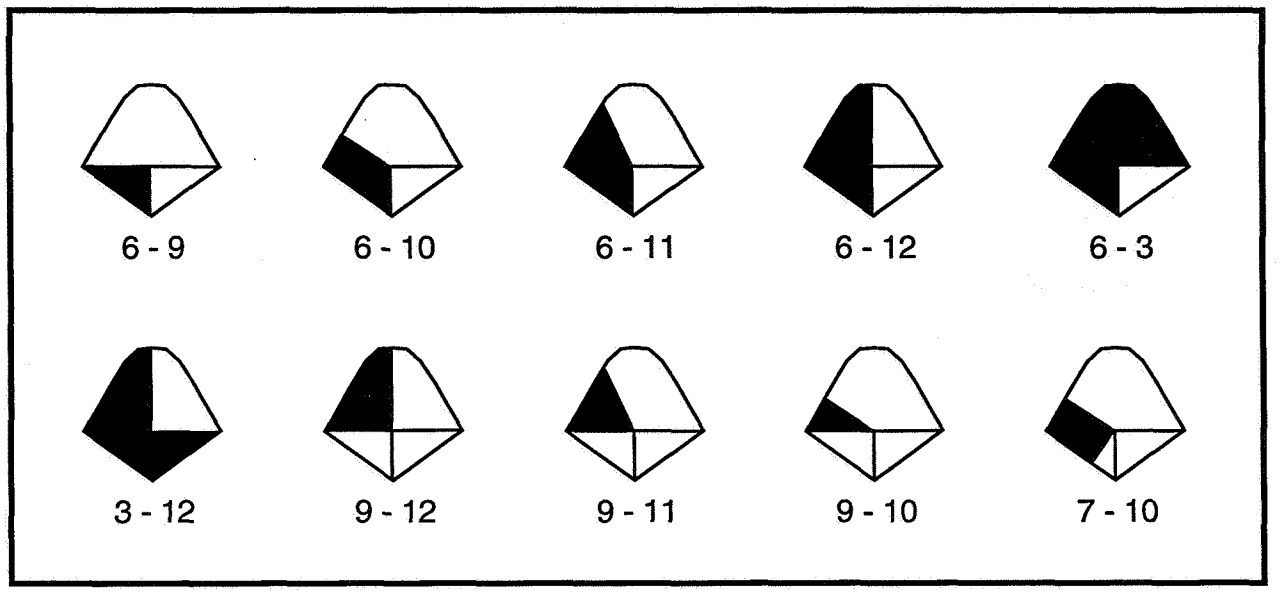

(a) Front view of forebody showing radial variations tested with X_p=(0-100)% l_{pf}.

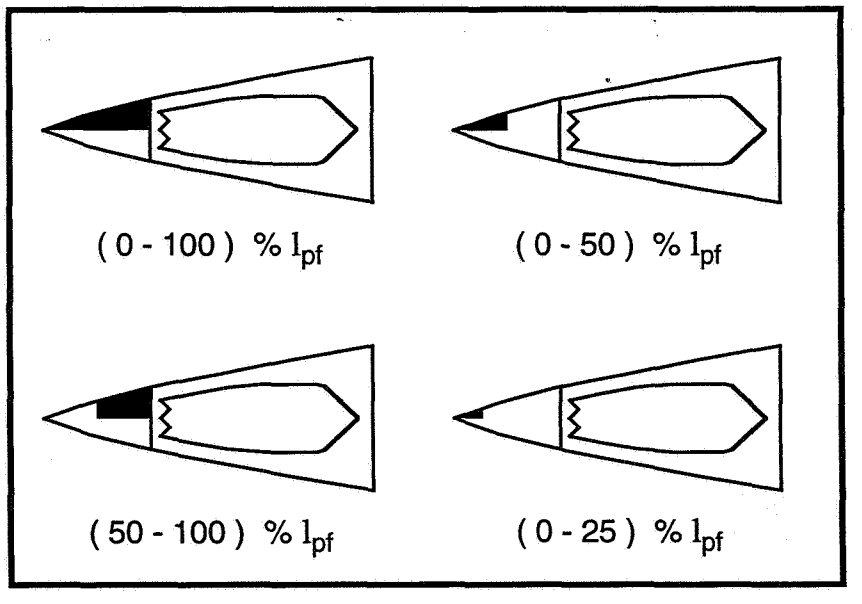

(b) Top view of forebody showing chordwise variations tested with Φ_p=6-12.

Figure 10. Regions of asymmetric forebody porosity tested on BMRF model. Shaded areas indicate porous regions.

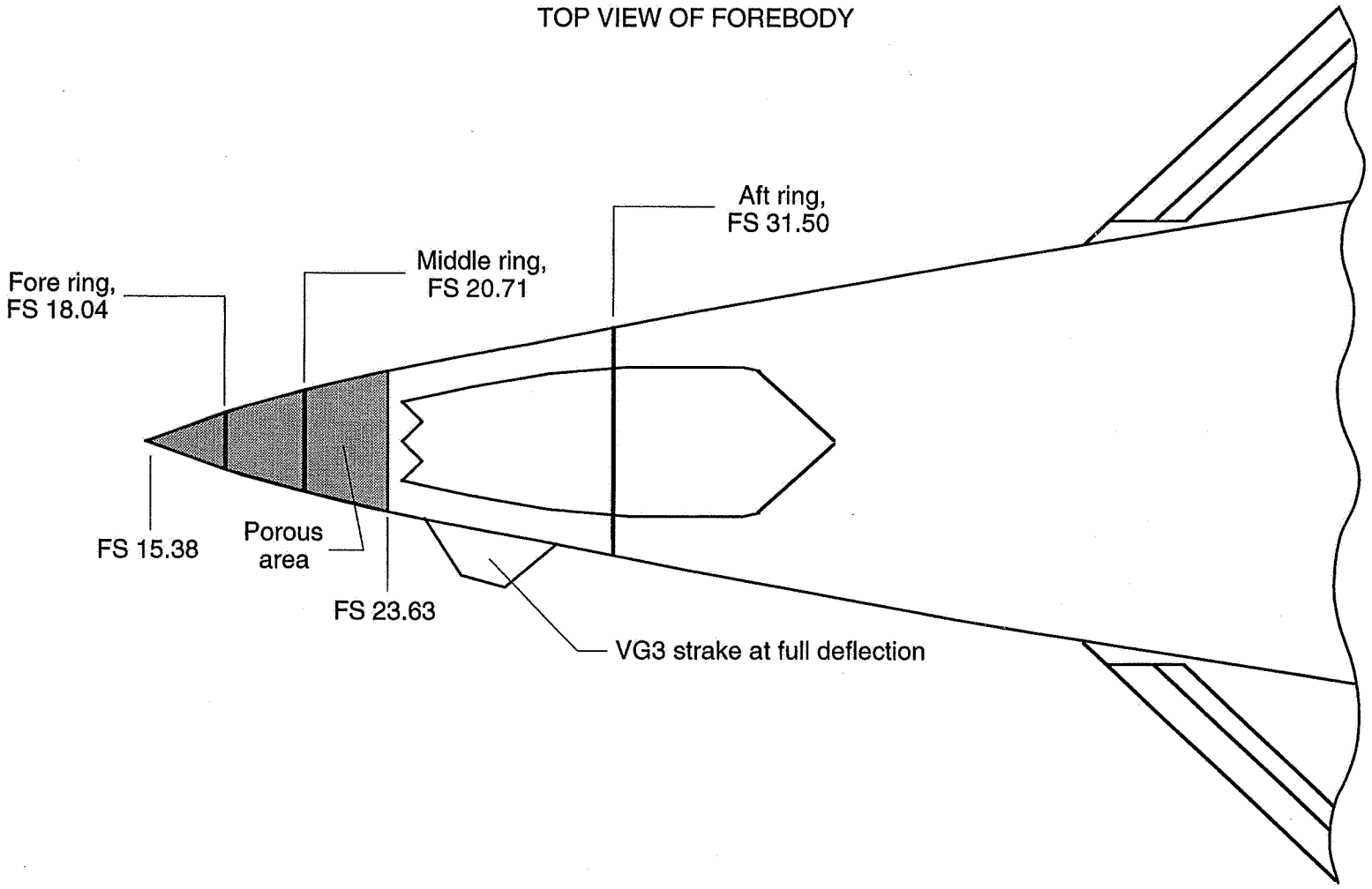

(a) Chordwise positions of pressure port rings.

Figure 11. Locations of static pressure ports.

FOREBODY CROSS SECTION AT FS 18.04

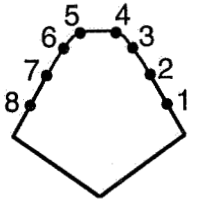

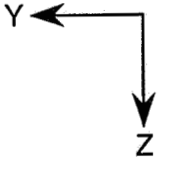

FOREBODY CROSS SECTION AT FS 20.71

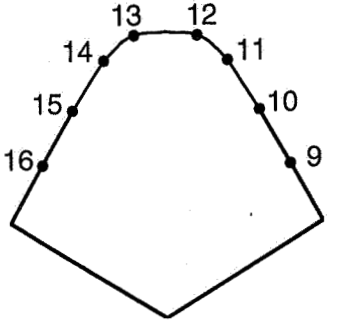

FORE RING

Port No.	FS, in.	BL, in.	WL, in.
1	18.04	-0.72	17.60
2	18.04	-0.54	17.91
3	18.04	-0.36	18.19
4	18.04	-0.18	18.35
5	18.04	0.18	18.35
6	18.04	0.36	18.19
7	18.04	0.54	17.91
8	18.04	0.72	17.60

MIDDLE RING

Port No.	FS, in.	BL, in.	WL, in.
9	20.71	-1.32	17.93
10	20.71	-0.99	18.51
11	20.71	-0.66	19.04
12	20.71	-0.33	19.30
13	20.71	0.33	19.30
14	20.71	0.66	19.04
15	20.71	0.99	18.51
16	20.71	1.32	17.93

(b) Coordinates of ports on fore and middle rings.

Figure 11. Continued.

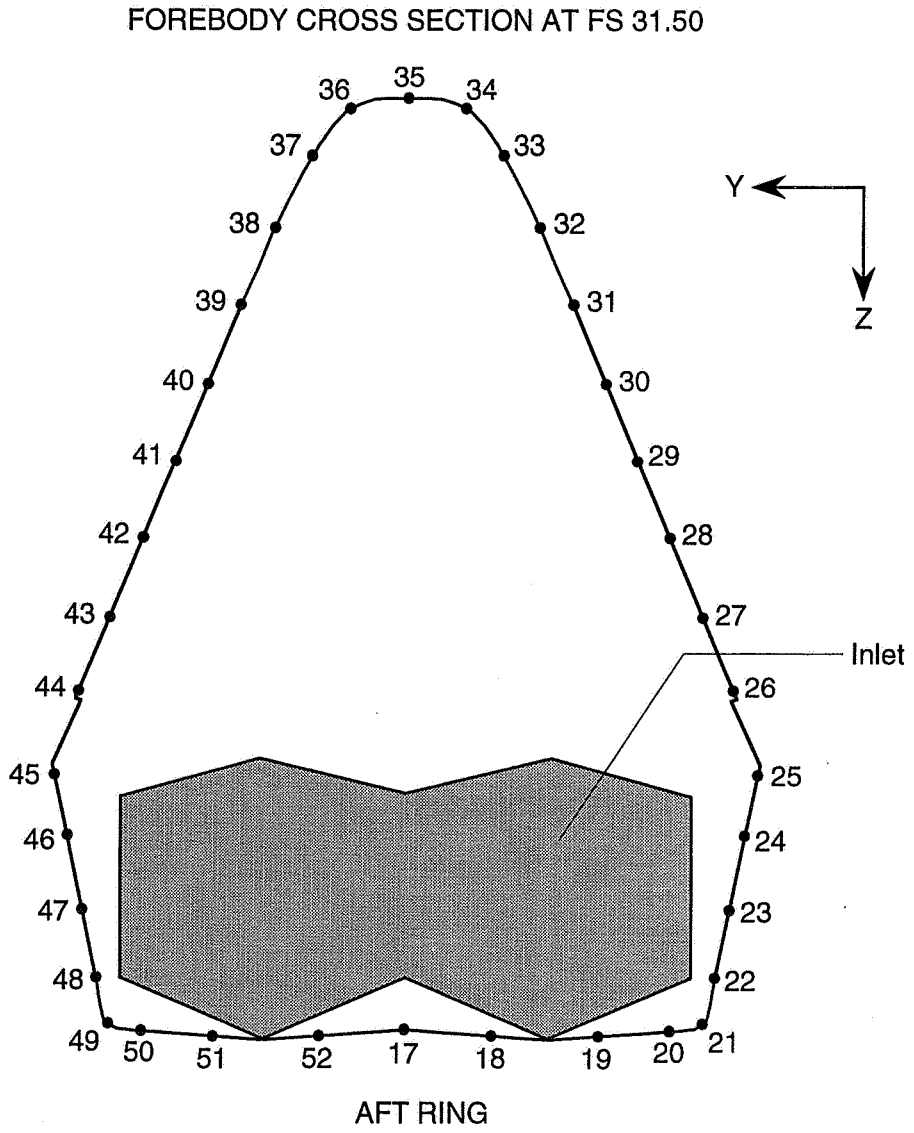

Port No.	FS, in.	BL, in.	WL, in.
17	31.50	0.00	13.63
18	31.50	-0.96	13.56
19	31.50	-2.10	13.56
20	31.50	-2.86	13.63
21	31.50	-3.23	13.69
22	31.50	-3.38	14.08
23	31.50	-3.54	14.90
24	31.50	-3.72	15.70
25	31.50	-3.86	16.48
26	31.50	-3.58	17.24
27	31.50	-3.24	18.10
28	31.50	-2.88	18.95
29	31.50	-2.52	19.80
30	31.50	-2.14	20.65
31	31.50	-1.78	21.50
32	31.50	-1.40	22.34
33	31.50	-1.00	23.12
34	31.50	-0.60	23.63
35	31.50	0.00	23.73
36	31.50	0.60	23.63
37	31.50	1.00	23.12
38	31.50	1.40	22.34
39	31.50	1.78	21.50
40	31.50	2.14	20.65
41	31.50	2.52	19.80
42	31.50	2.88	18.95
43	31.50	3.24	18.10
44	31.50	3.58	17.24
45	31.50	3.86	16.48
46	31.50	3.72	15.70
47	31.50	3.54	14.90
48	31.50	3.38	14.08
49	31.50	3.23	13.69
50	31.50	2.86	13.63
51	31.50	2.10	13.56
52	31.50	0.96	13.56

(c) Coordinates of ports on aft ring.

Figure 11. Concluded.

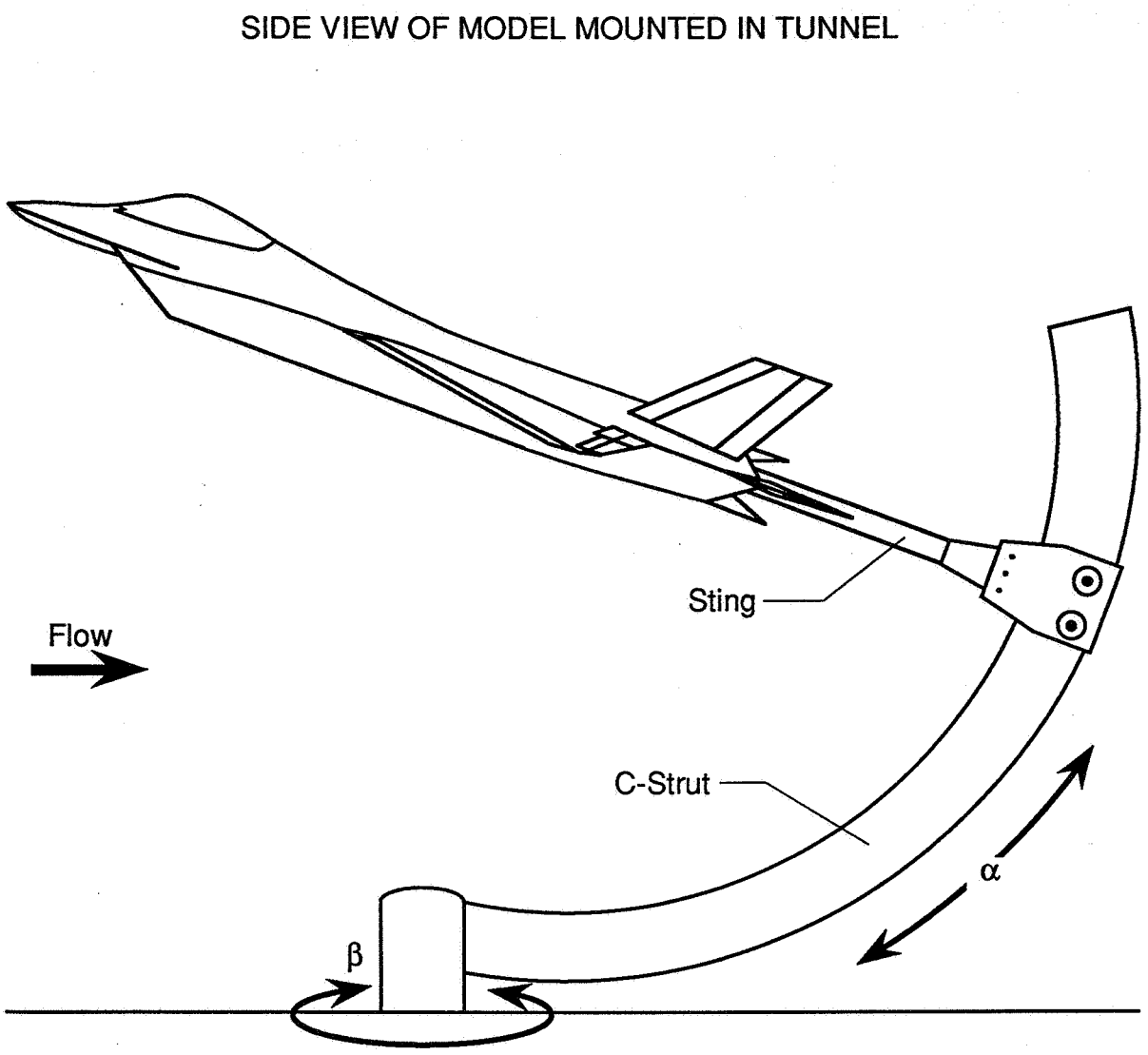

Figure 12. Model-mounting hardware and actuation mechanism. Not to scale.

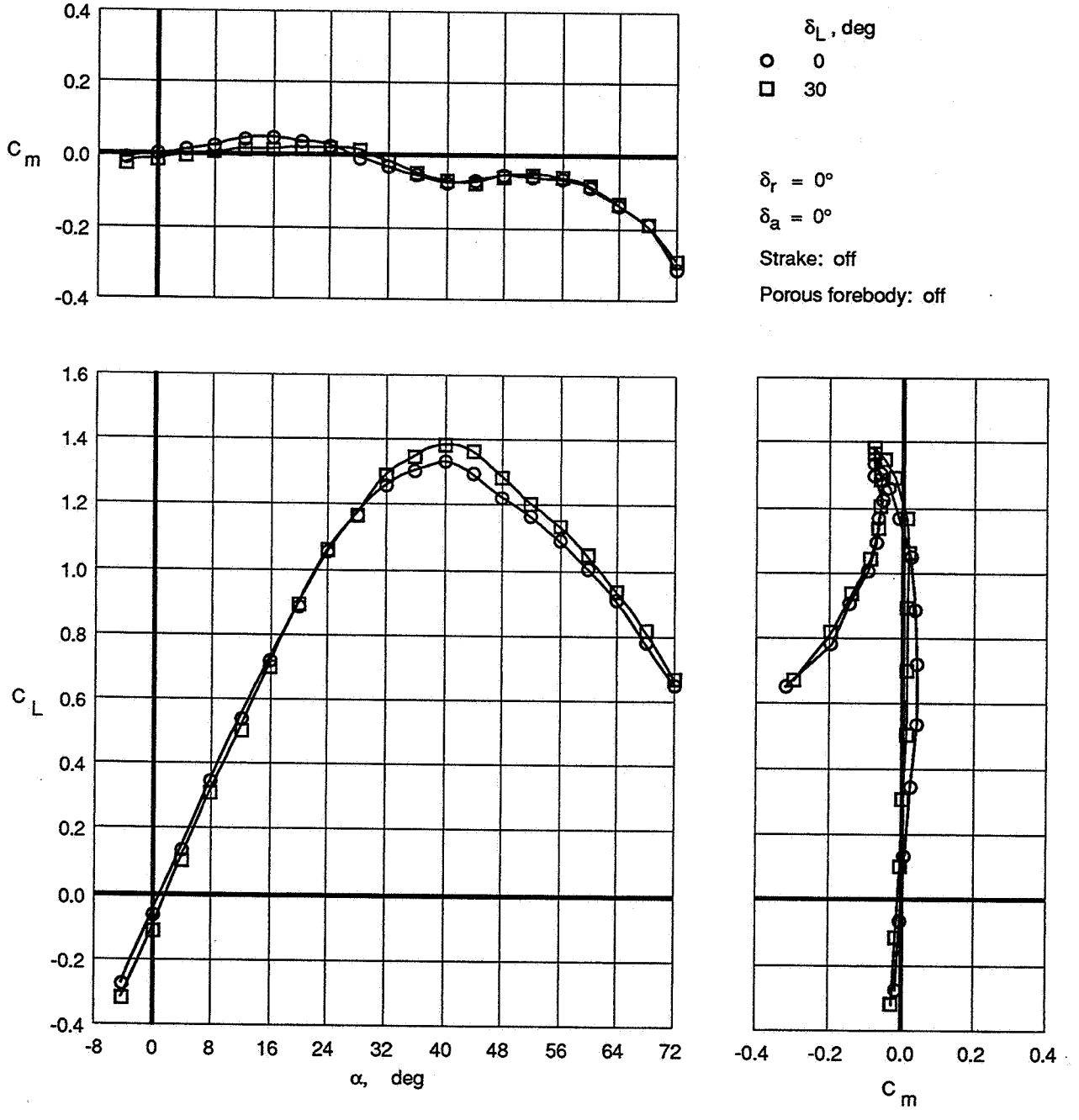

(a) Longitudinal characteristics.

Figure 13. Effect of leading-edge flap deflections on BMRF configuration.

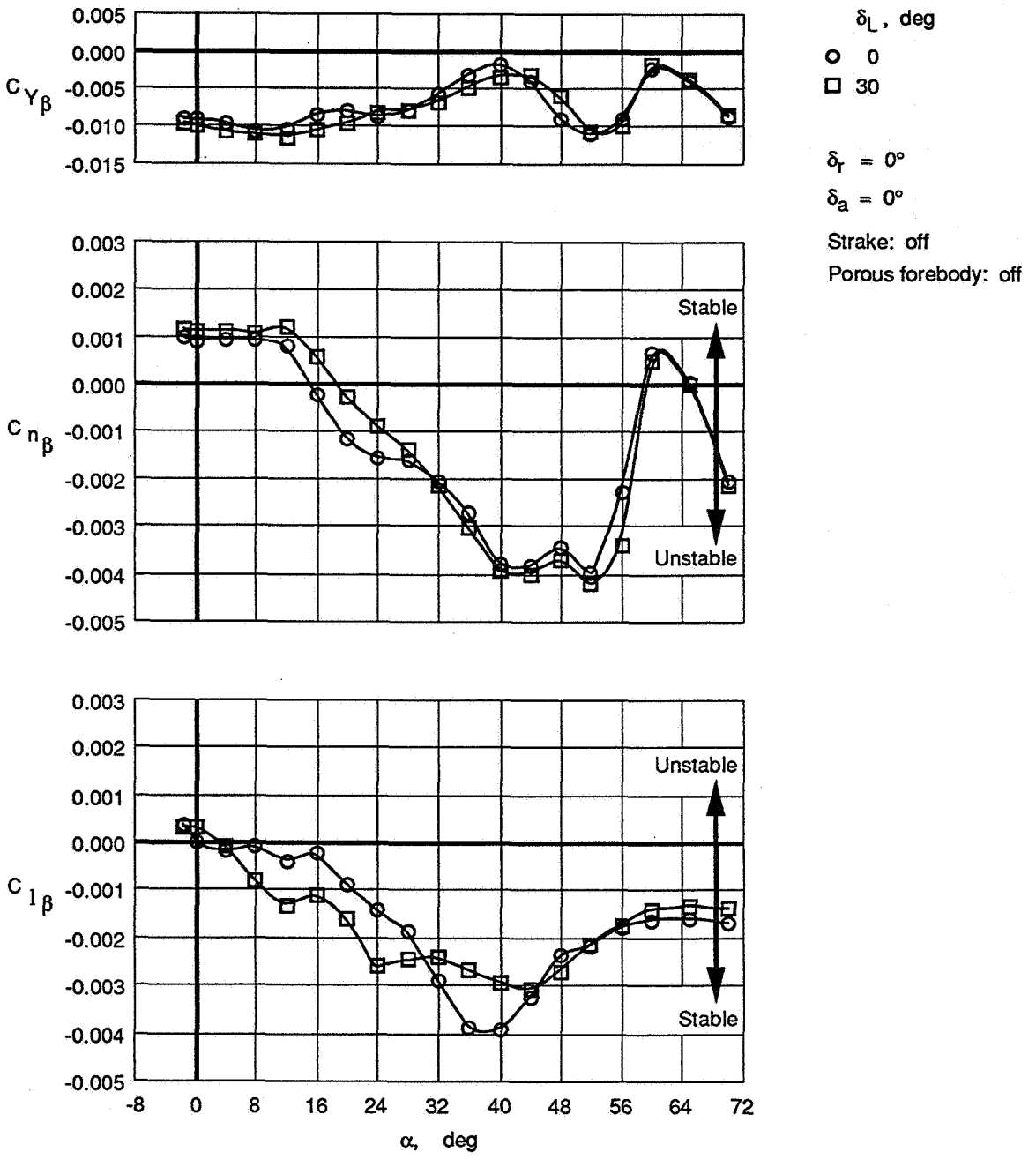

(b) Lateral-directional stability.

Figure 13. Concluded.

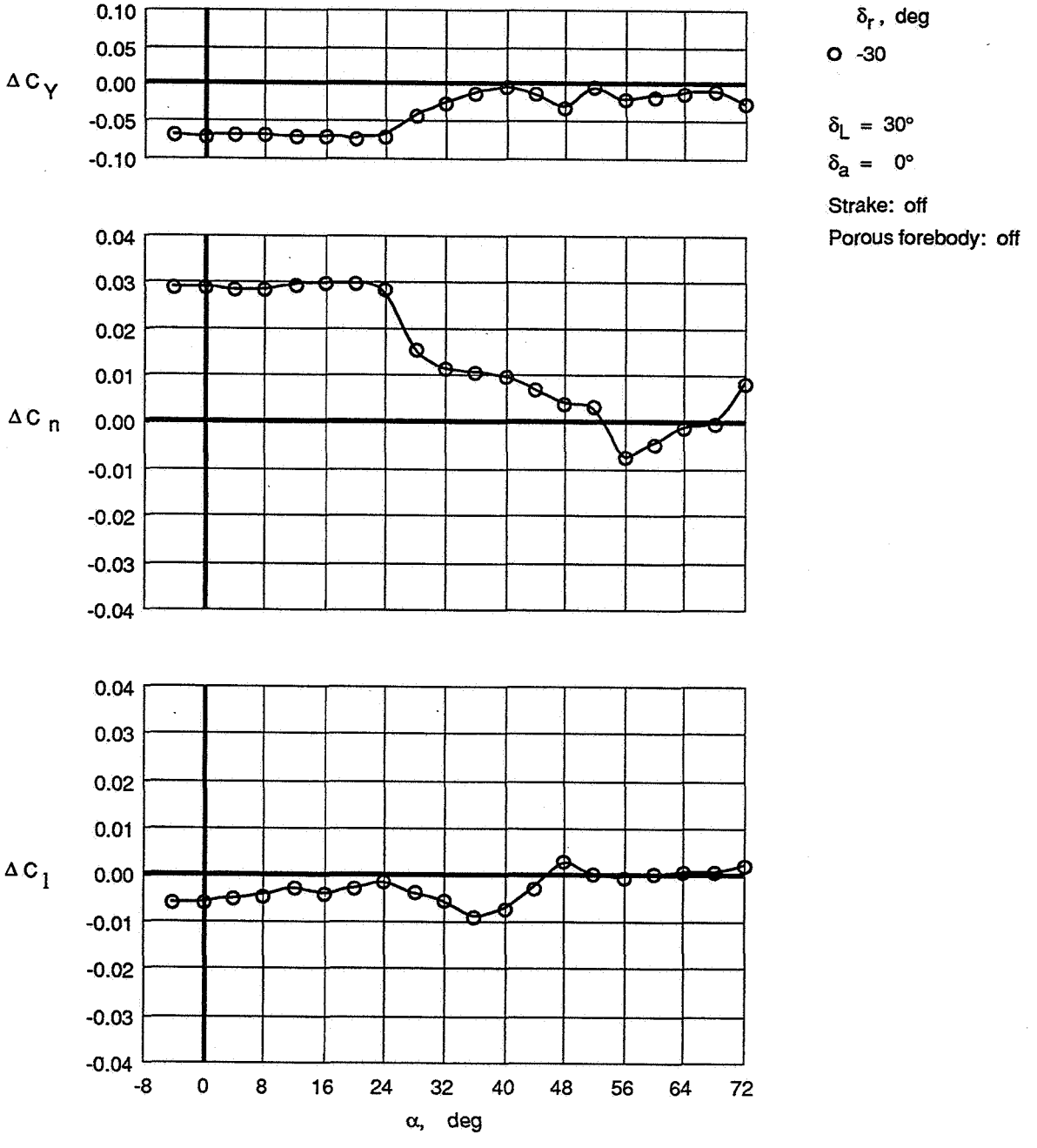

Figure 14. Control effectiveness of rudder deflection on BMRF configuration.

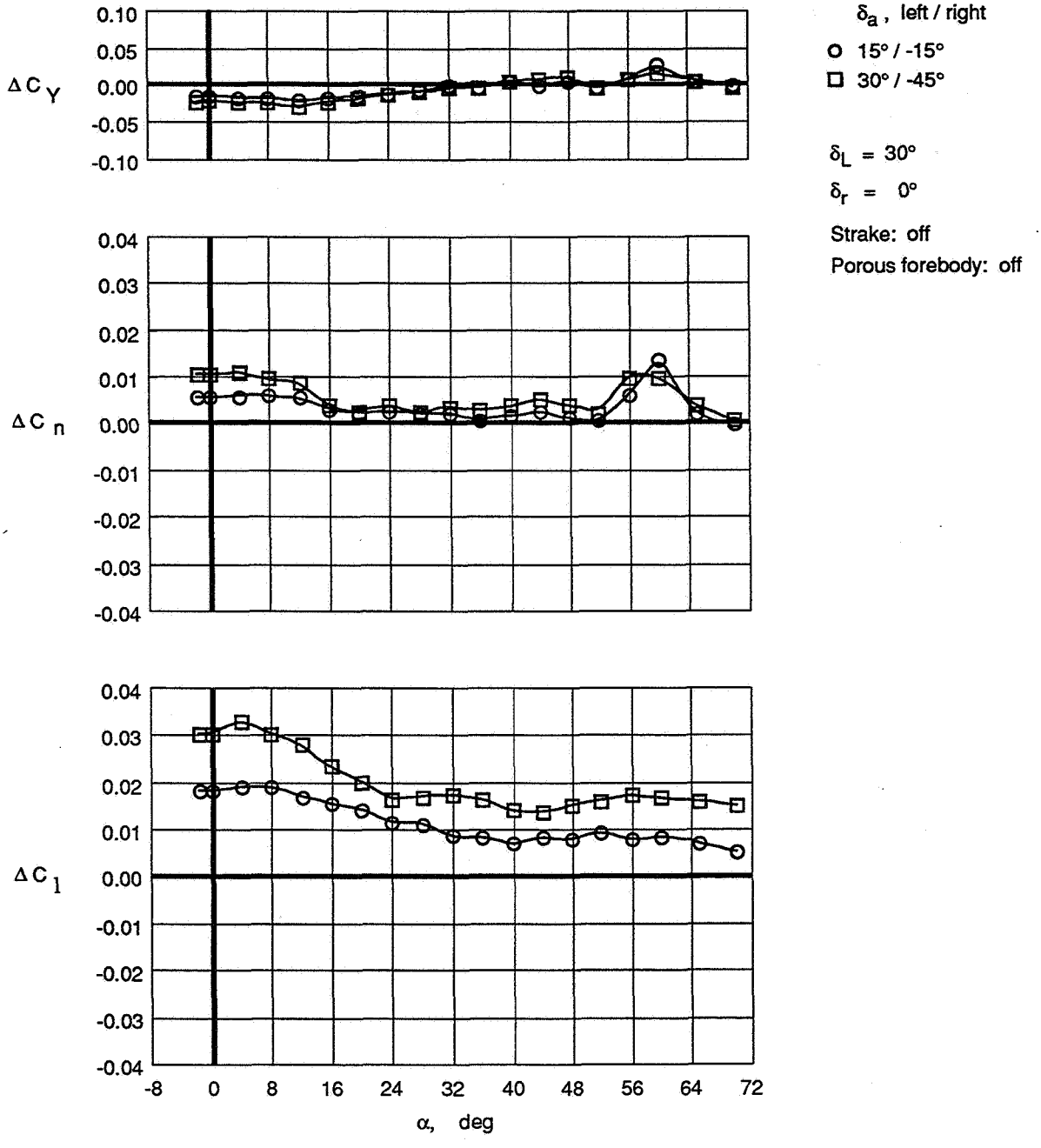

Figure 15. Control effectiveness of aileron deflections on BMRF configuration.

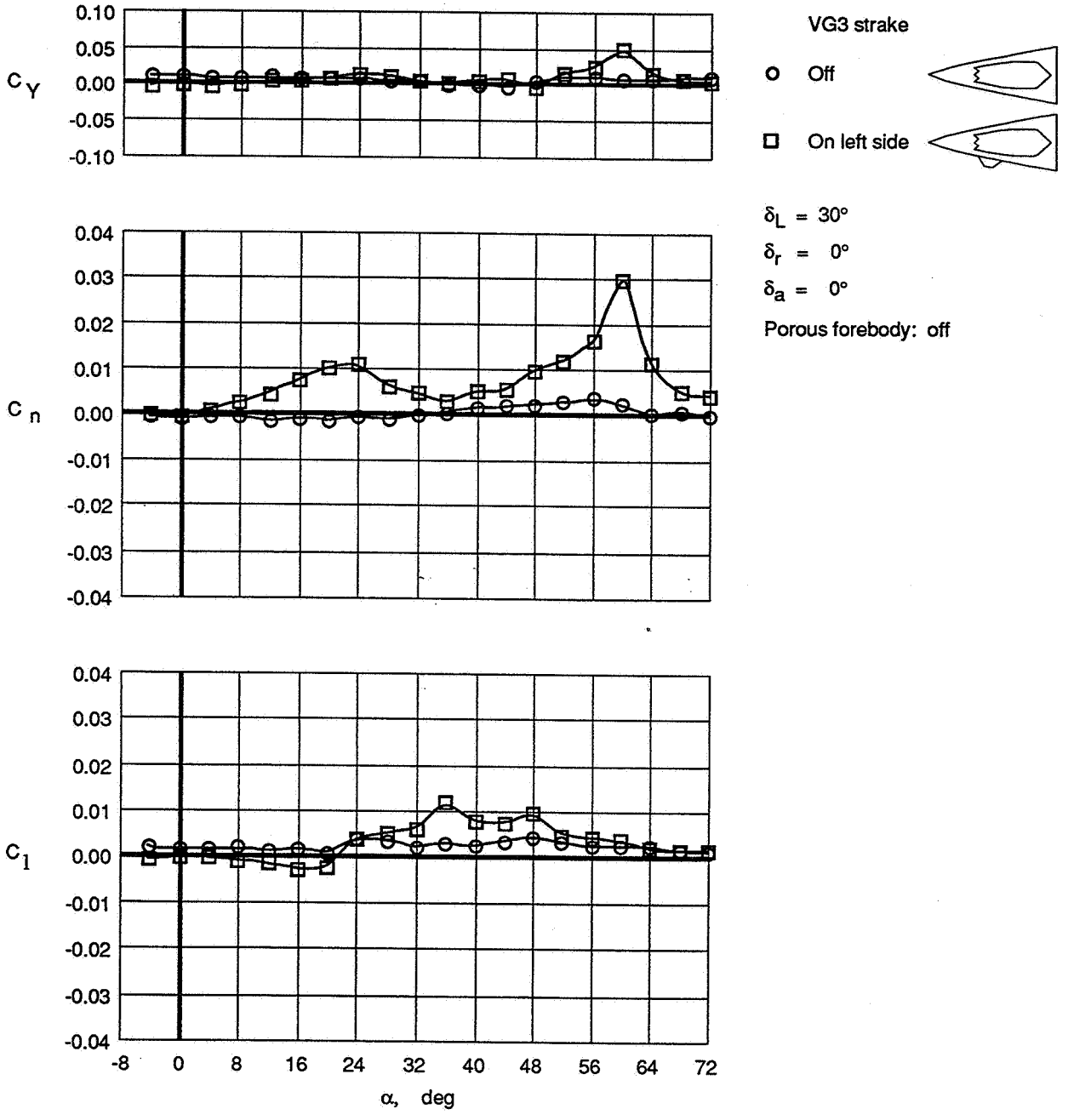

(a) Lateral-directional characteristics.

Figure 16. Effect of VG3 strake mounted on left side of forebody.

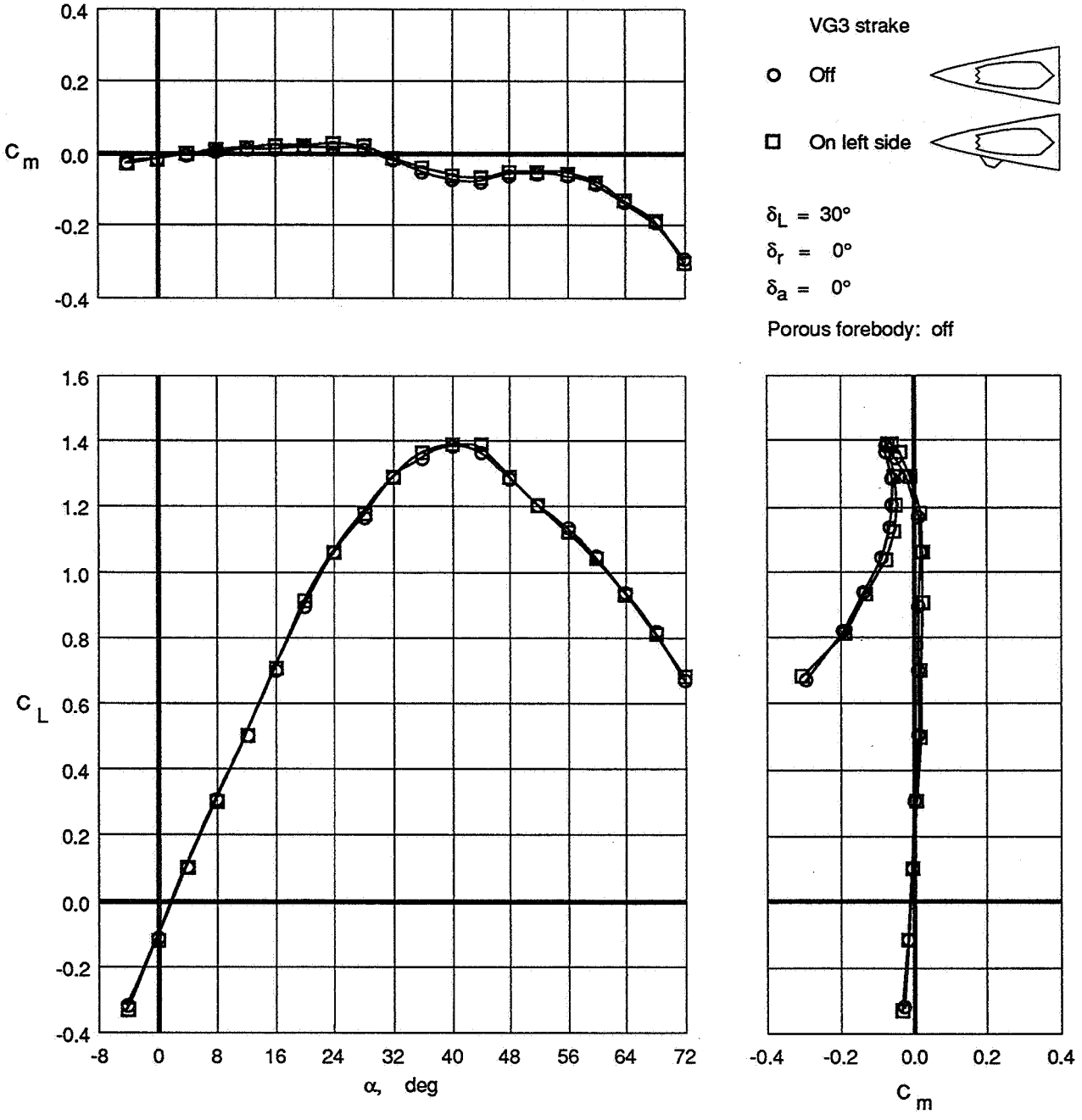

(b) Longitudinal characteristics.

Figure 16. Concluded.

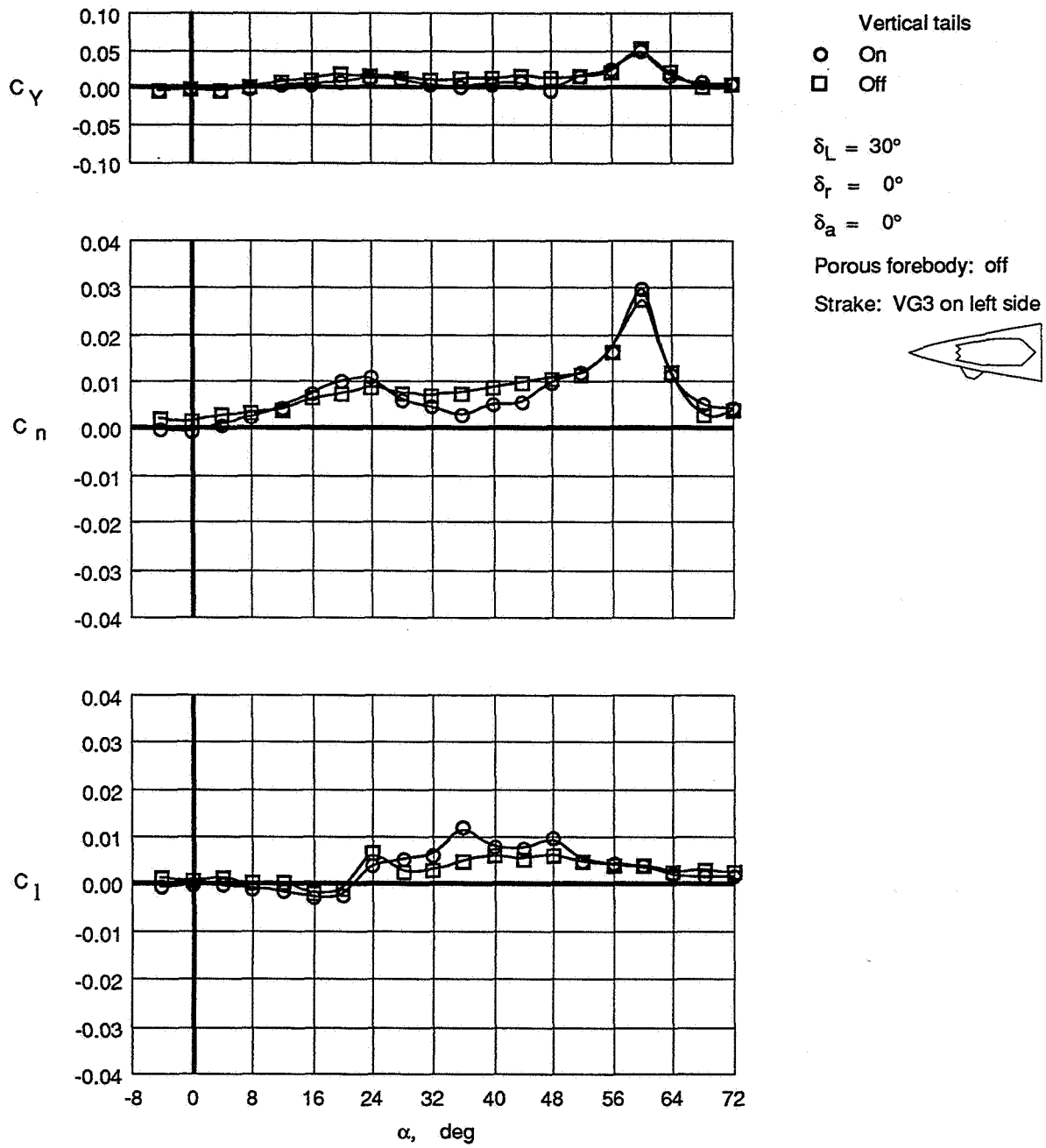

(a) Lateral-directional characteristics.

Figure 17. Effect of removing vertical tails on VG3 strake configuration.

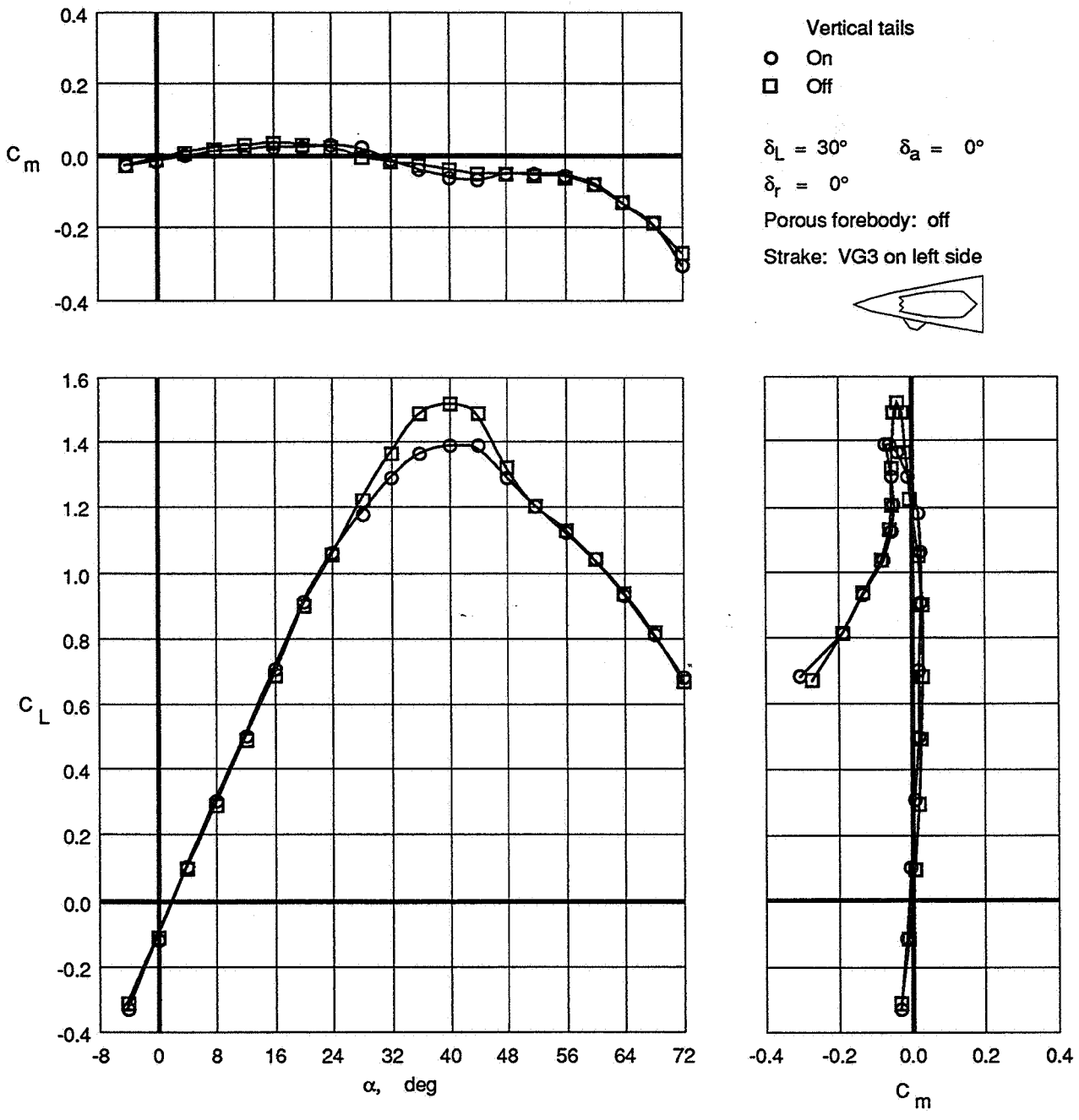

(b) Longitudinal characteristics.

Figure 17. Concluded.

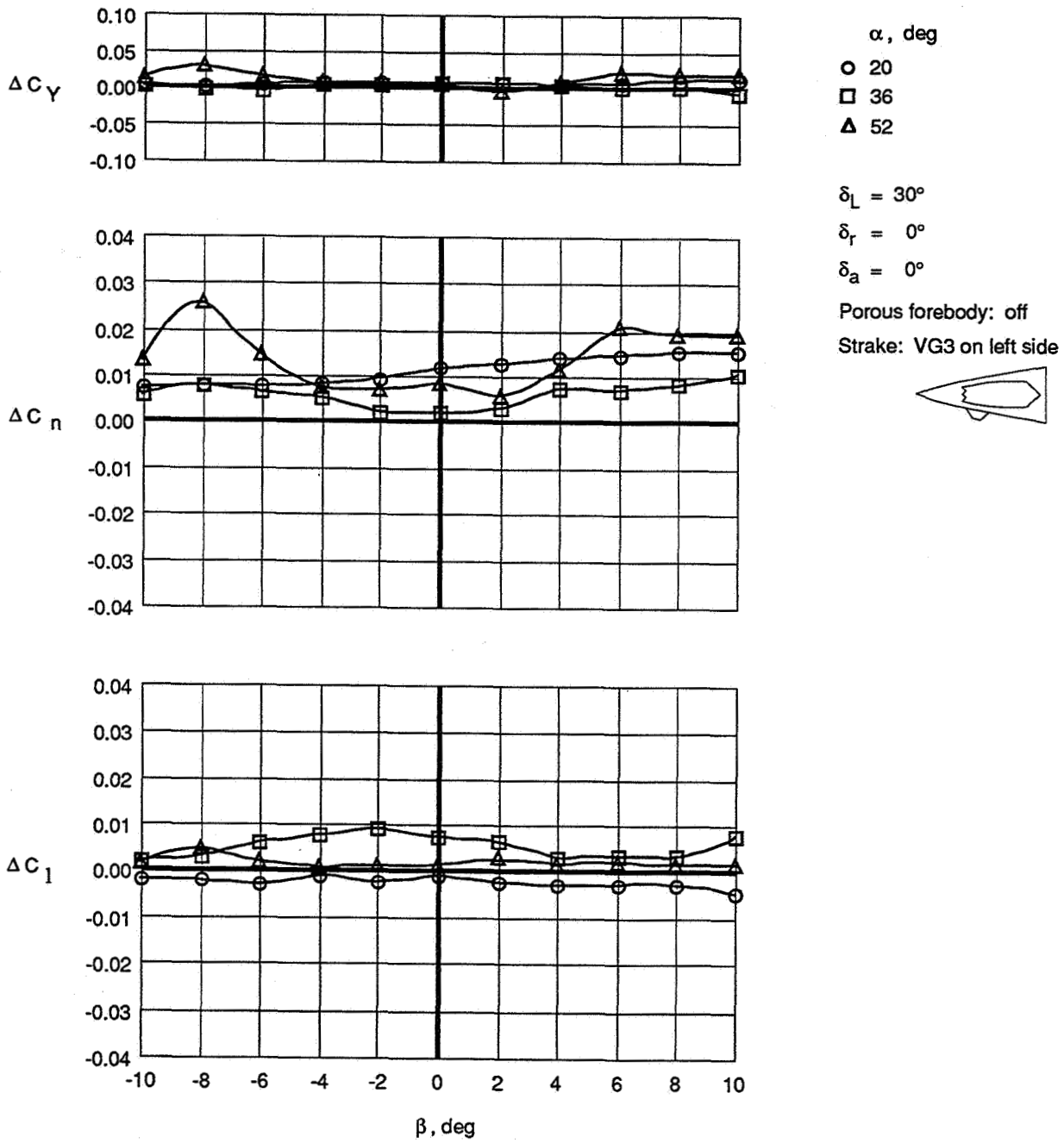

Figure 18. Effect of sideslip on effectiveness of VG3 strake.

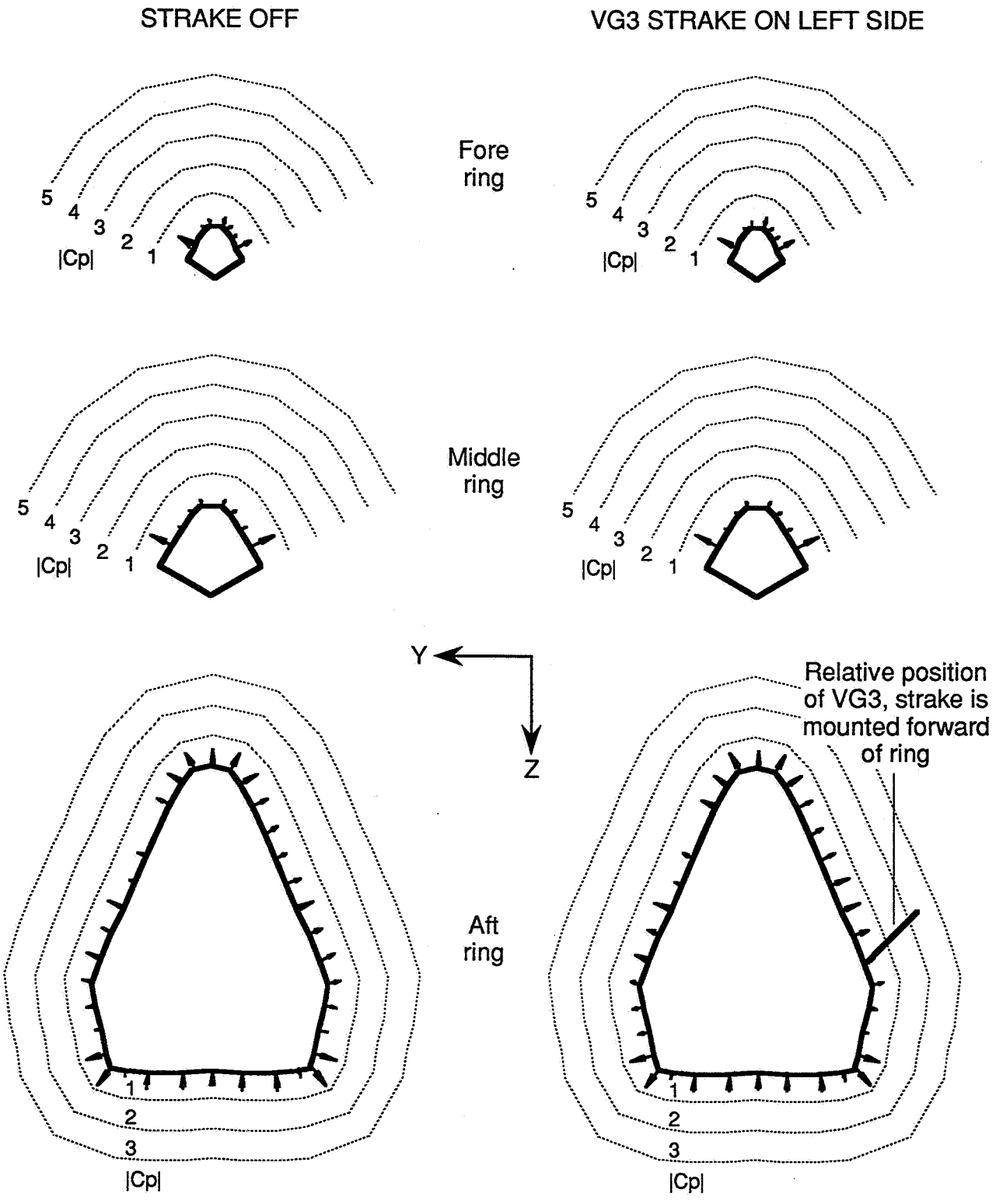

(a) α=24°, β=0°.

Figure 19. Comparison of pressure data with VG3 strake off and deployed on left side of forebody.

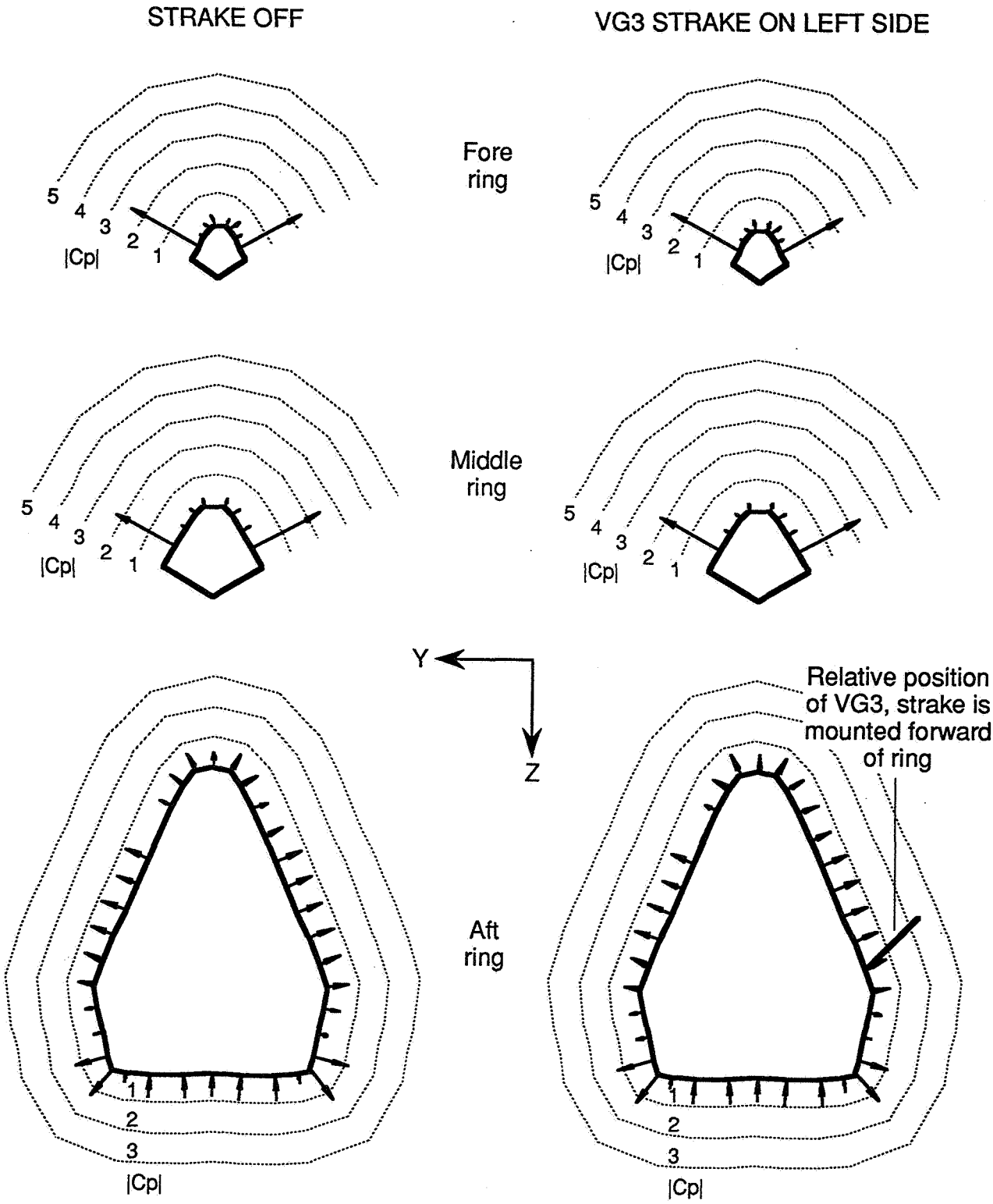

(b) α=36°, β=0°.

Figure 19. Continued.

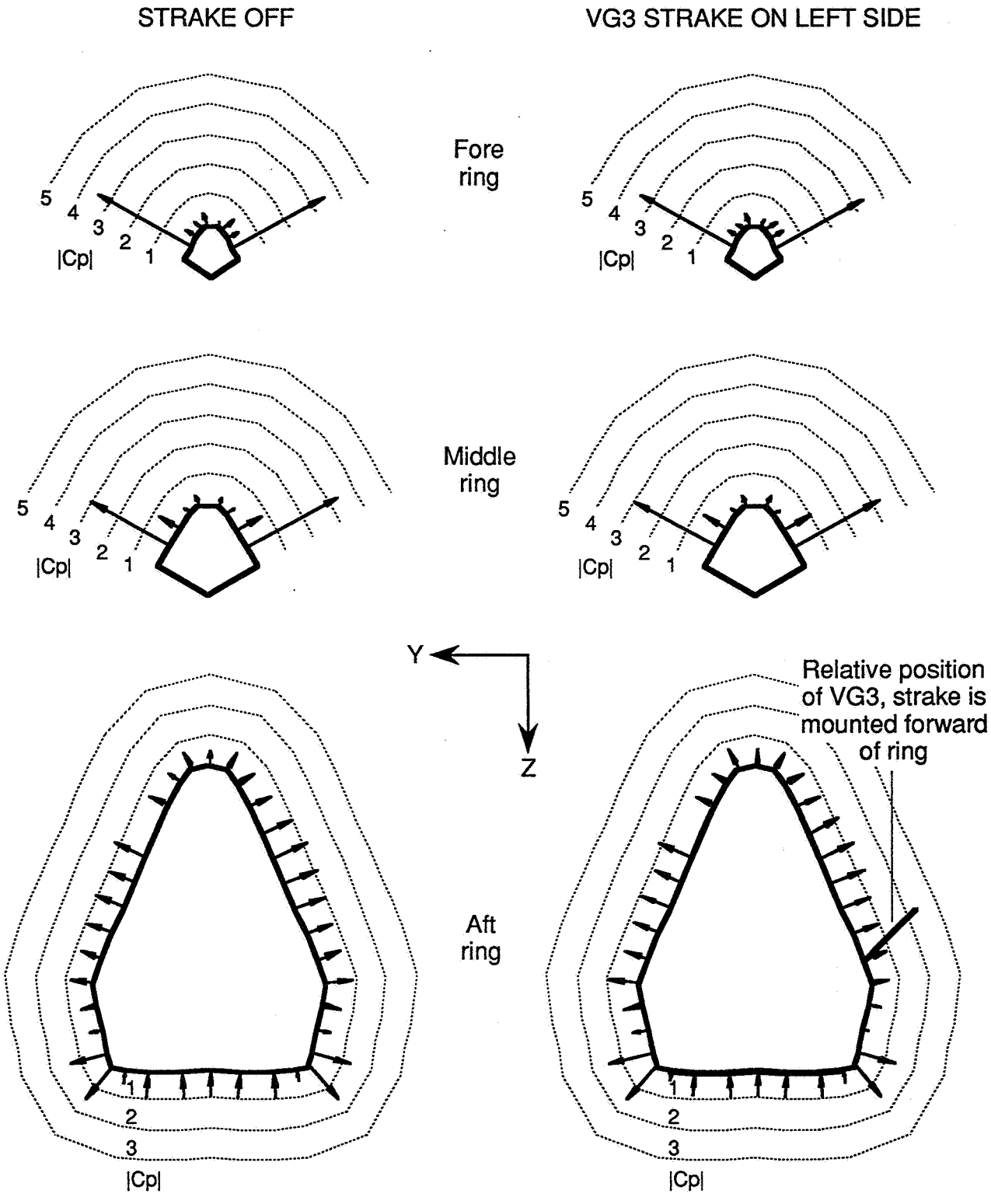

(c) α=44°, β=0°.

Figure 19. Continued.

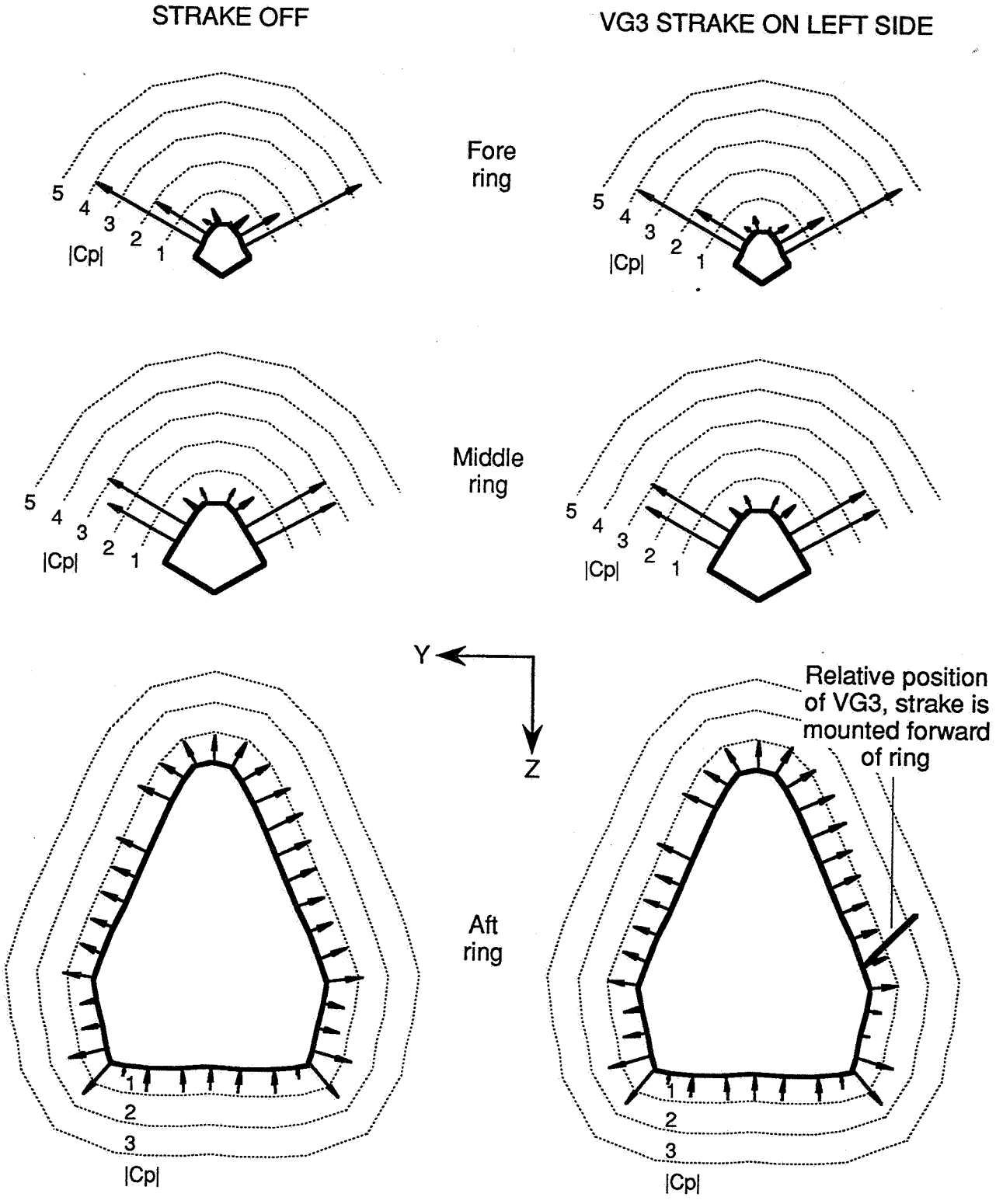

(d) α=52°, β=0°.

Figure 19. Continued.

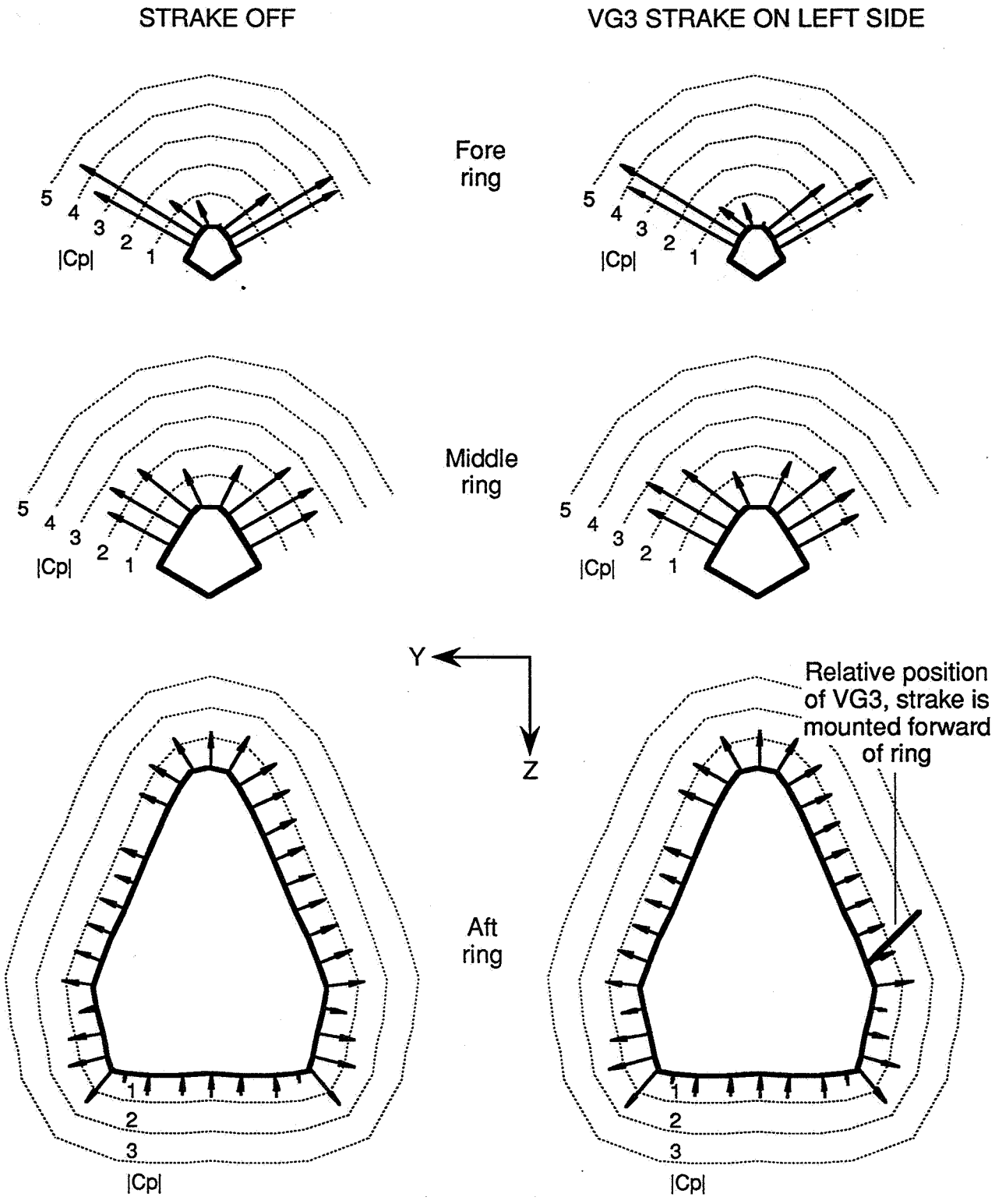

(e) α=60°, β=0°.

Figure 19. Continued.

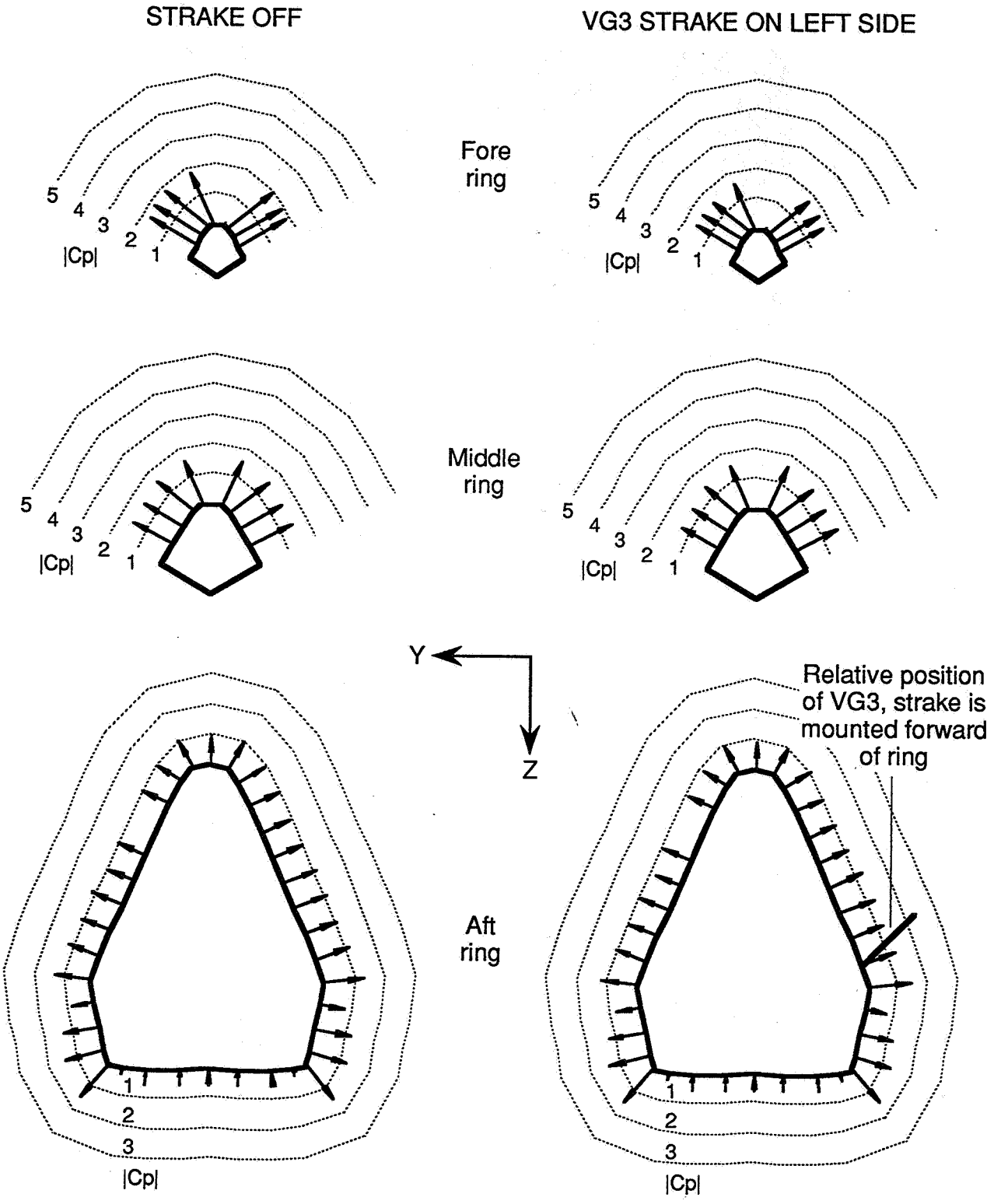

(f) α=68°, β=0°.

Figure 19. Concluded.

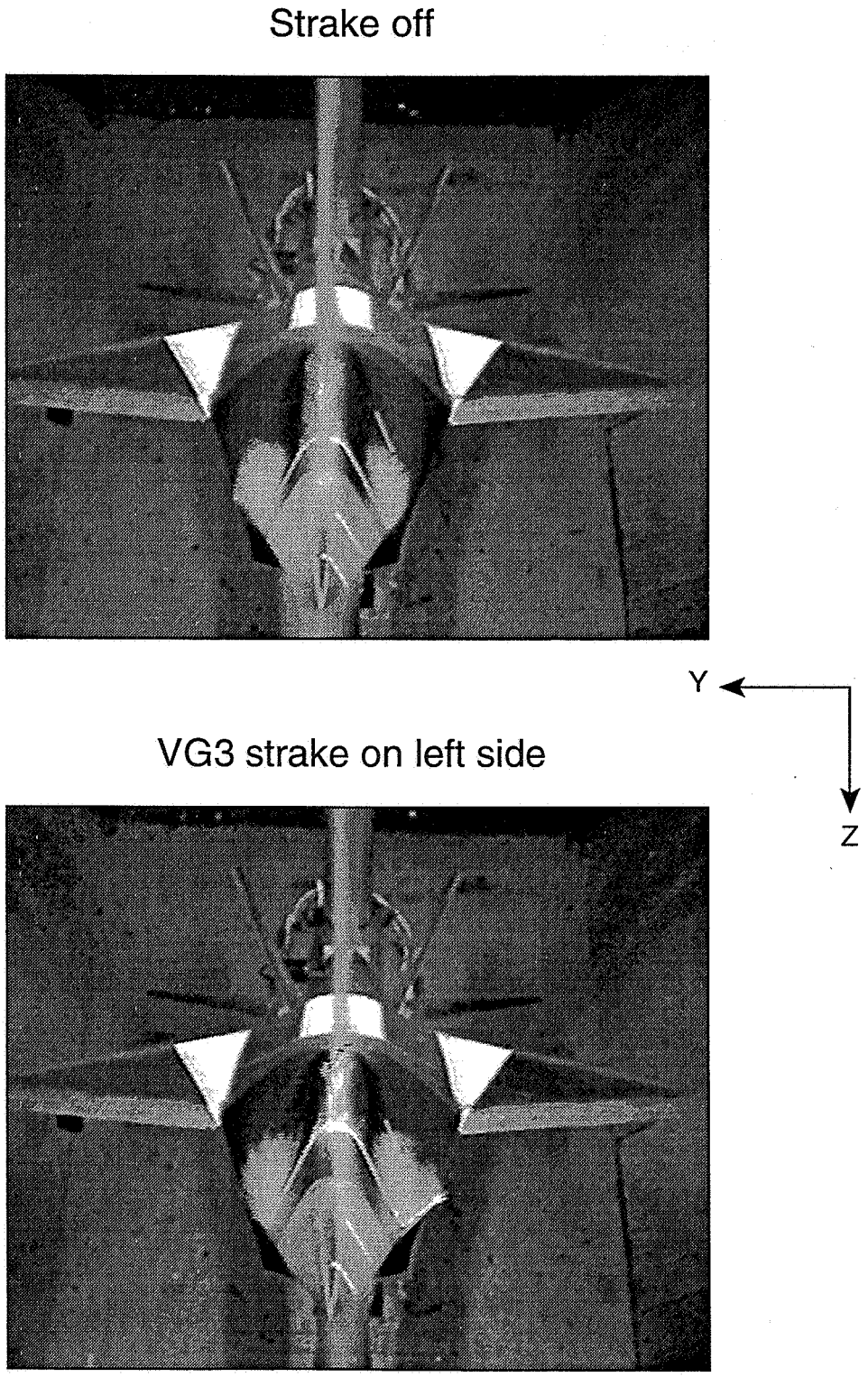

(a) α=44°, β=0°.

Figure 20. Comparison of flow visualization with VG3 strake off and deployed on left side of forebody.

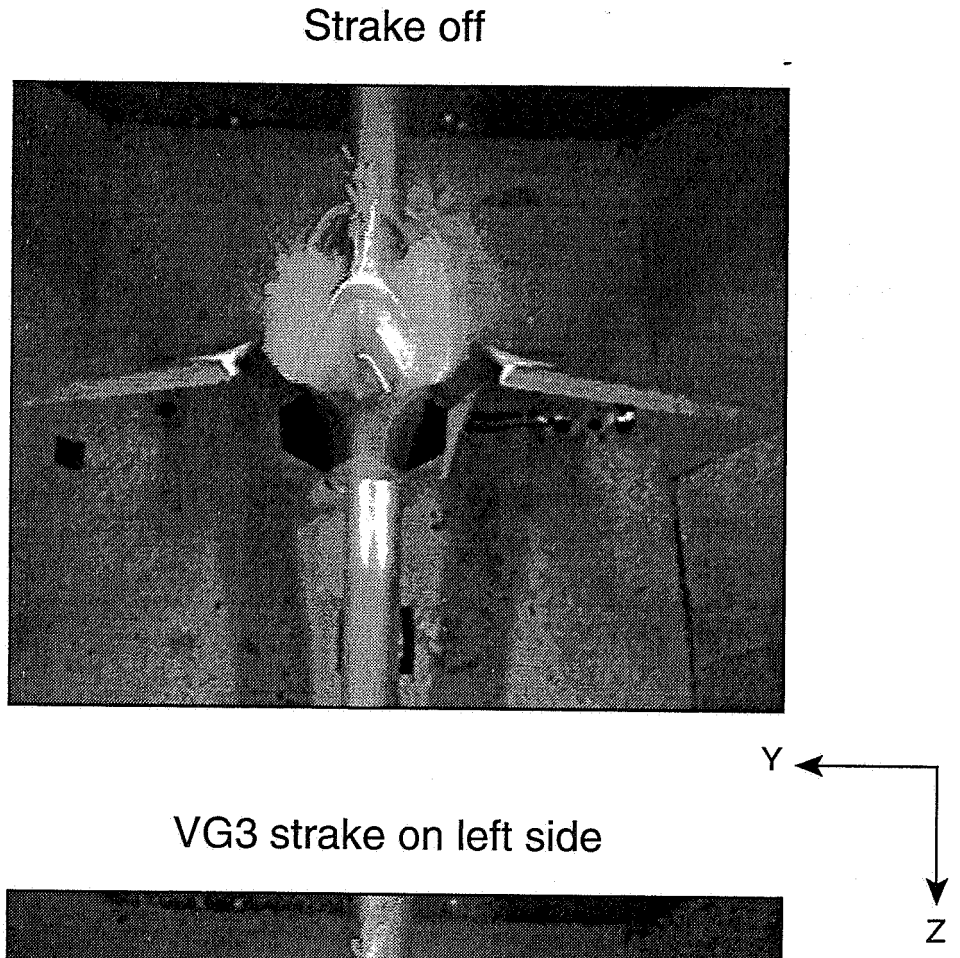

(b) α=52°, β=0°.

Figure 20. Concluded.

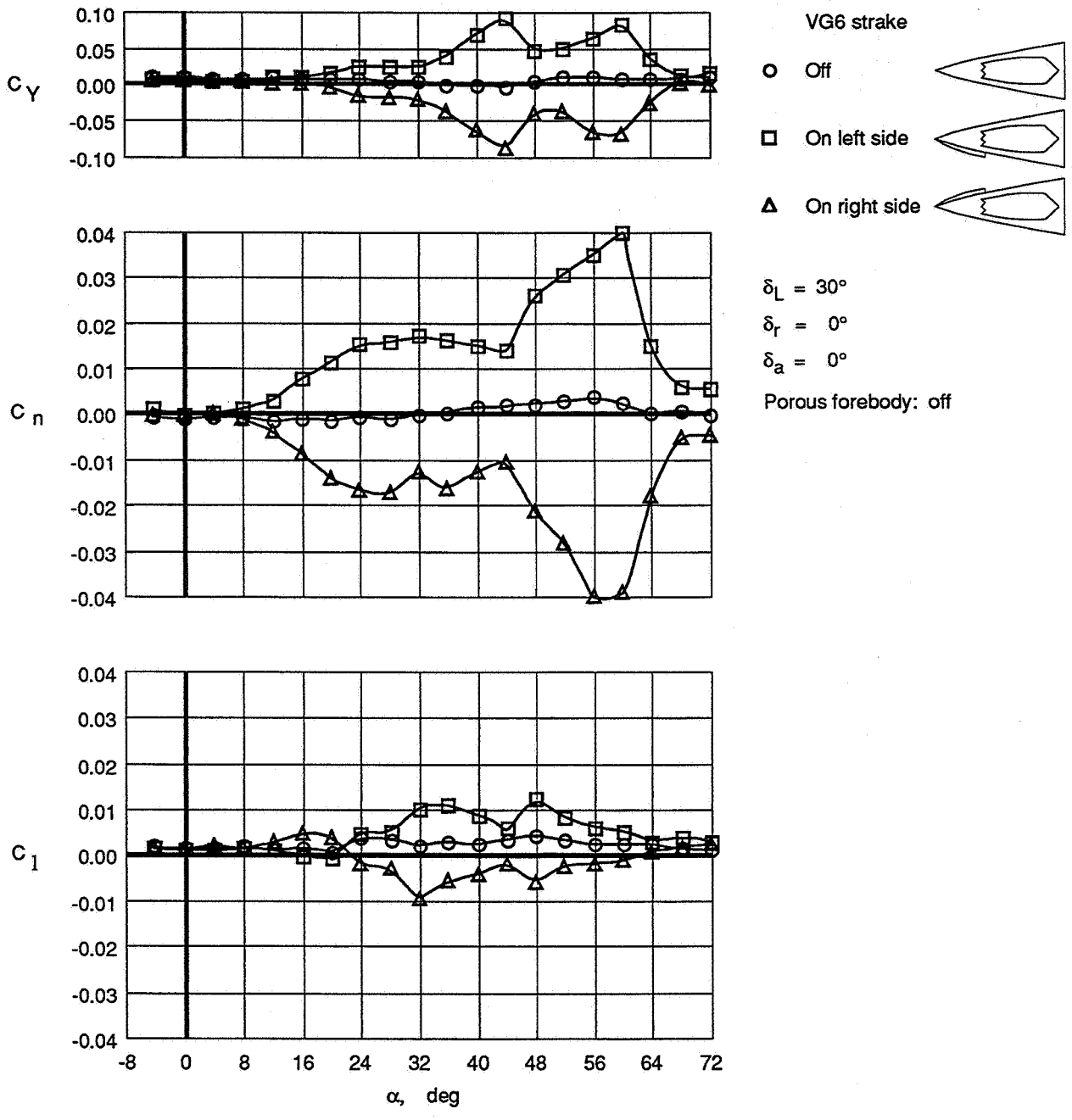

(a) Lateral-directional characteristics.

Figure 21. Effect of VG6 strake when mounted on either left or right side of forebody.

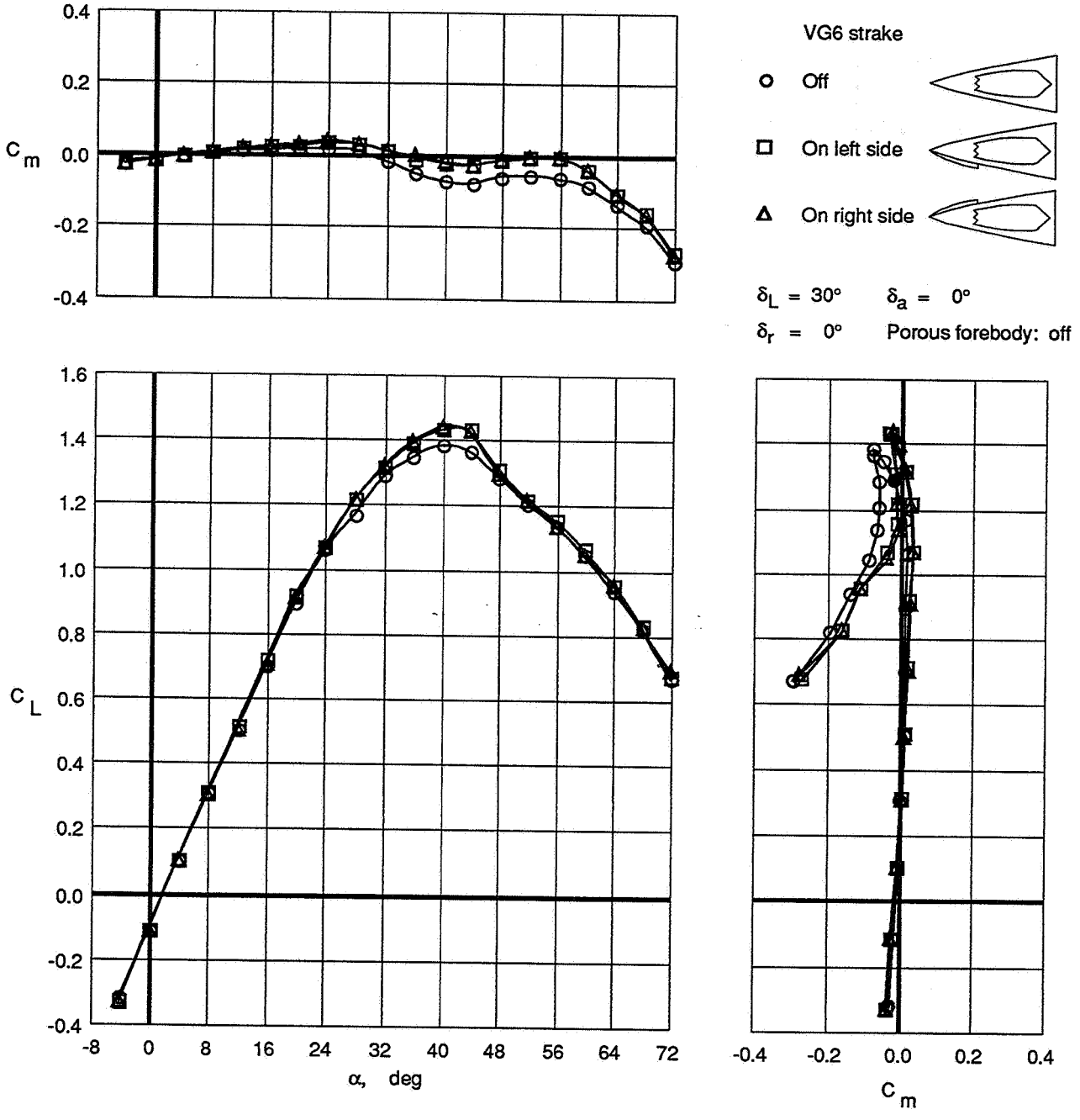

(b) Longitudinal characteristics.

Figure 21. Concluded.

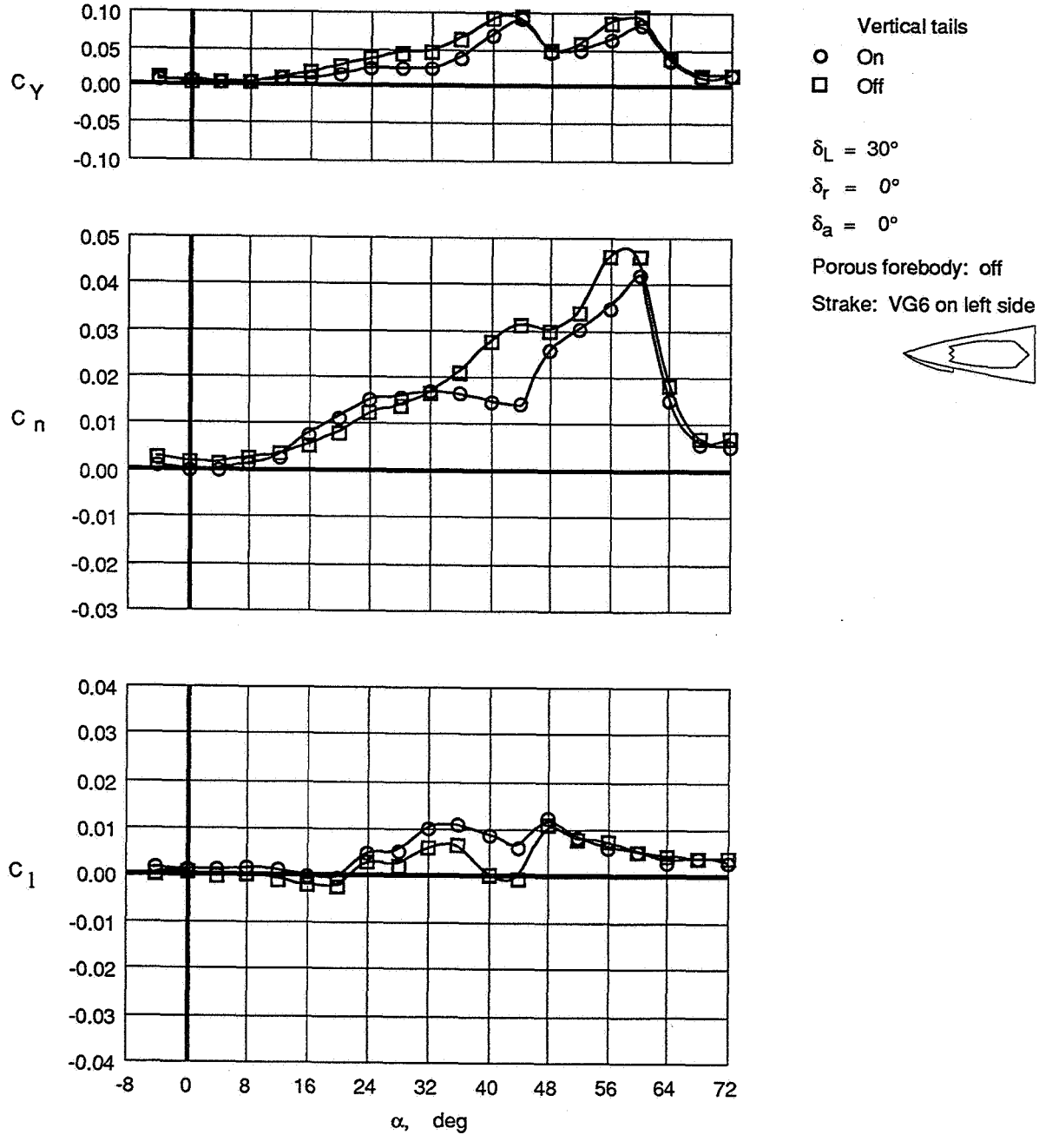

(a) Lateral-directional characteristics.

Figure 22. Effect of removing vertical tails on VG6 strake configuration.

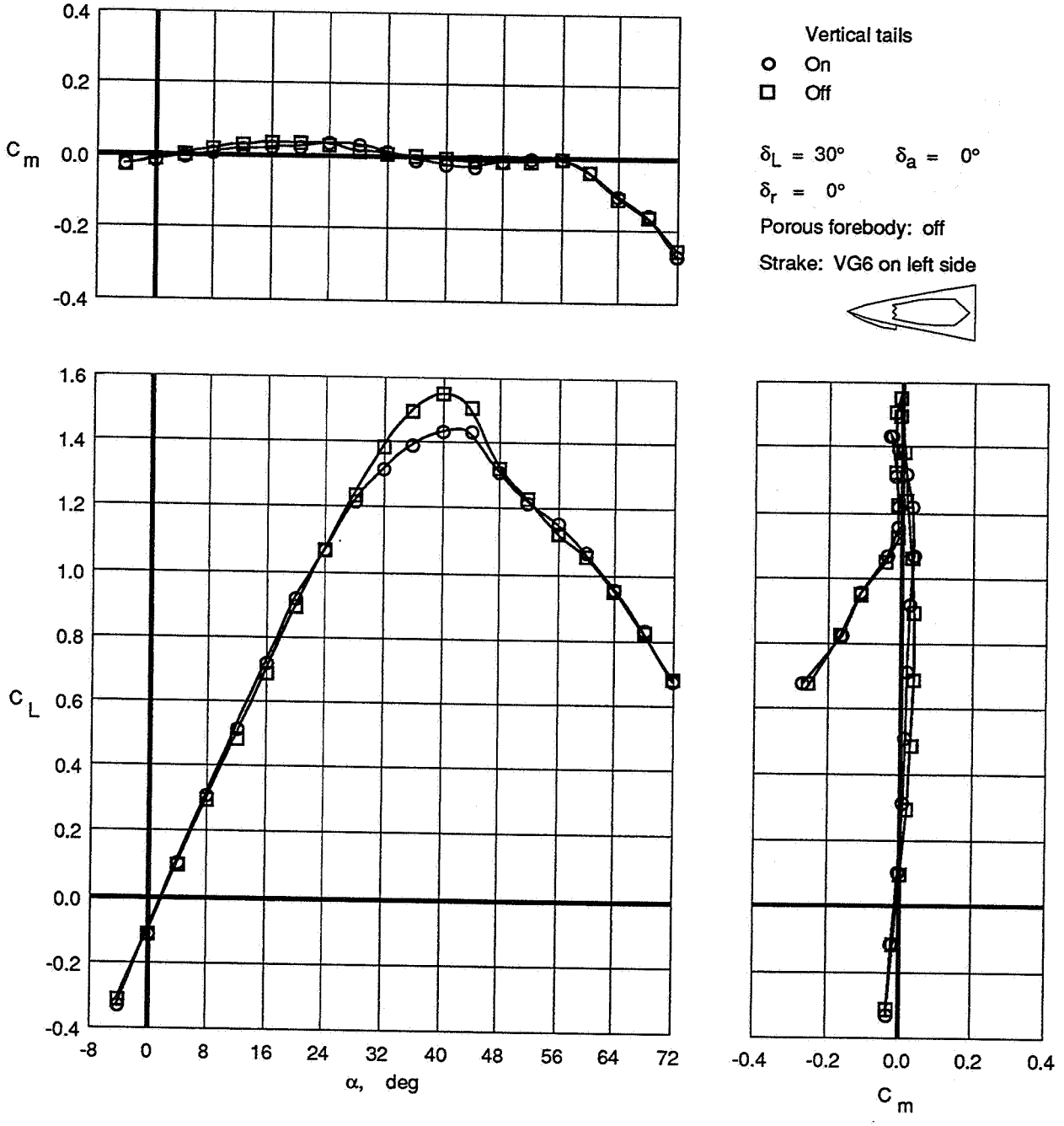

(b) Longitudinal characteristics.

Figure 22. Concluded.

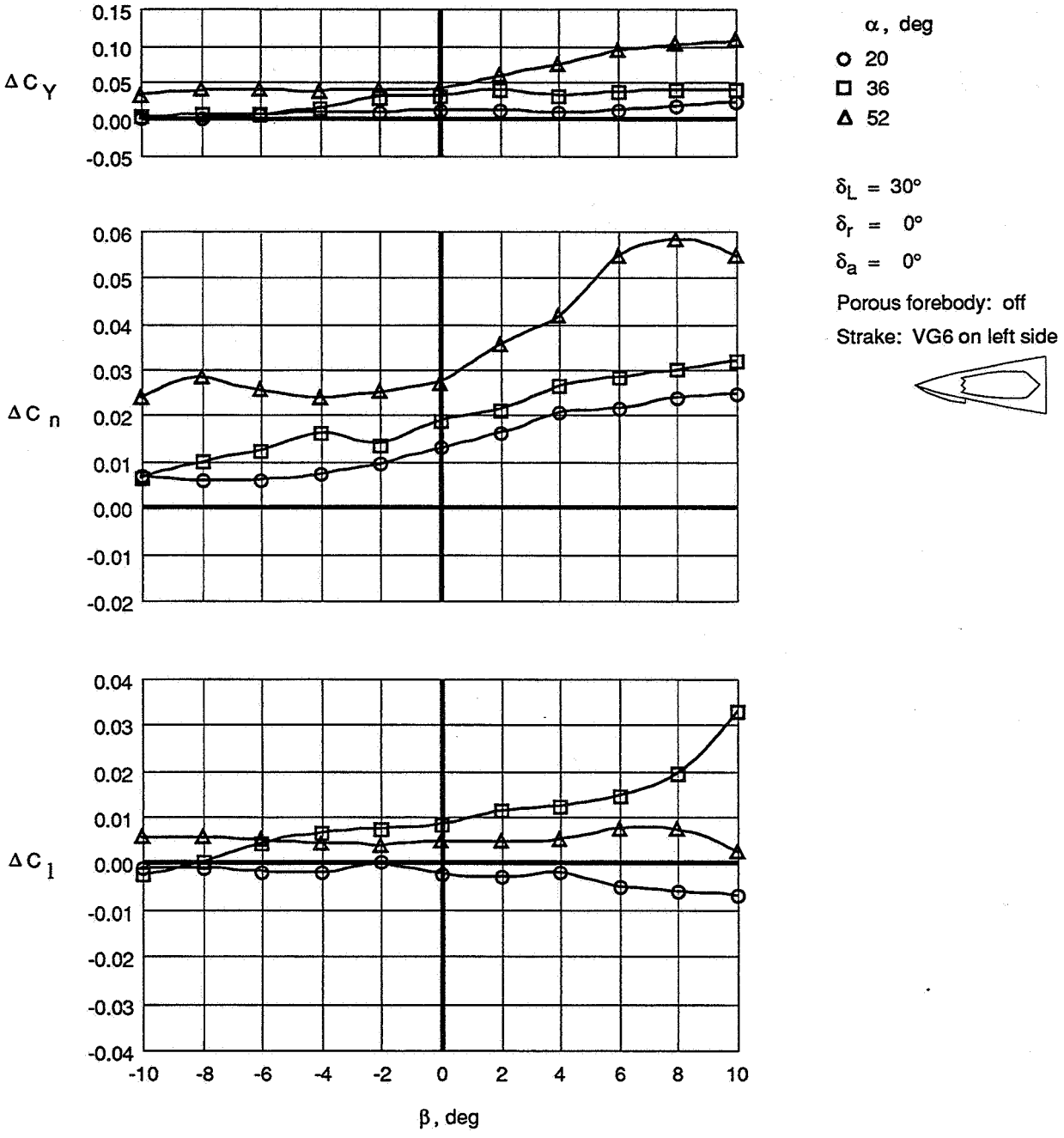

Figure 23. Effect of sideslip on effectiveness of VG6 strake.

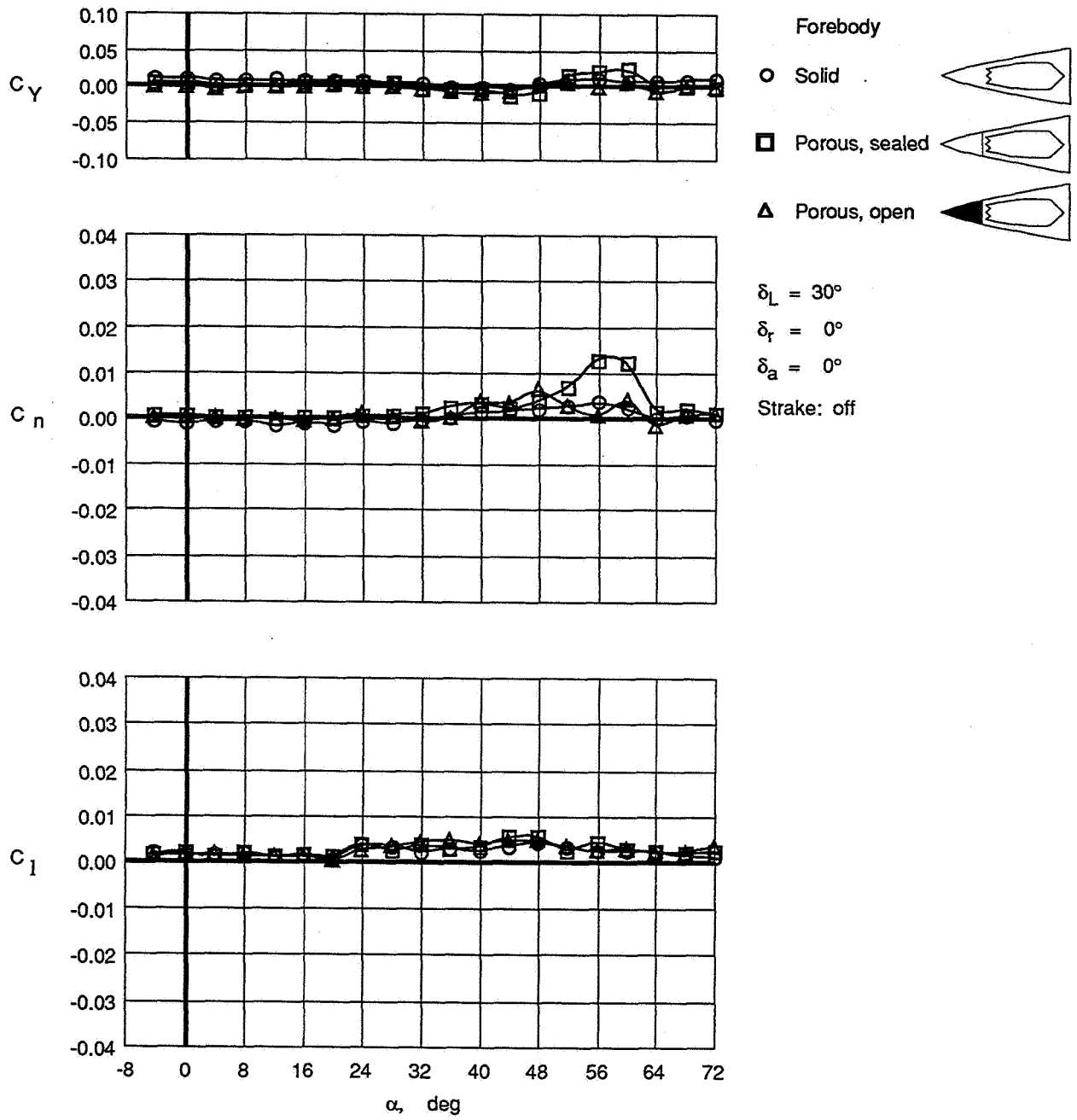

(a) Lateral-directional characteristics.

Figure 24. Effect of addition of porous forebody when sealed or completely open.

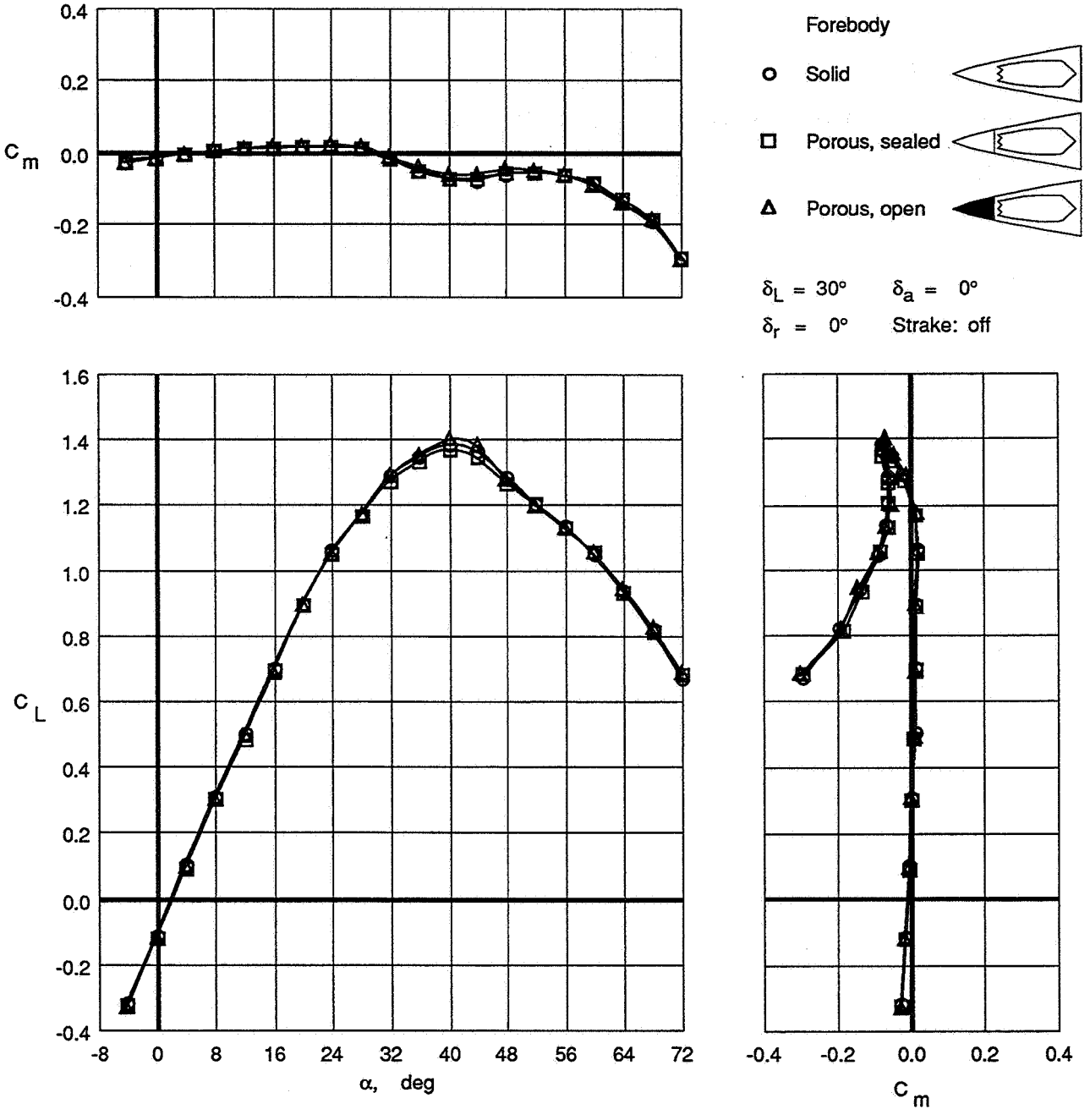

(b) Longitudinal characteristics.

Figure 24. Concluded.

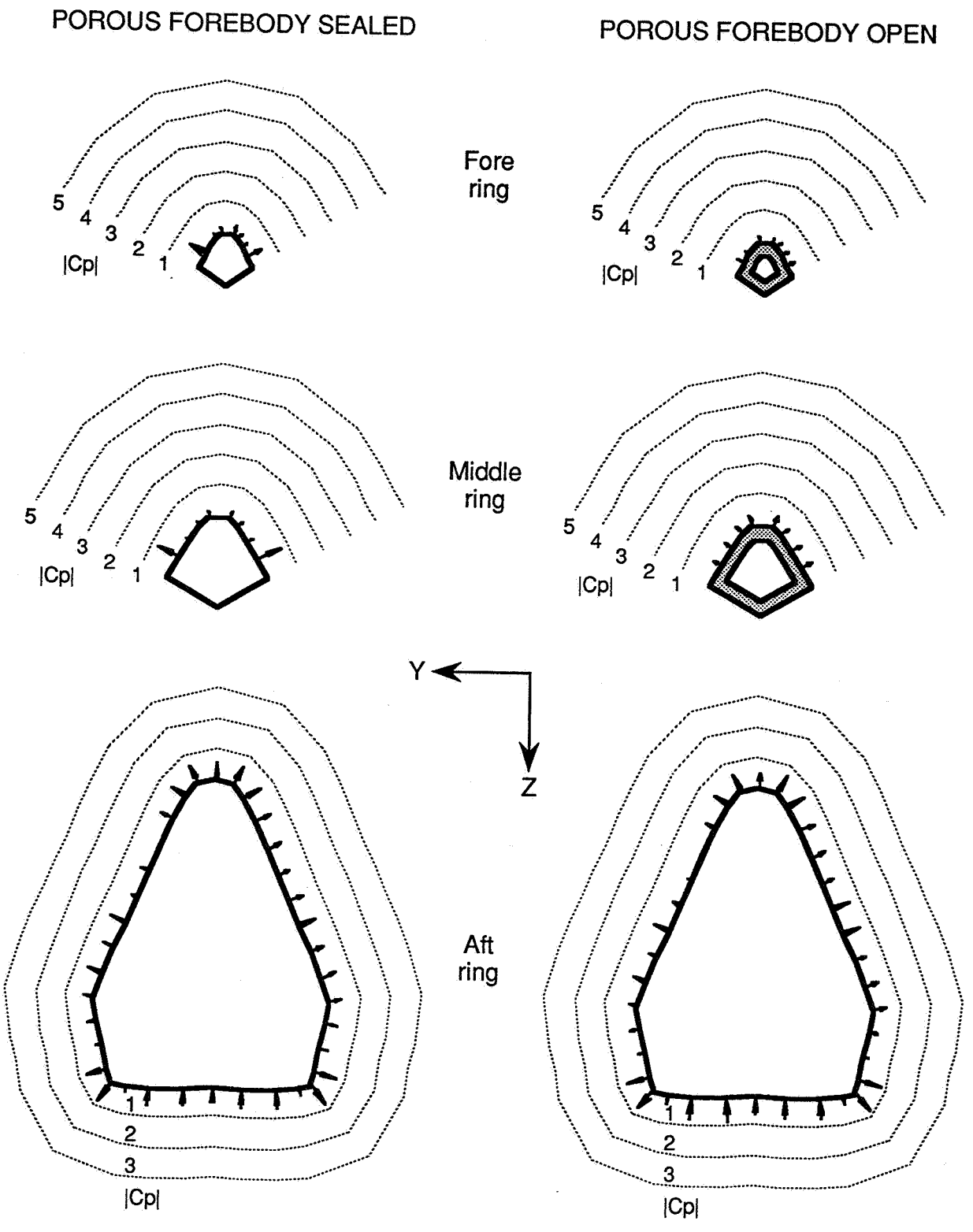

(a) α=24°, β=0°.

Figure 25. Comparison of pressure data for configurations with porous forebody sealed and completely open. Shaded areas indicate porous regions.

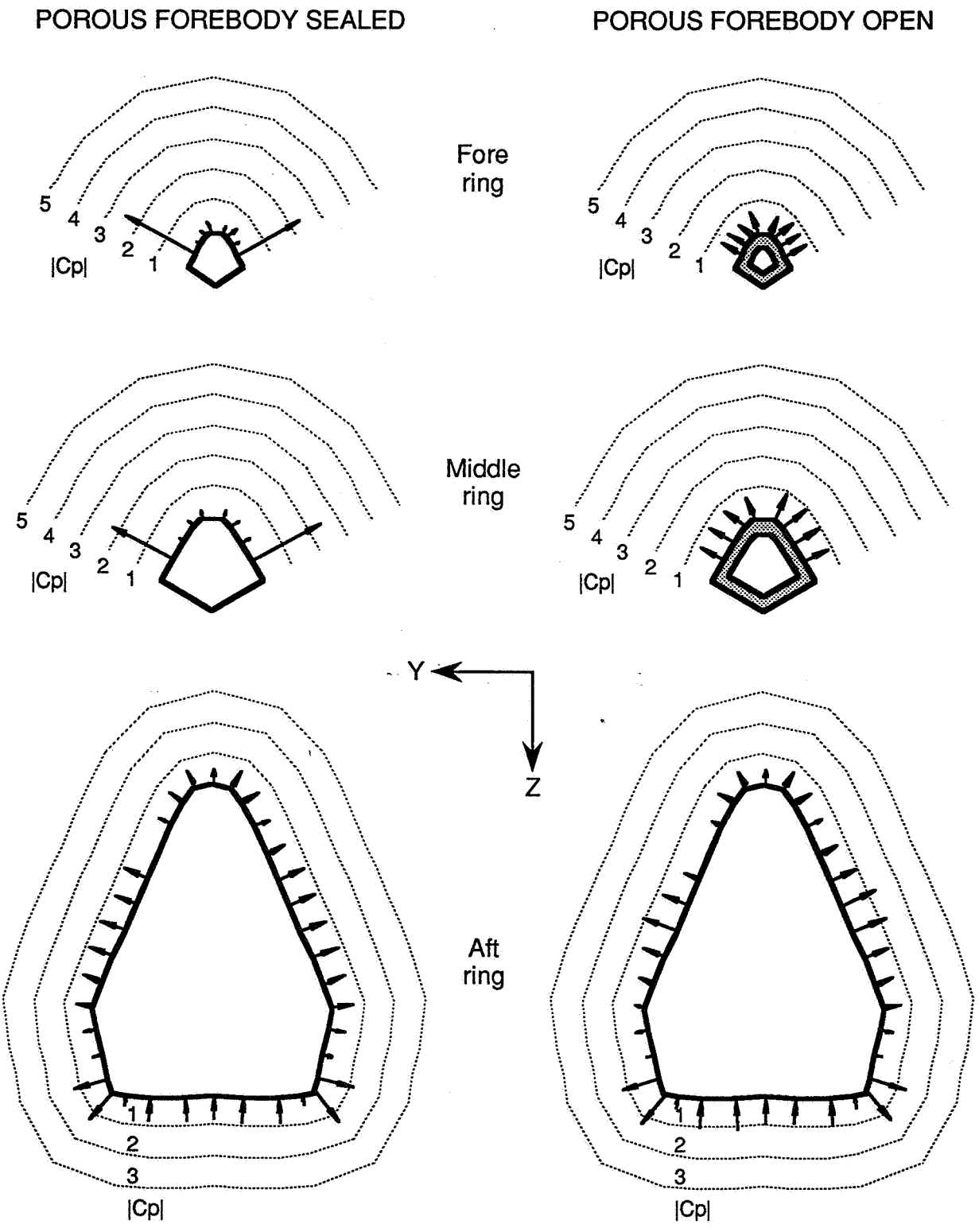

(b) α=36°, β=0°.

Figure 25. Continued.

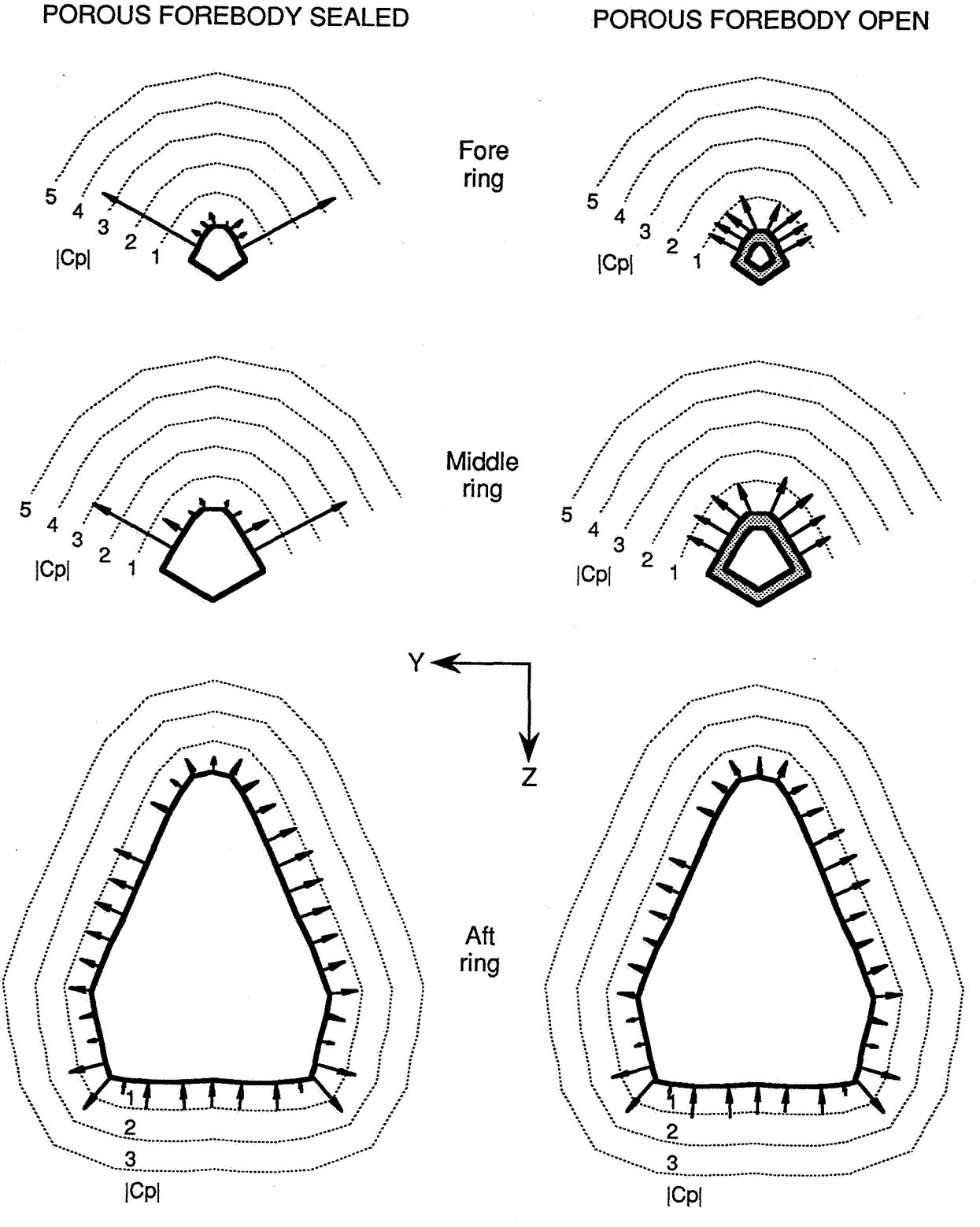

(c) α=44°, β=0°.

Figure 25. Continued.

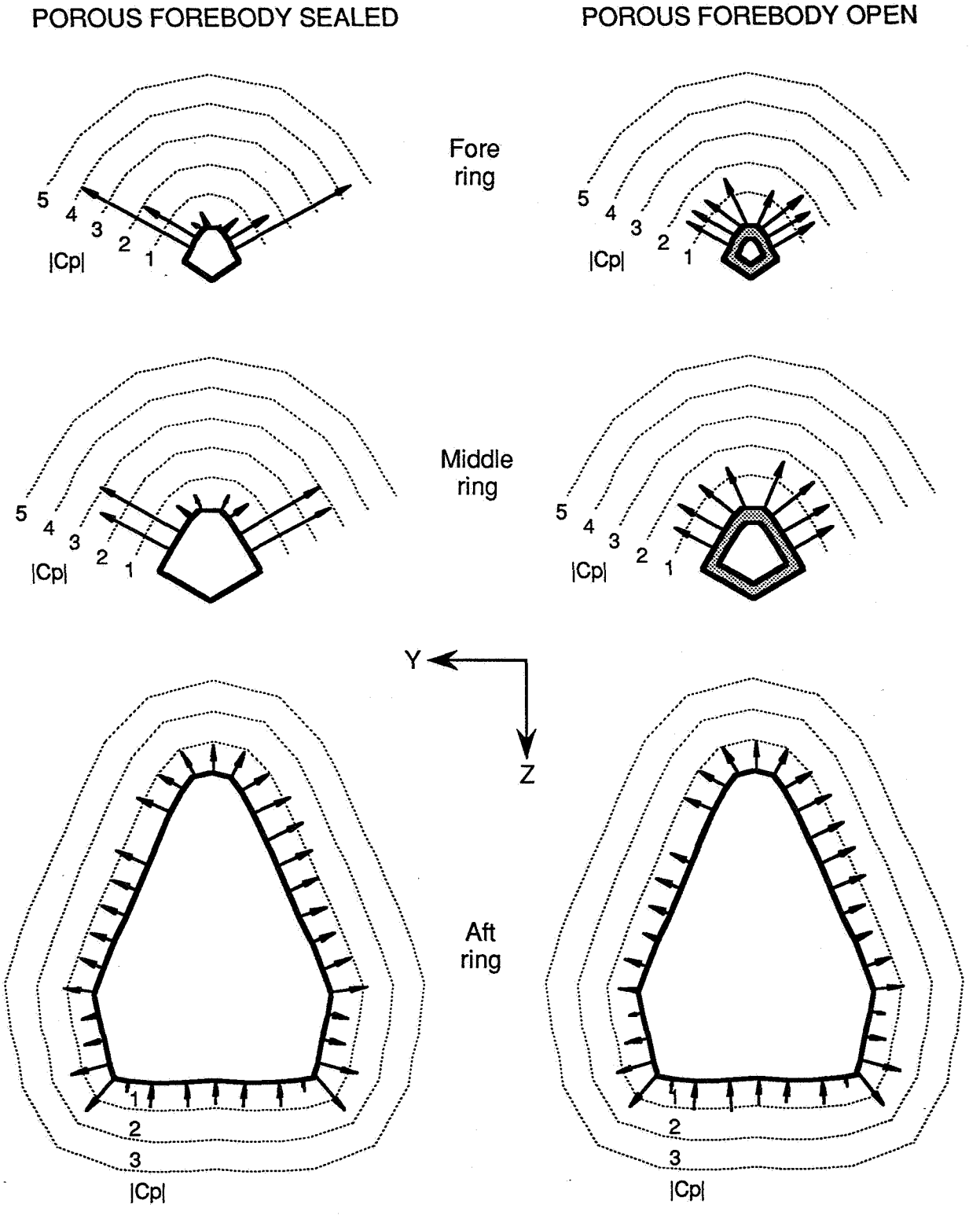

(d) α=52°, β=0°.

Figure 25. Continued.

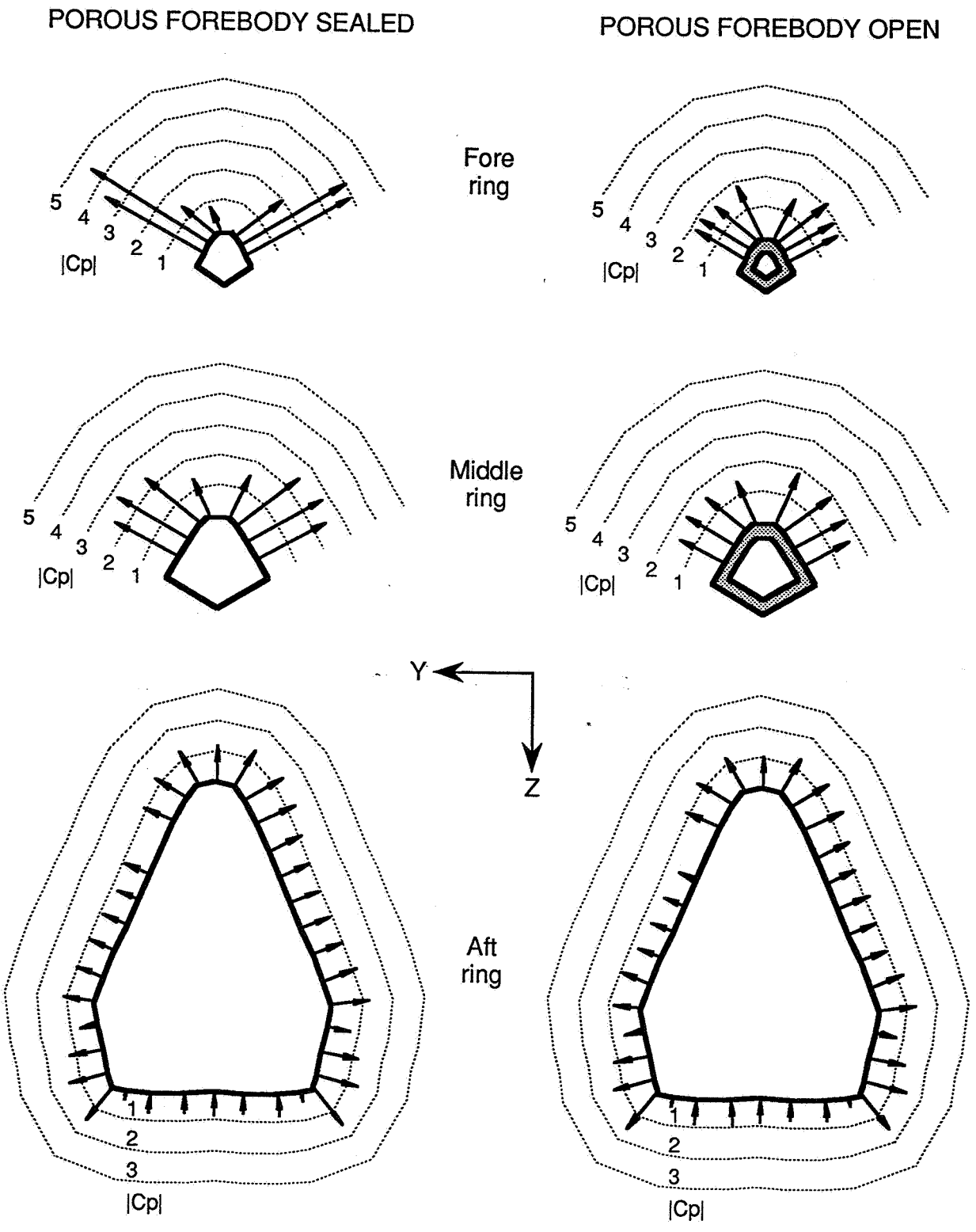

(e) α=60°, β=0°.

Figure 25. Continued.

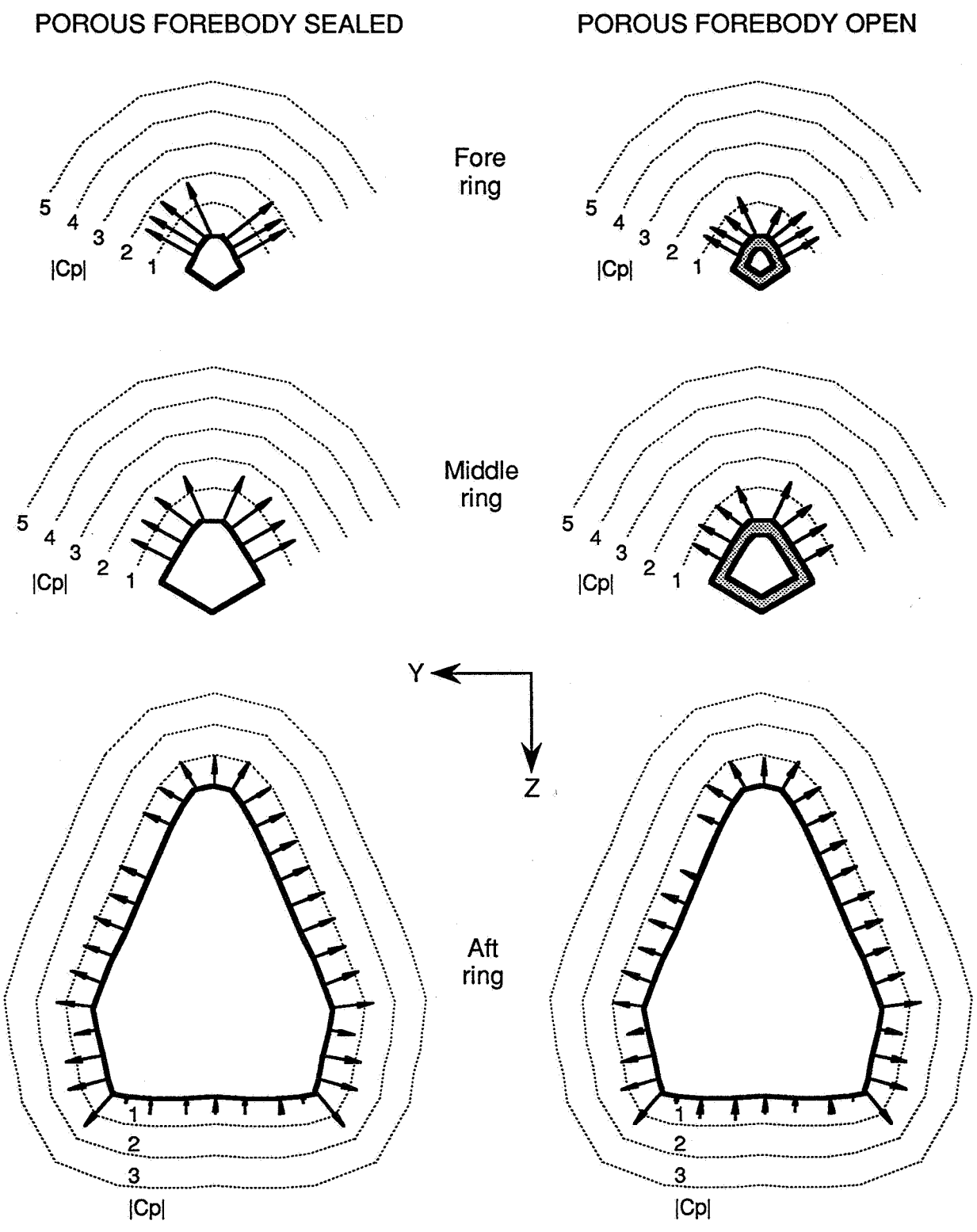

(f) α=68°, β=0°.

Figure 25. Concluded.

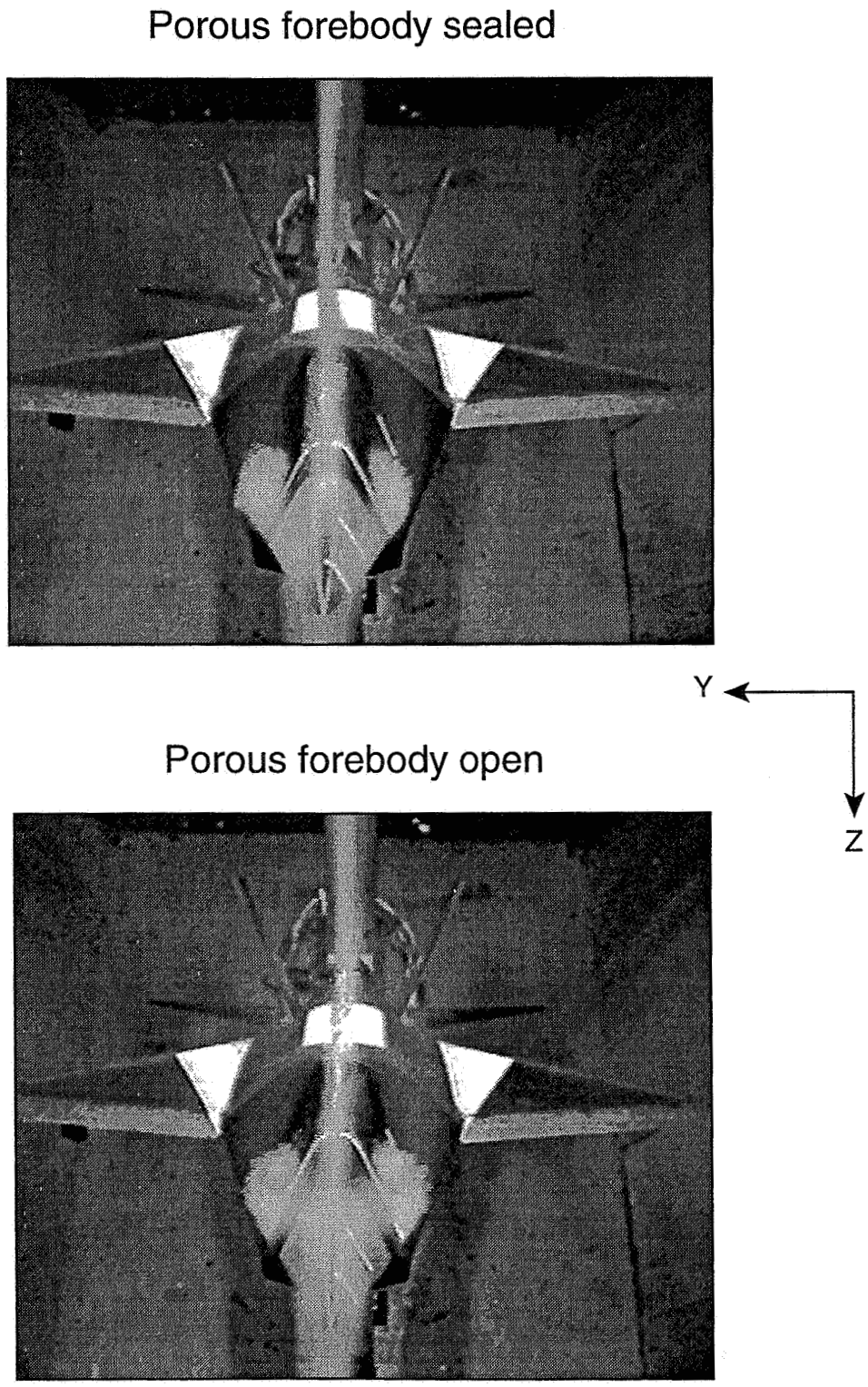

(a) α=44°, β=0°.

Figure 26. Comparison of flow visualization for configurations with porous forebody sealed and completely opened.

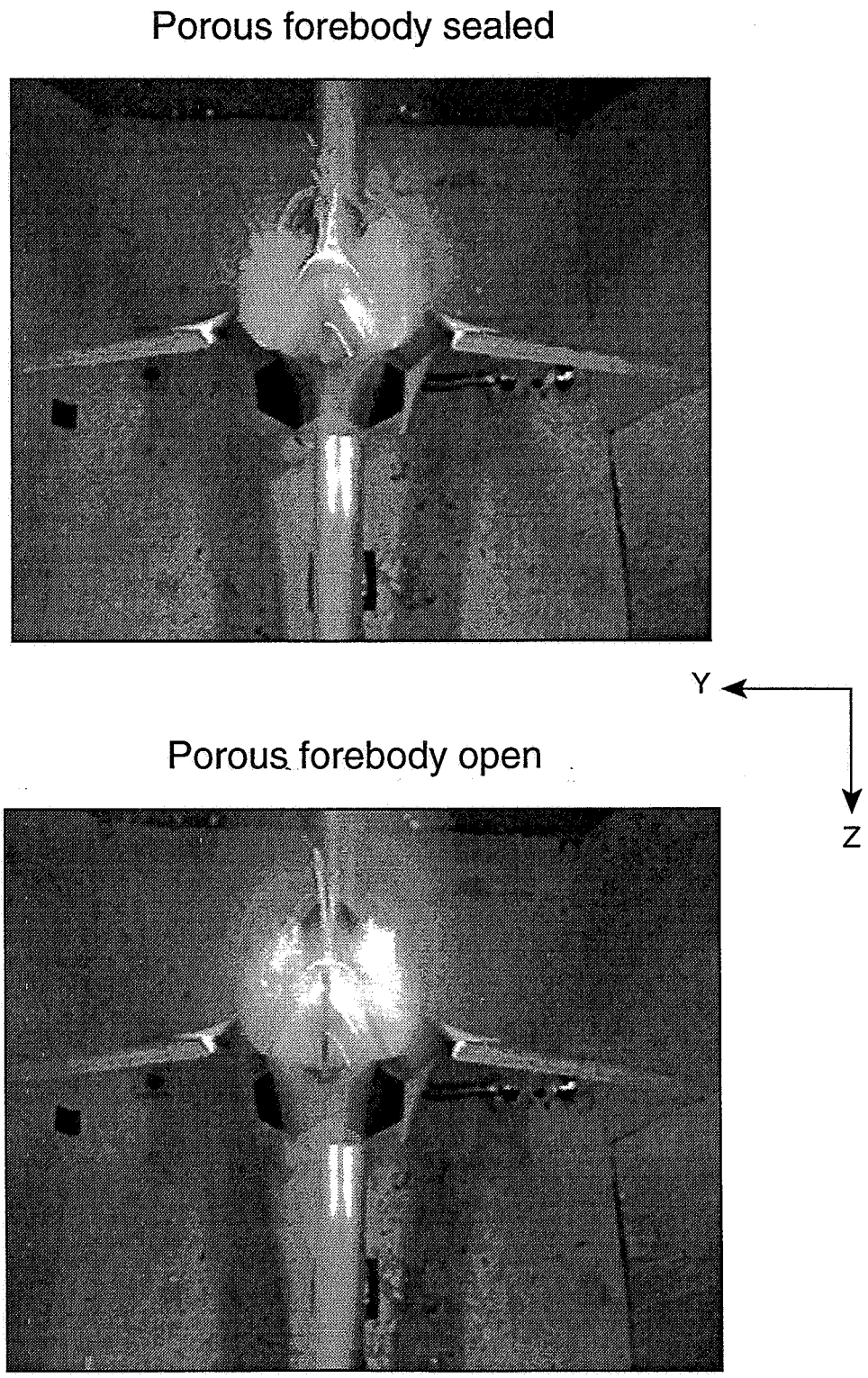

(b) α=52°, β=0°.

Figure 26. Concluded.

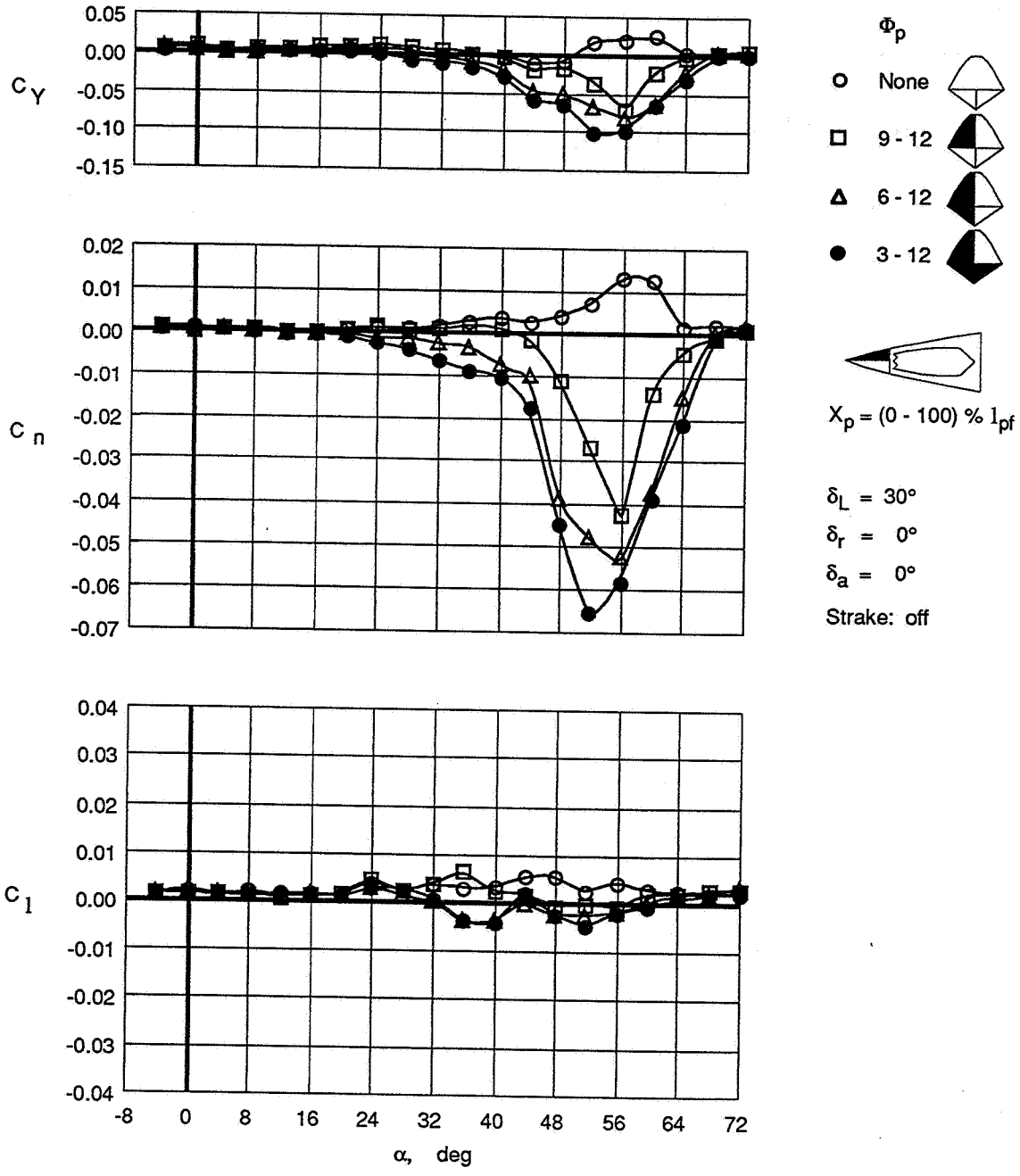

(a) Lateral-directional characteristics.

Figure 27. Effect of increasing radial porosity coverage by quadrant when starting from top centerline.

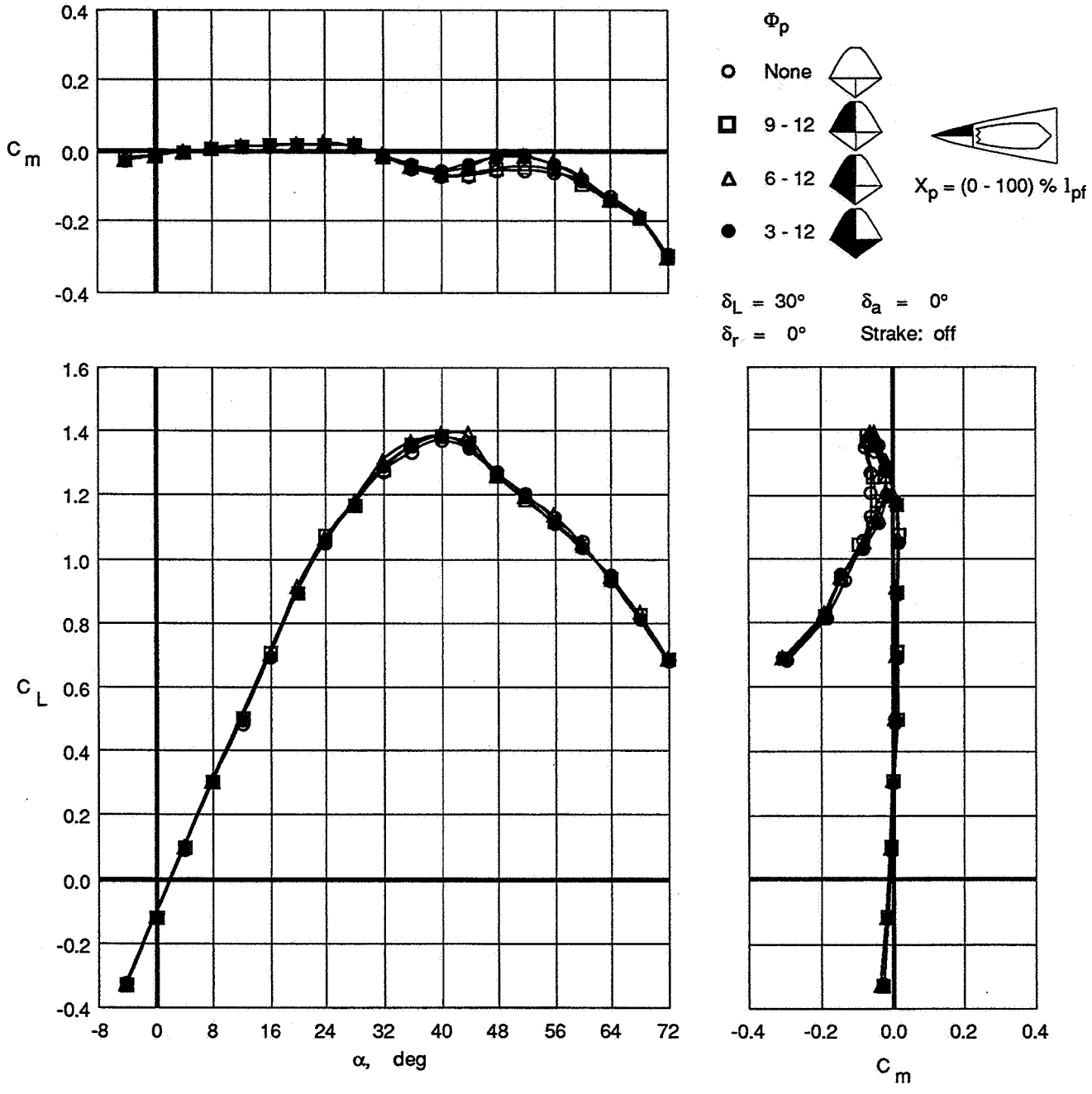

(b) Longitudinal characteristics.

Figure 27. Concluded.

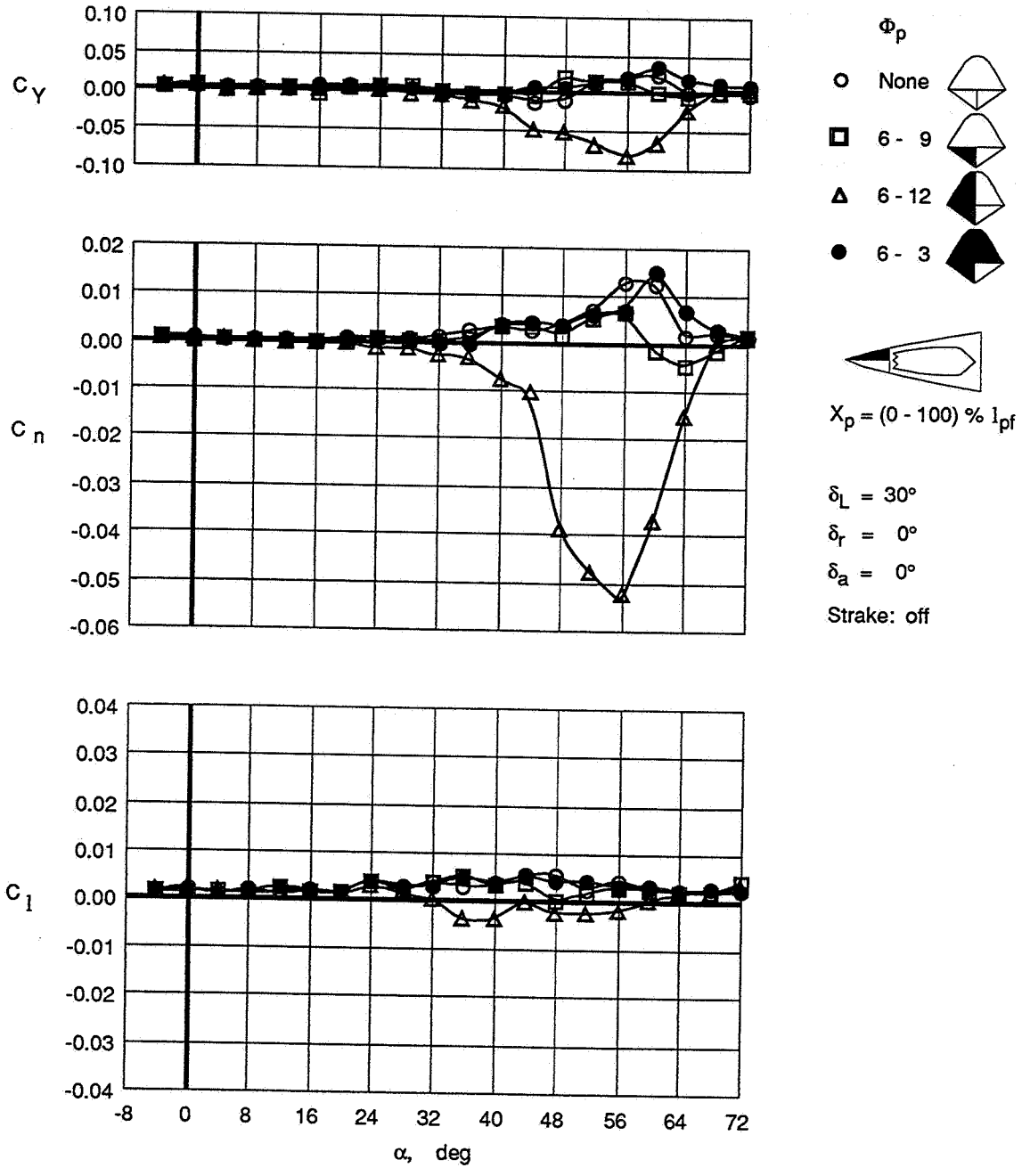

(a) Lateral-directional characteristics.

Figure 28. Effect of increasing radial porosity coverage by quadrant when starting from bottom centerline.

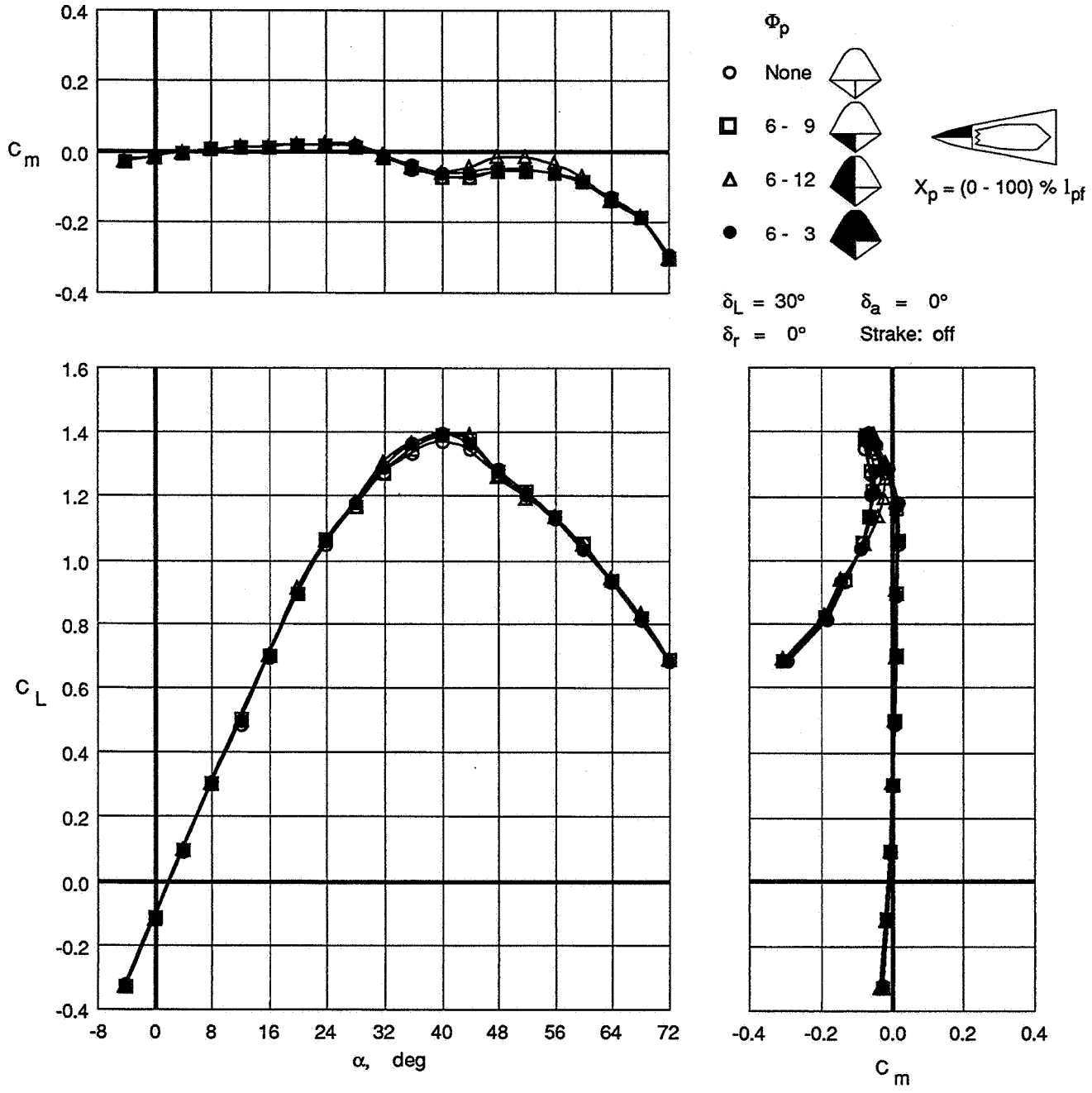

(b) Longitudinal characteristics.

Figure 28. Concluded.

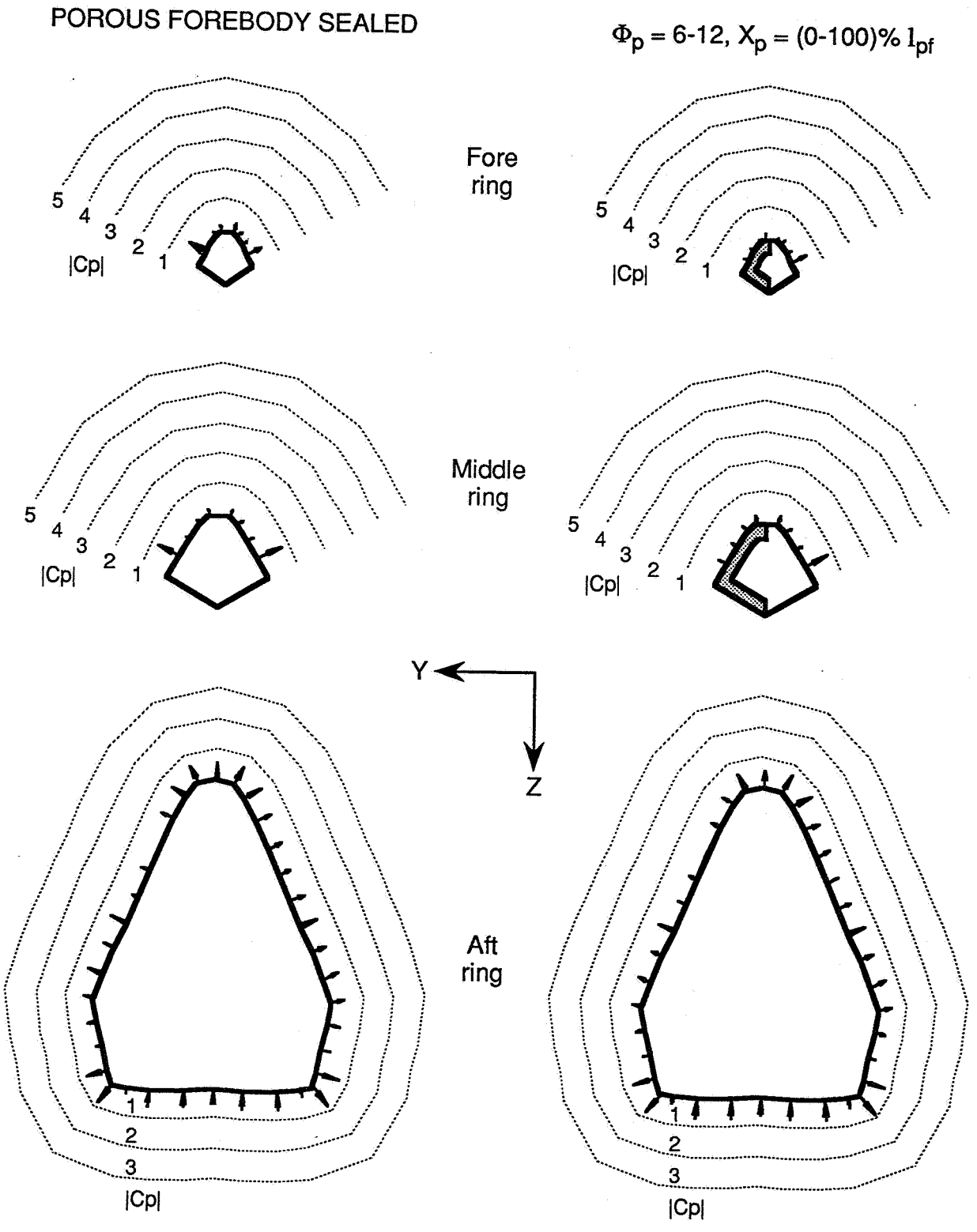

(a) α=24°, β=0°.

Figure 29. Comparison of pressure data for sealed forebody and Φ_P=6-12 configuration. Shaded areas indicate porous regions.

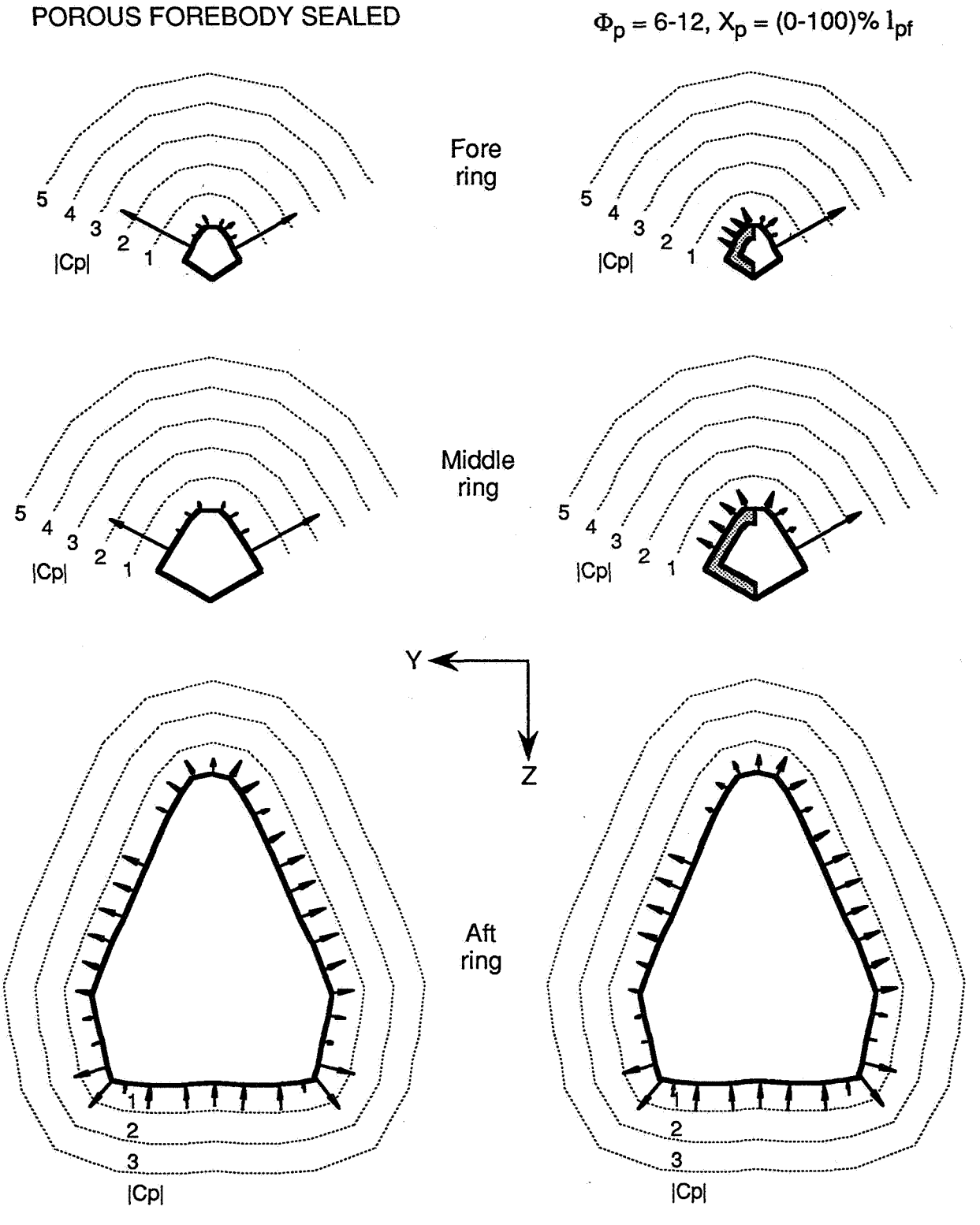

(b) α=36°, β=0°.

Figure 29. Continued.

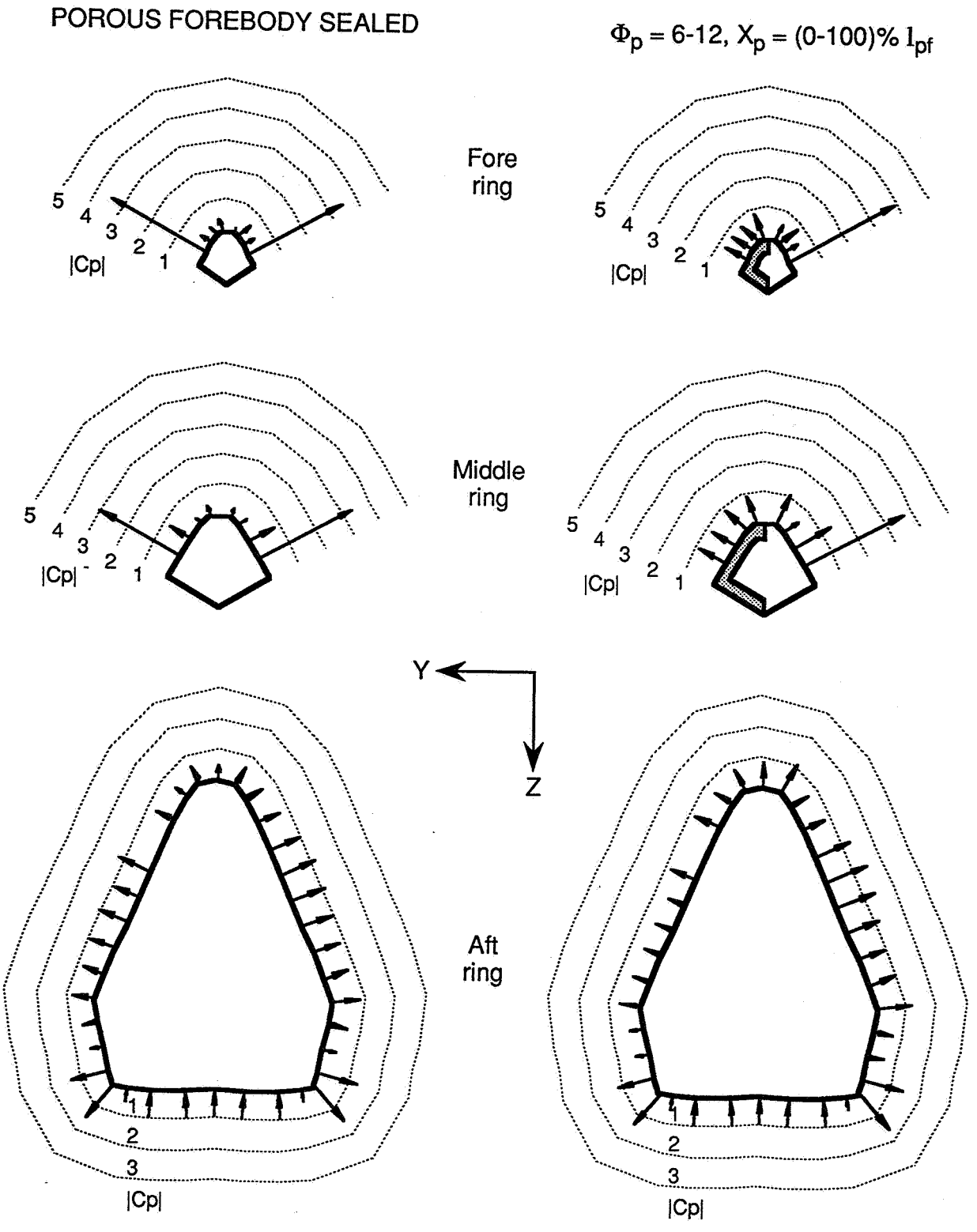

(c) α=44°, β=0°.

Figure 29. Continued.

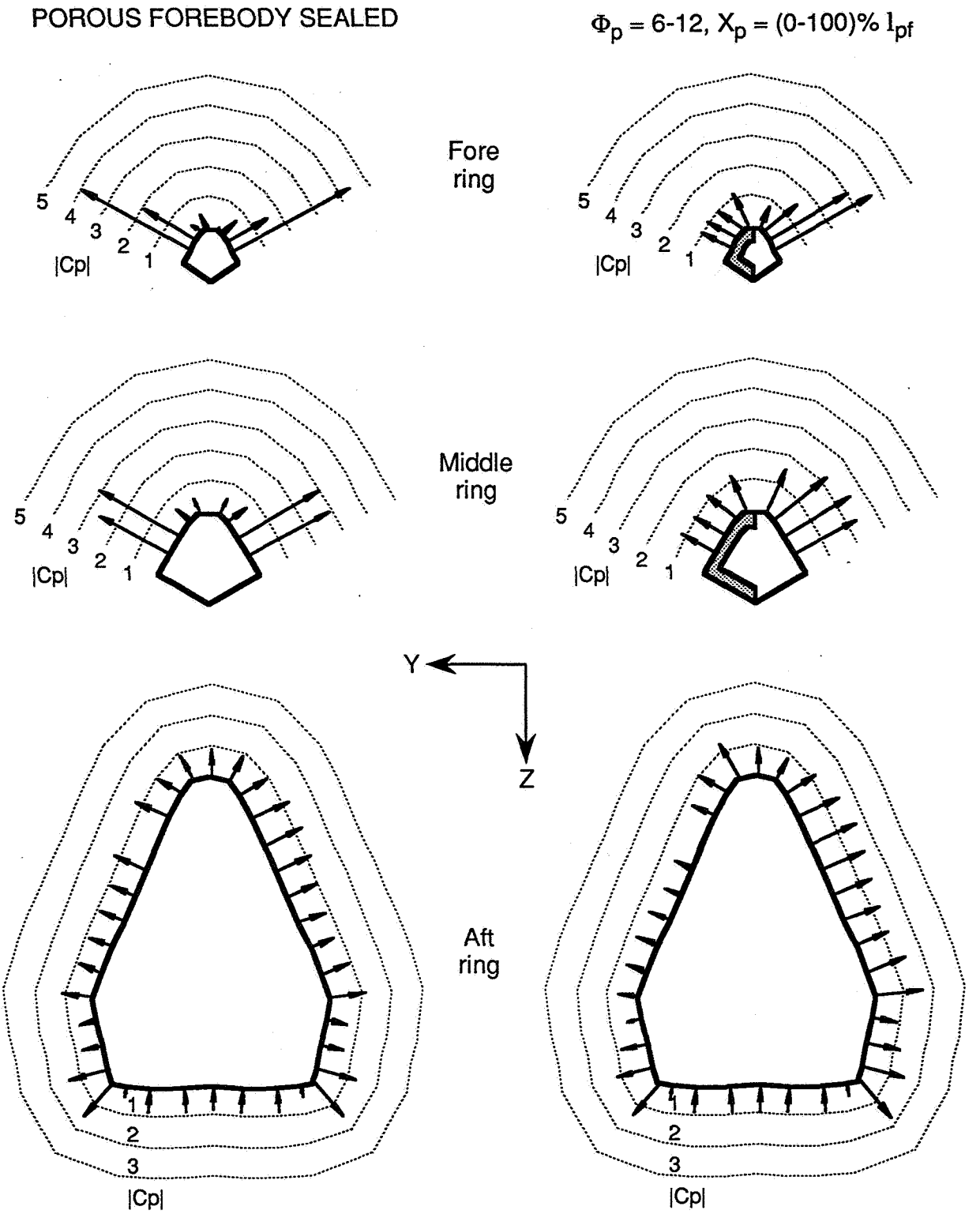

(d) α=52°, β=0°.

Figure 29. Continued.

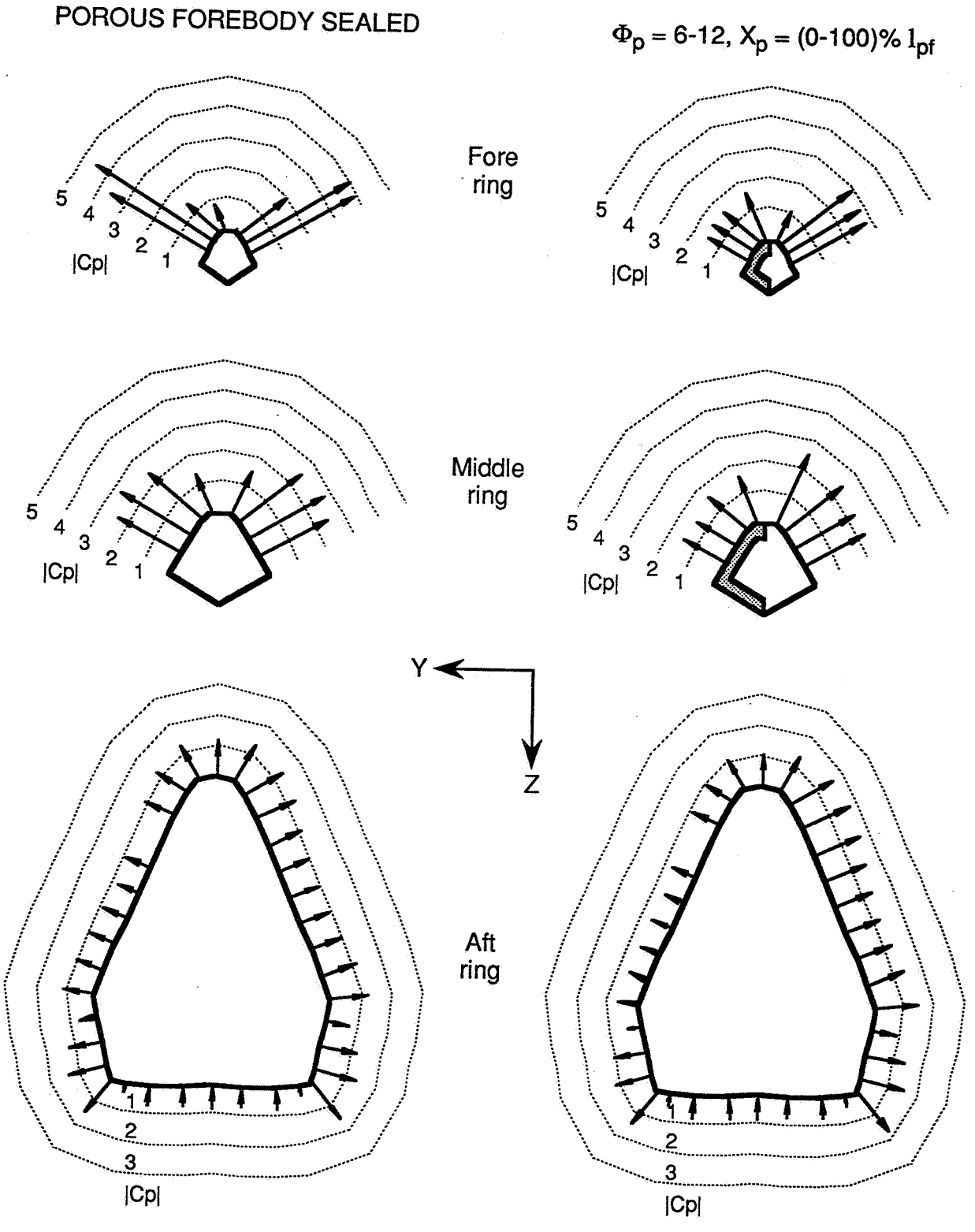

(e) α=60°, β=0°.

Figure 29. Continued.

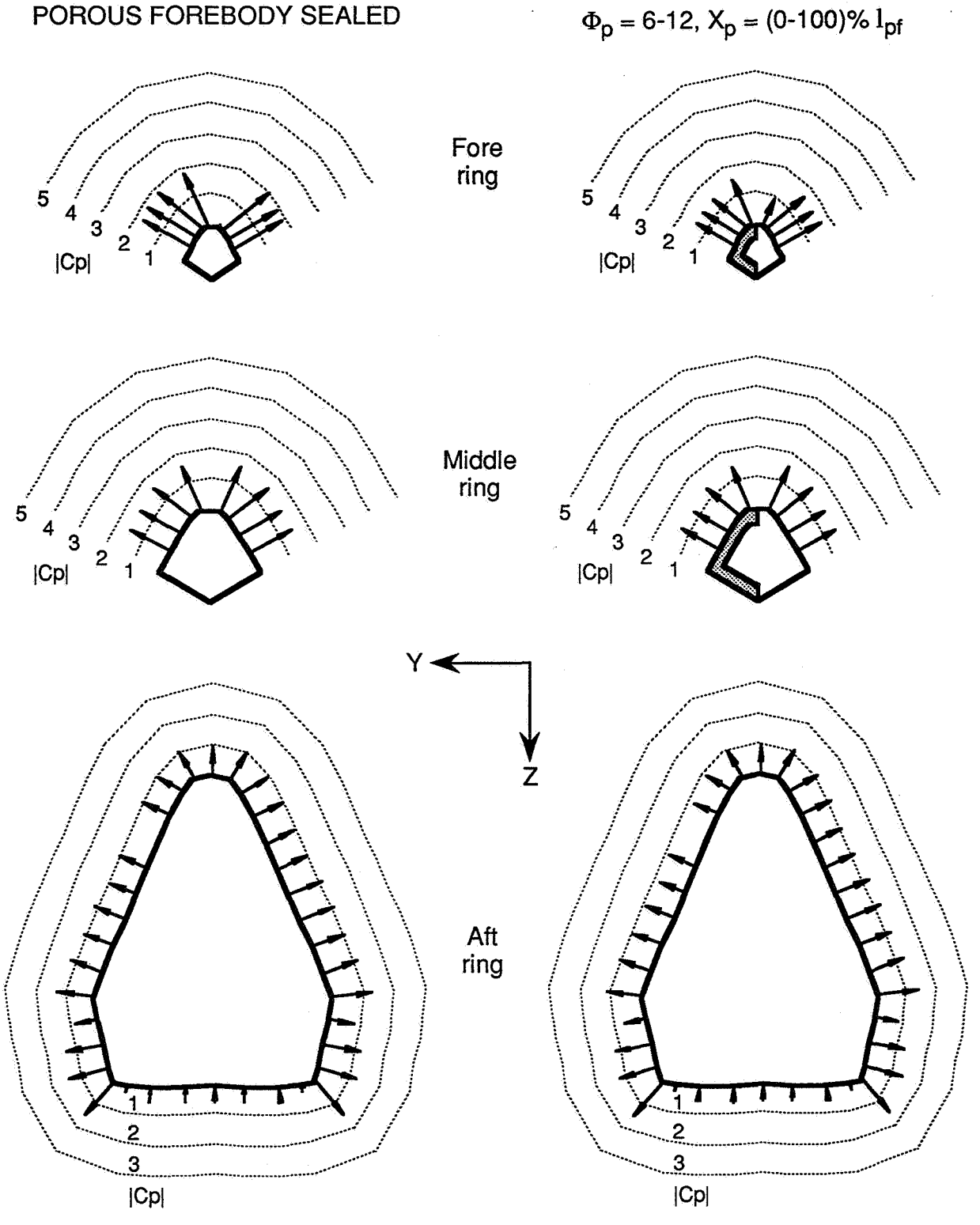

(f) α=68°, β=0°.

Figure 29. Concluded.

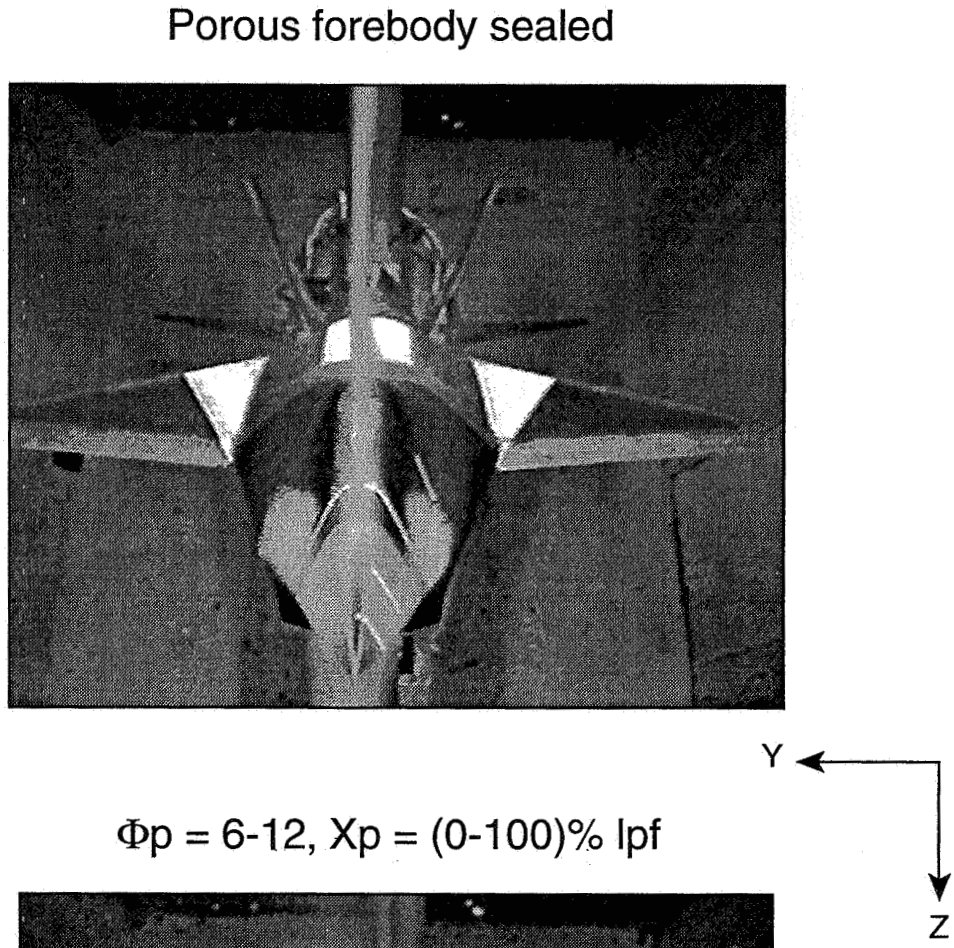

(a) α=44°, β=0°.

Figure 30. Comparison of flow visualization for sealed forebody and Φp = 6-12 configuration.

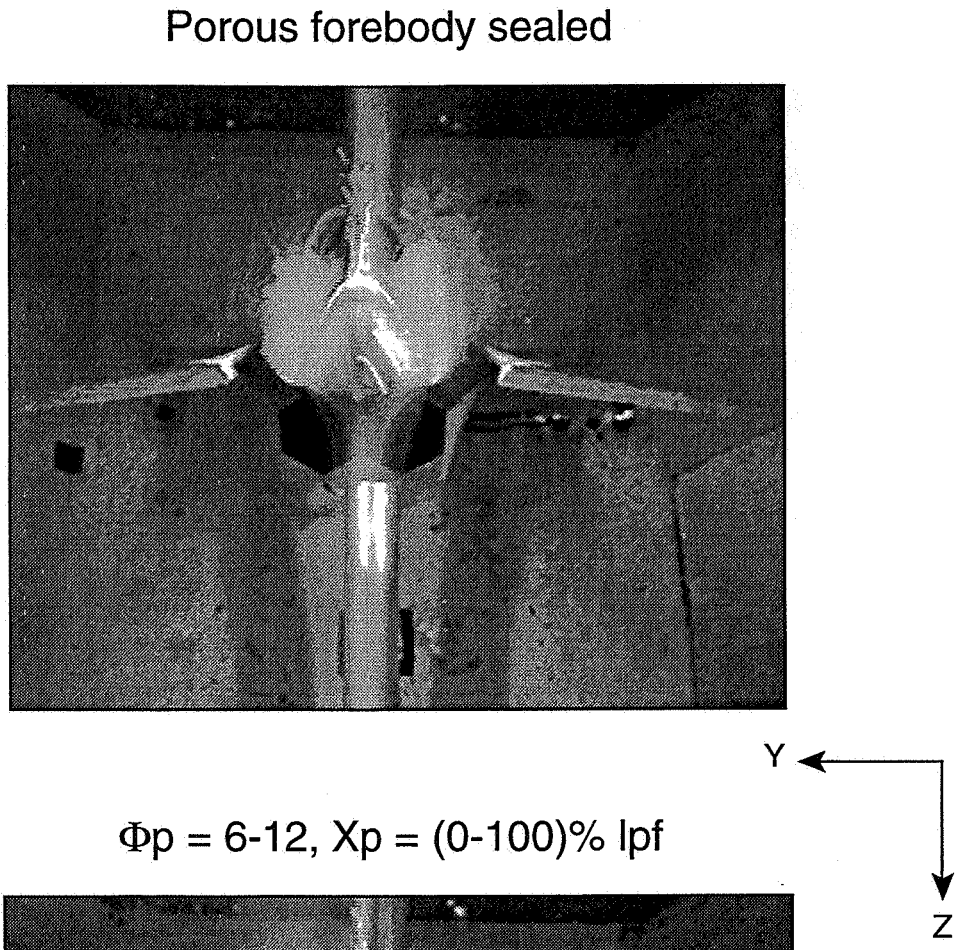

(b) α=52°, β=0°.

Figure 30. Concluded.

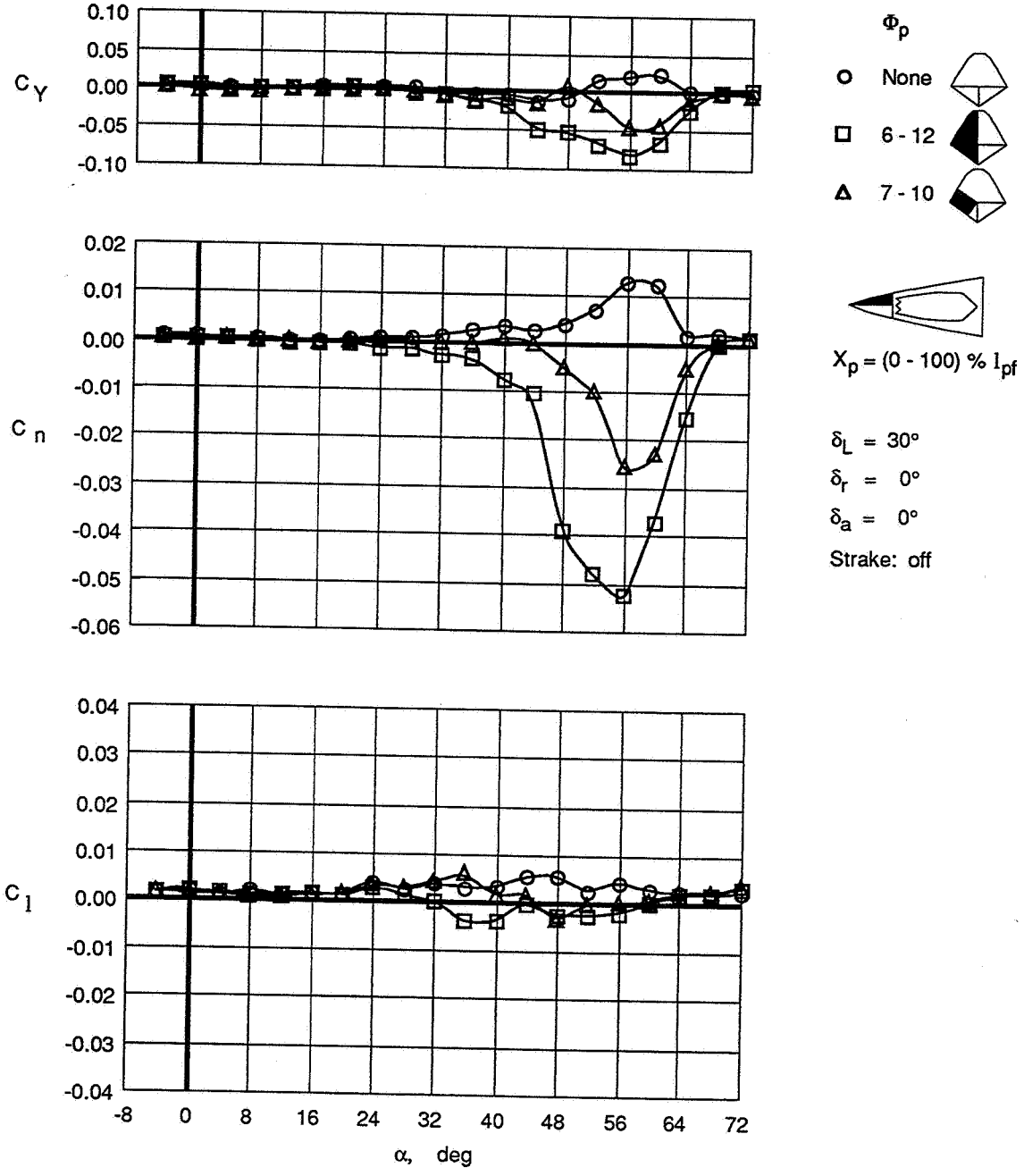

(a) Lateral-directional characteristics.

Figure 31. Effectiveness of region of forebody porosity located primarily along chine line.

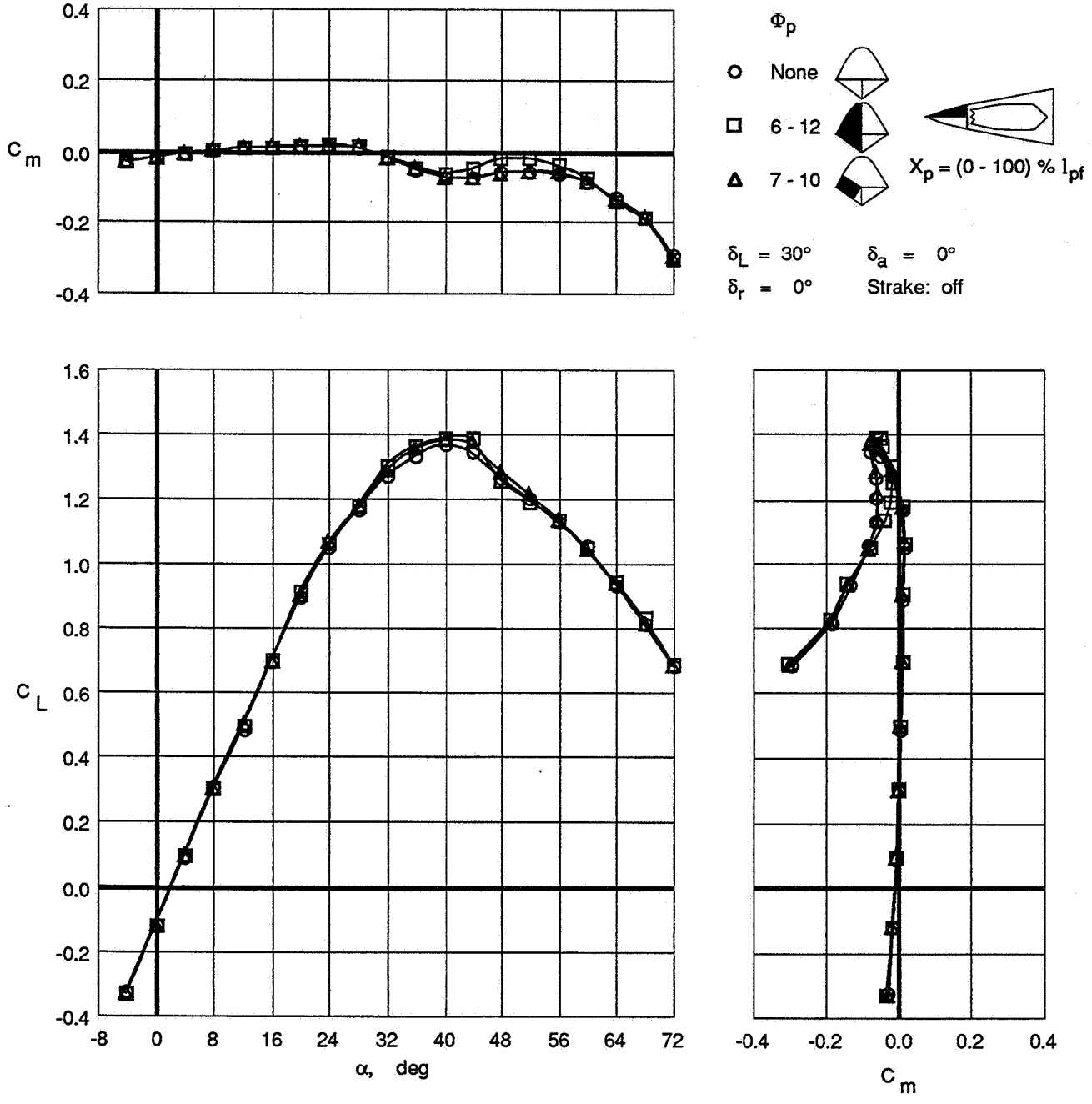

(b) Longitudinal characteristics.

Figure 31. Concluded.

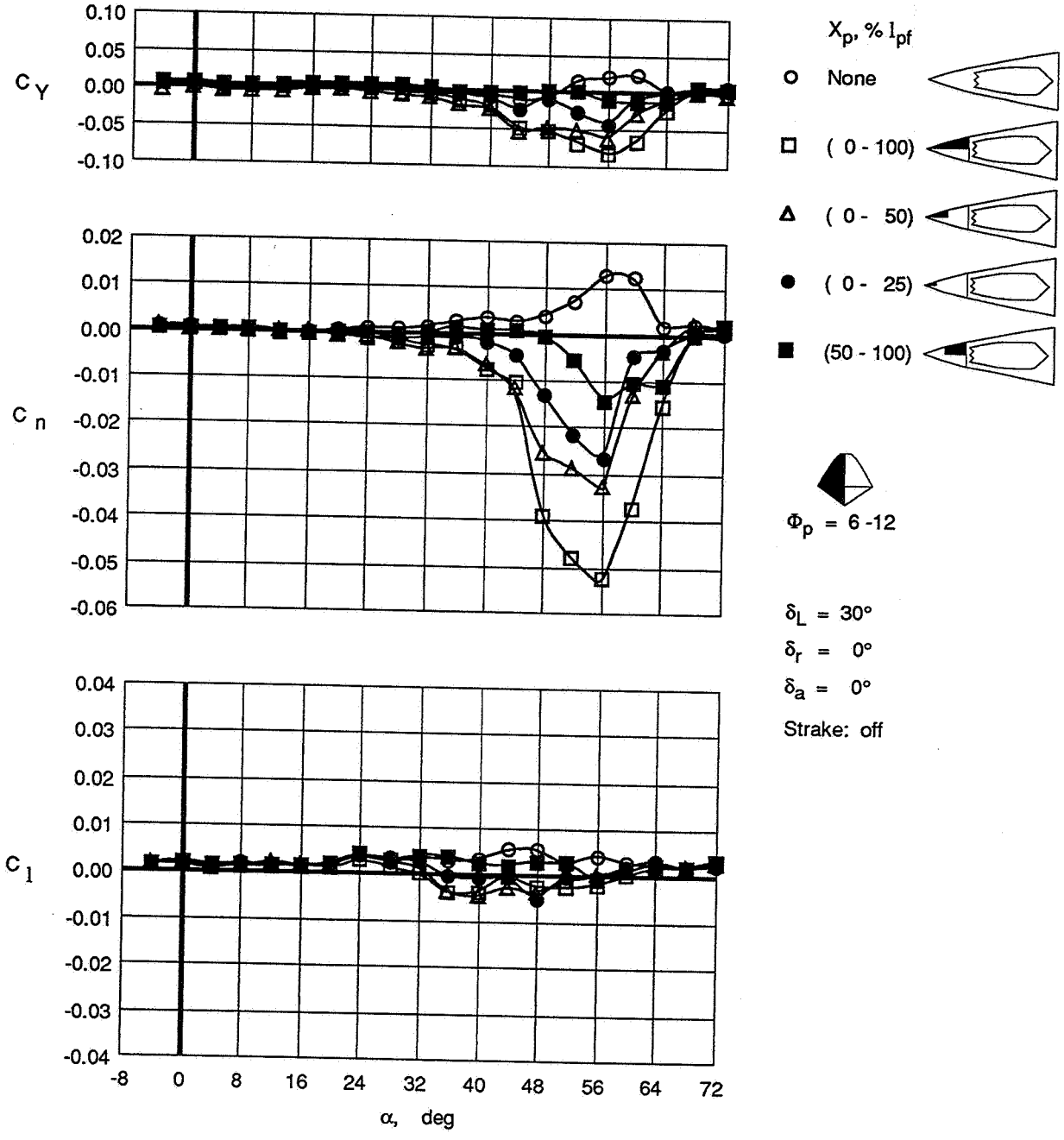

(a) Lateral-directional characteristics.

Figure 32. Effect of varying chordwise porosity coverage when Φ_p = 6-12.

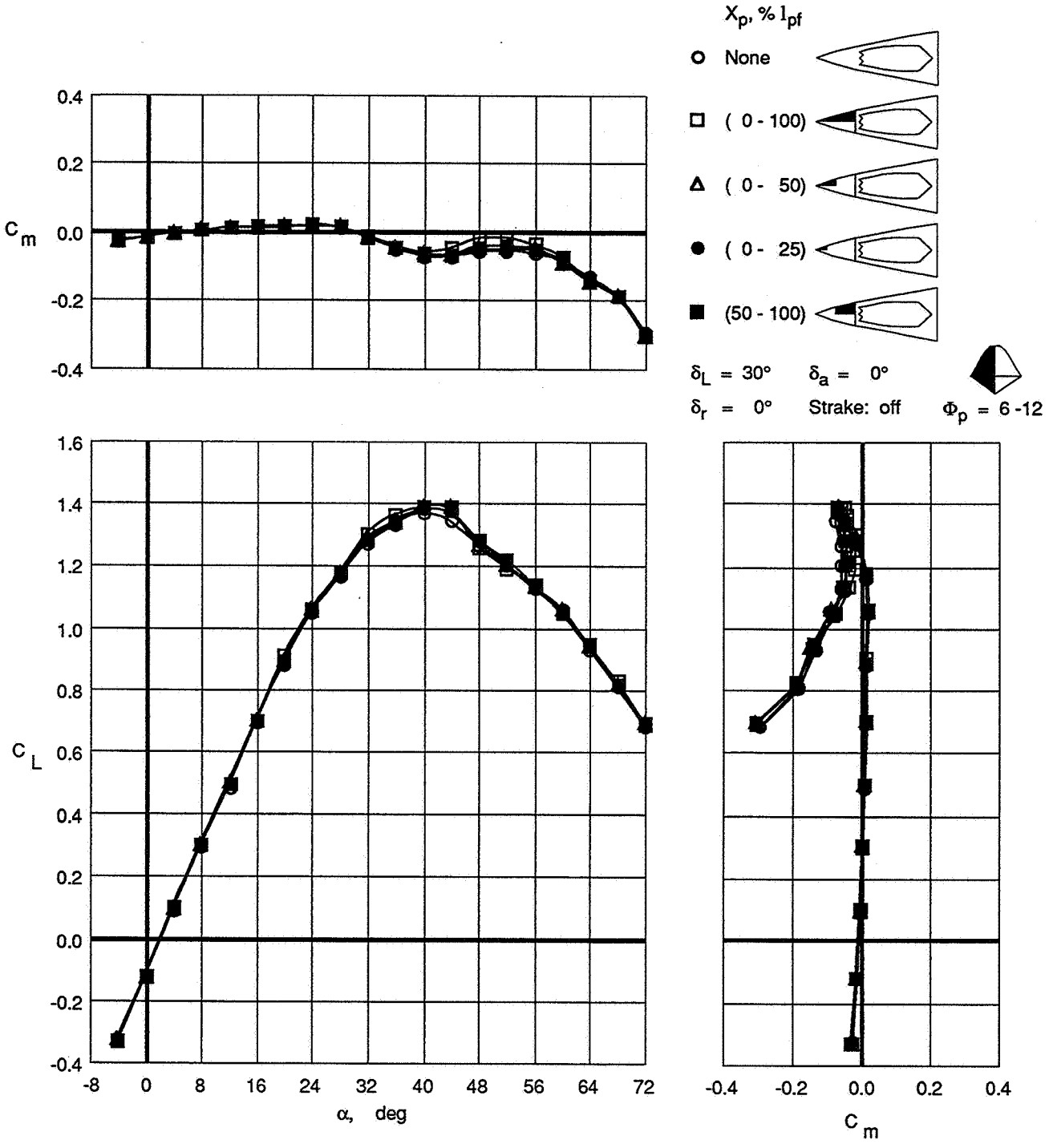

(b) Longitudinal characteristics.

Figure 32. Concluded.

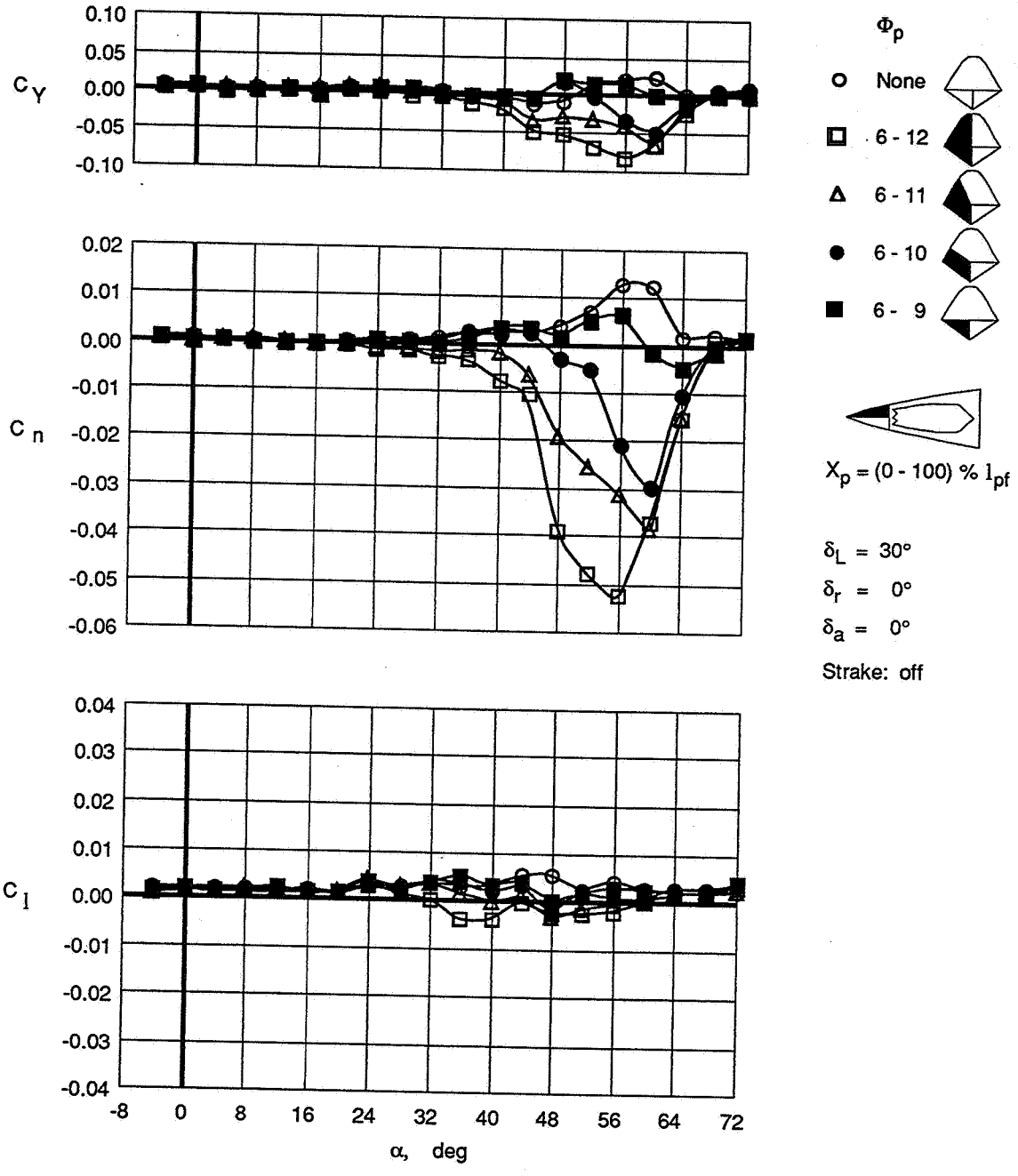

(a) Lateral-directional characteristics.

Figure 33. Modulation of yawing moment when starting with Φ_p=6-12 configuration by decreasing radial porosity coverage on upper surfaces.

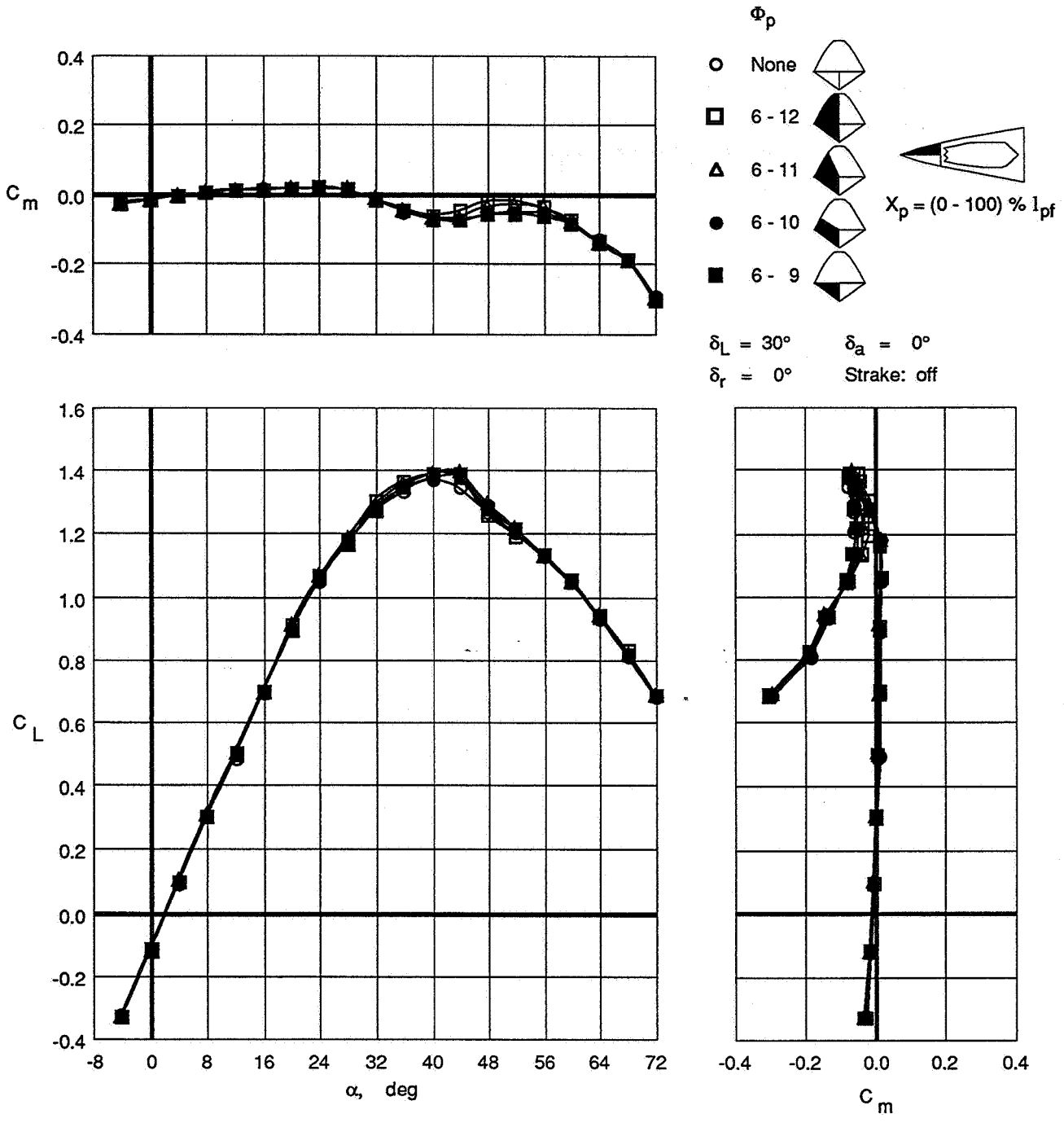

(b) Longitudinal characteristics.

Figure 33. Concluded.

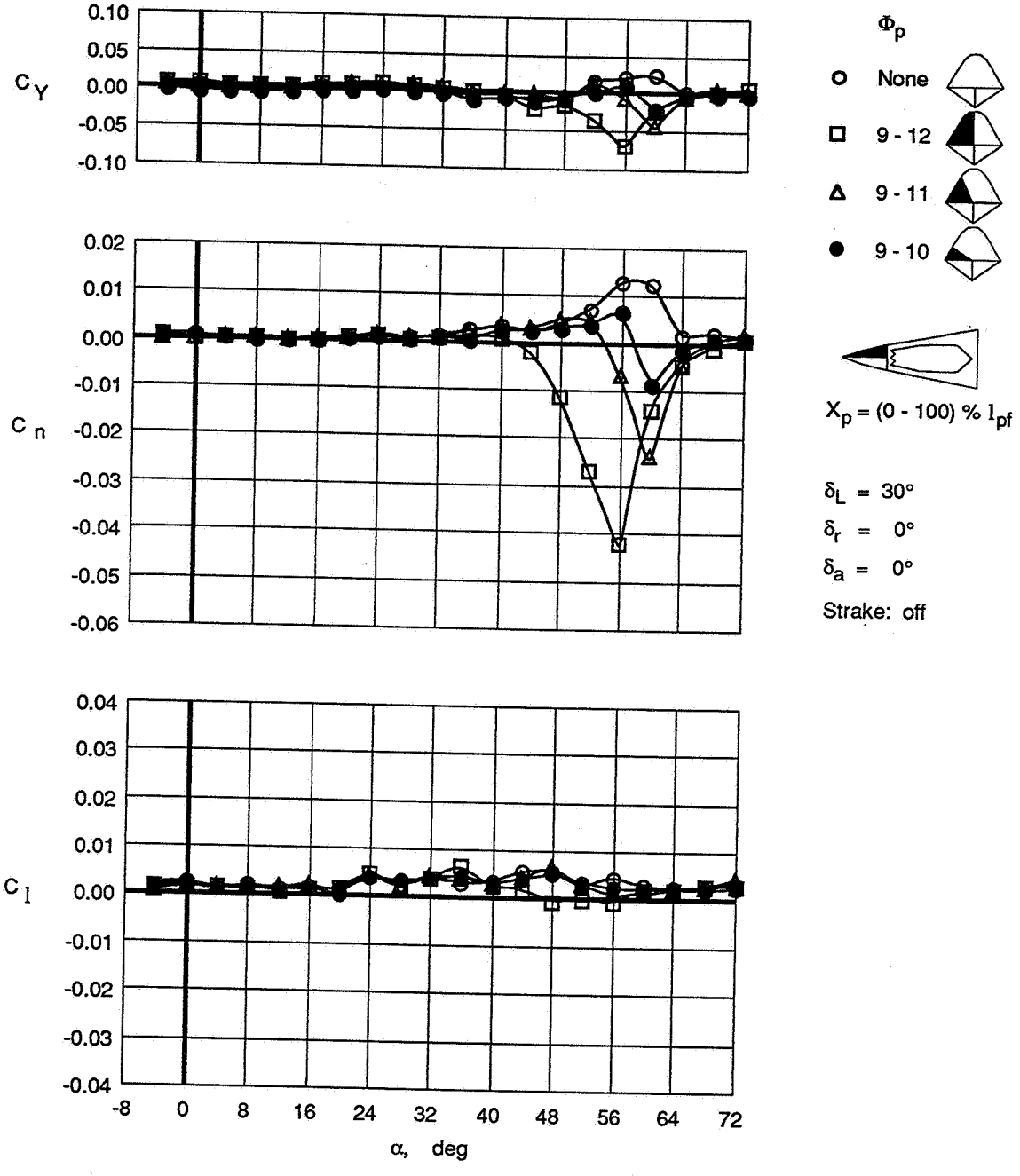

(a) Lateral-directional characteristics.

Figure 34. Modulation of yawing moment when starting with Φ_p=9-12 configuration by decreasing radial porosity coverage.

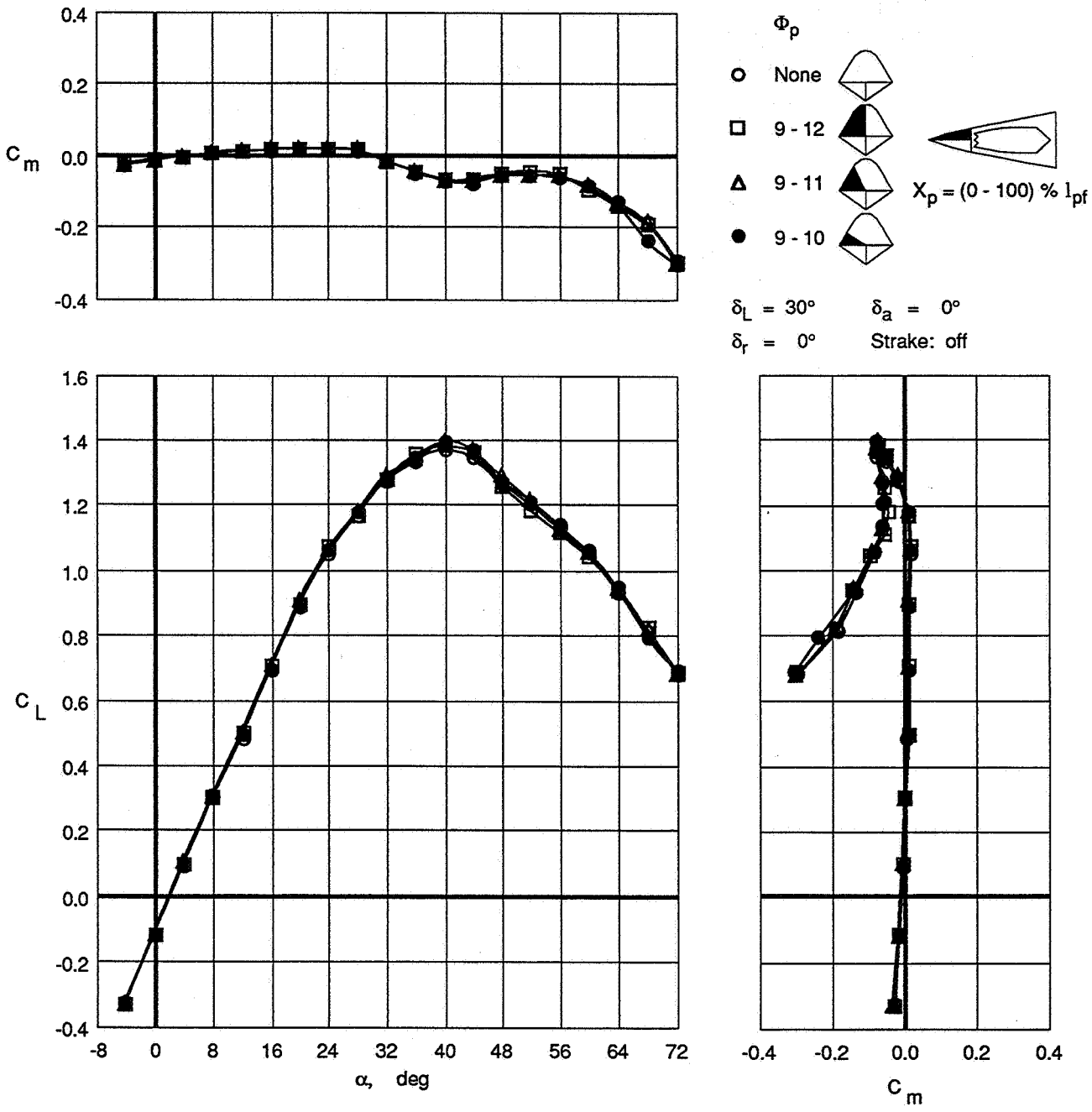

(b) Longitudinal characteristics.

Figure 34. Concluded.

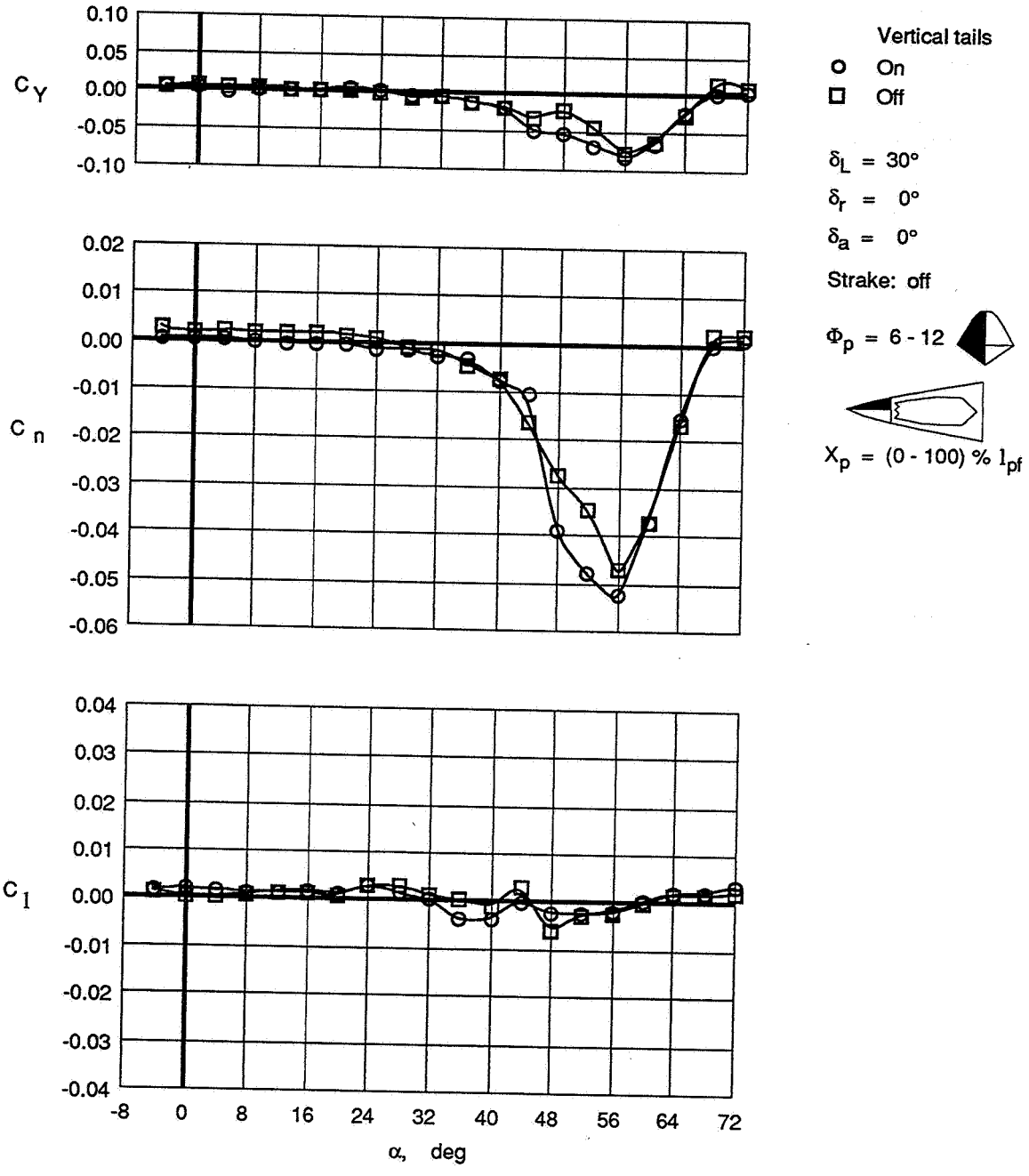

(a) Lateral-directional characteristics.

Figure 35. Effect of removing vertical tails on Φ_p=6-12 configuration.

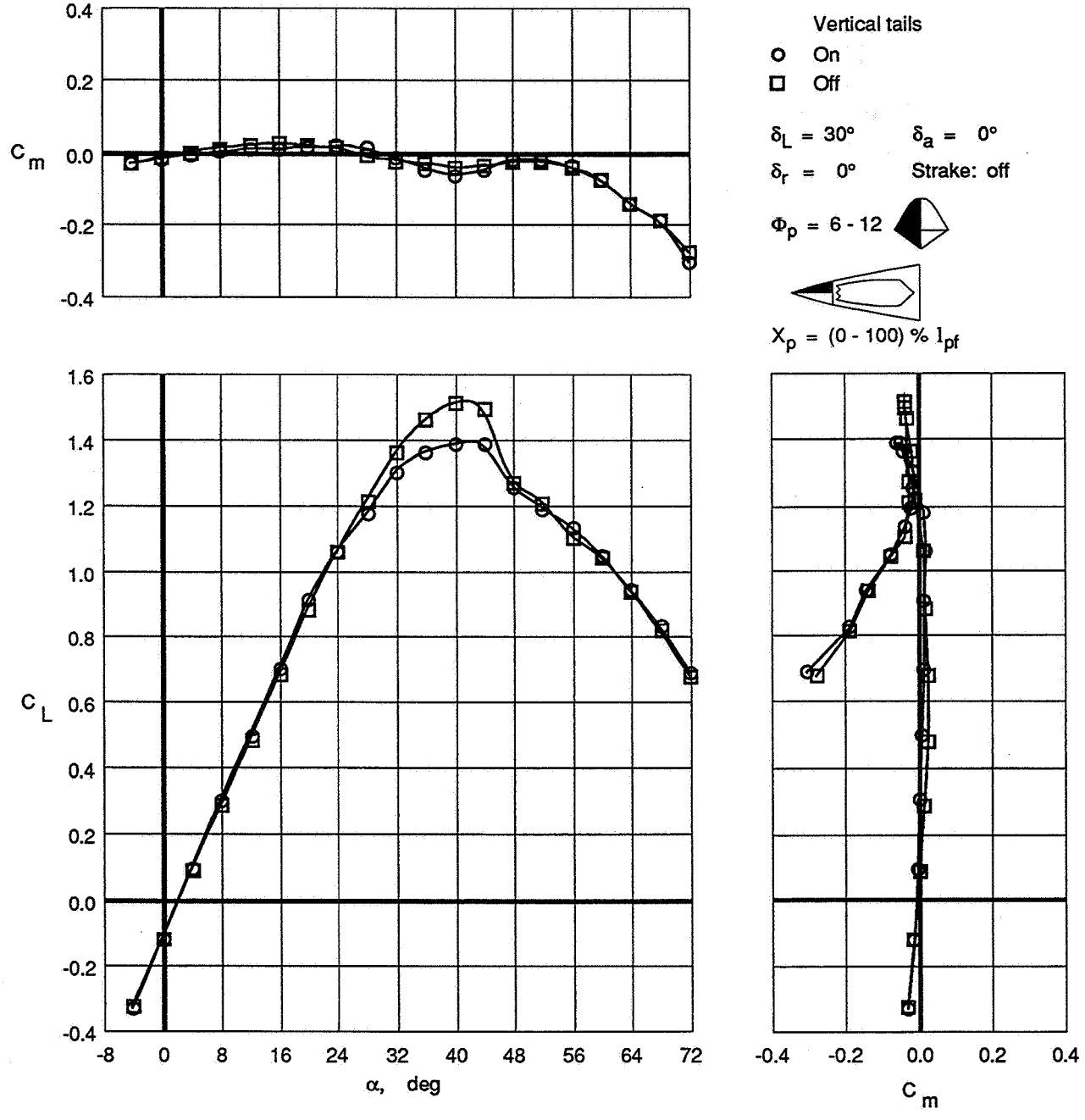

(b) Longitudinal characteristics.

Figure 35. Concluded.

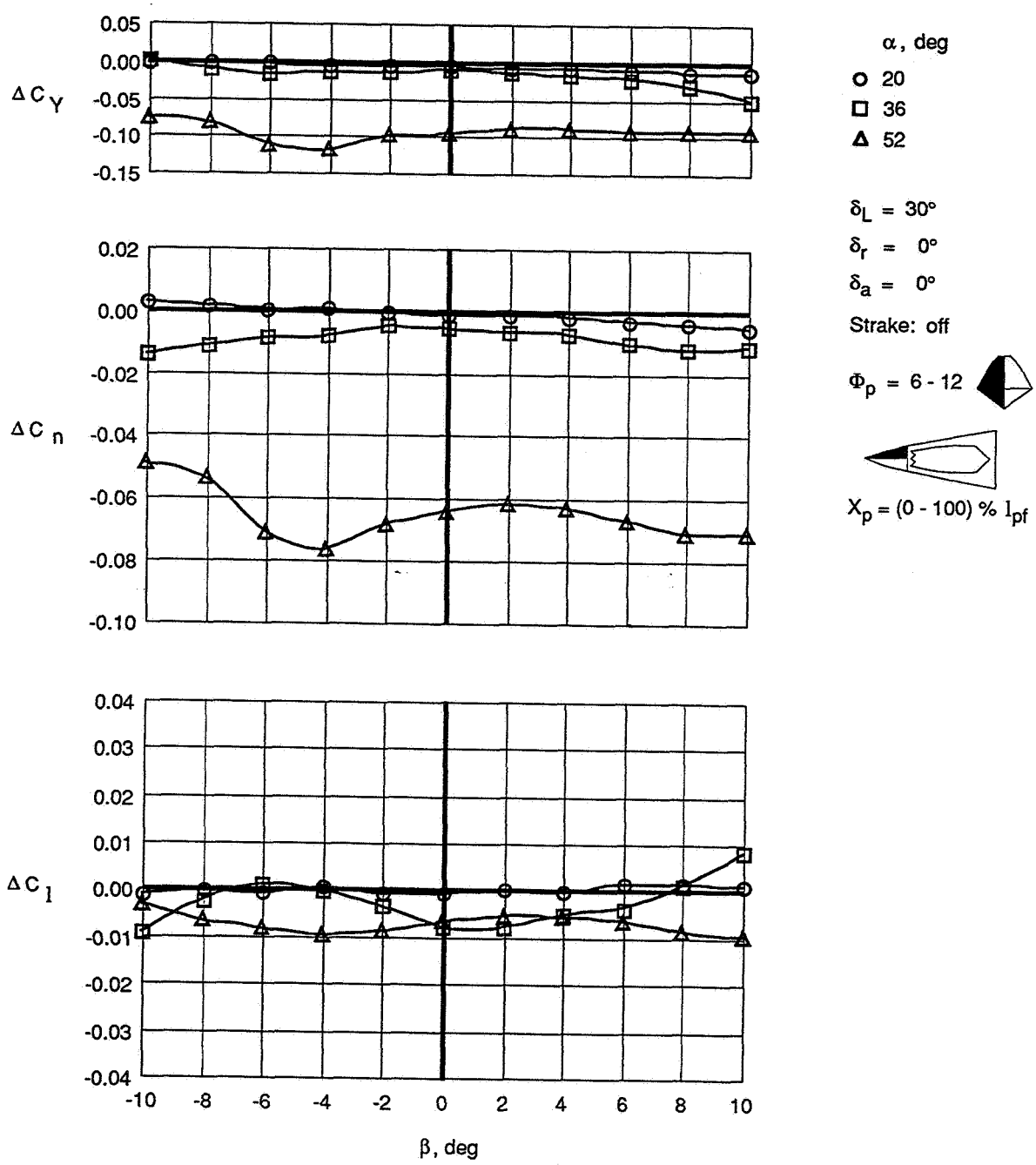

Figure 36. Effect of sideslip on effectiveness of Φ_p=6-12 configuration.

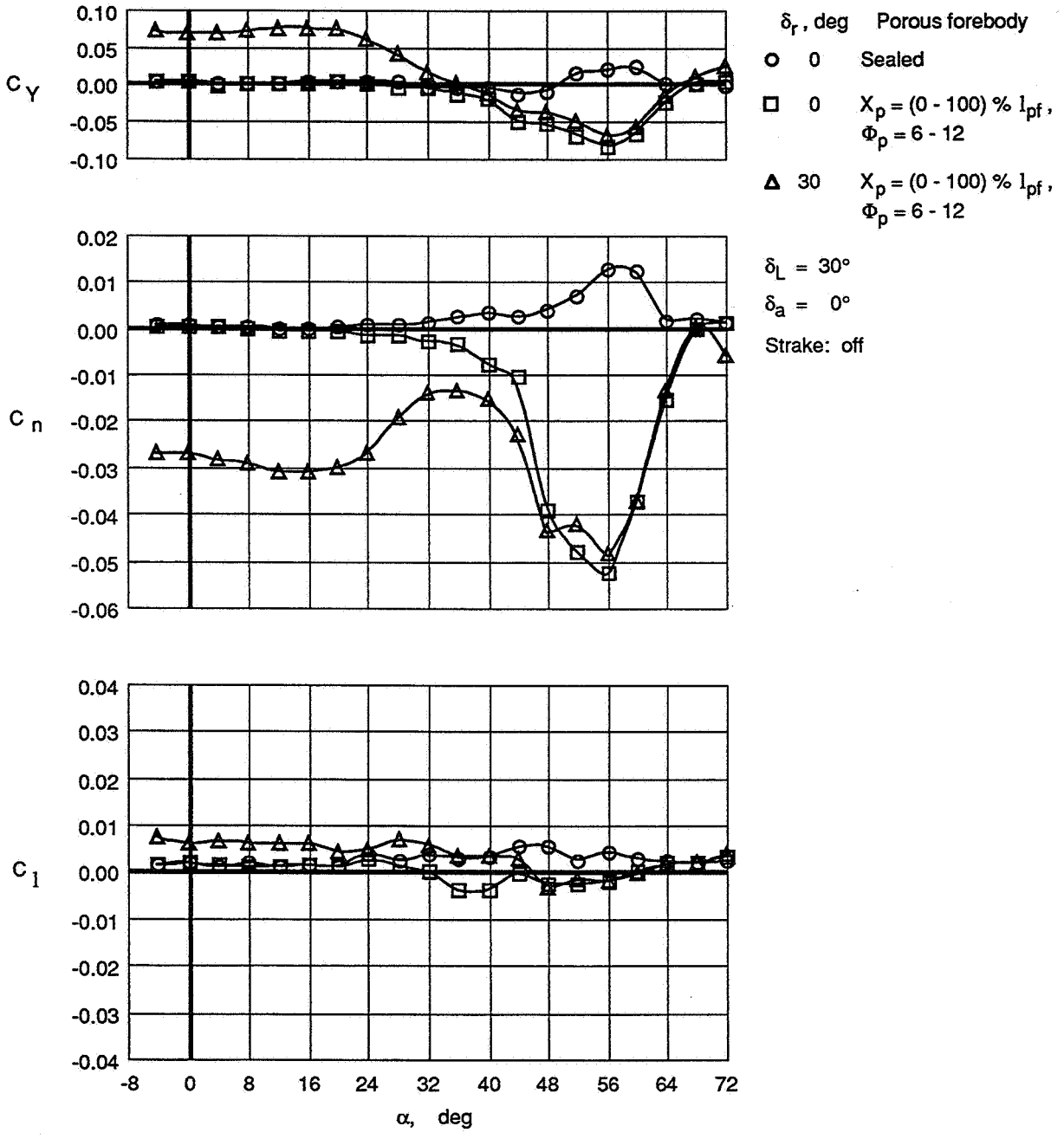

Figure 37. Total yaw-control effectiveness available from both rudder and porous forebody.

REPORT DOCUMENTATION PAGE

Form Approved
OMB No. 0704-0188

1. AGENCY USE ONLY *(Leave blank)*	2. REPORT DATE	3. REPORT TYPE AND DATES COVERED
	August 1995	Contractor Report

4. TITLE AND SUBTITLE
Low-Speed Wind-Tunnel Investigation of a Porous Forebody and Nose Strakes for Yaw Control of a Multirole Fighter Aircraft

5. FUNDING NUMBERS
C NAS1-19000
WU 505-68-30-01

6. AUTHOR(S)
Scott P. Fears

7. PERFORMING ORGANIZATION NAME(S) AND ADDRESS(ES)
Lockheed Engineering & Sciences Company
144 Research Drive
Hampton, VA 23666

8. PERFORMING ORGANIZATION REPORT NUMBER

9. SPONSORING / MONITORING AGENCY NAME(S) AND ADDRESS(ES)
National Aeronautics and Space Administration
Langley Research Center
Hampton, VA 23681-0001

10. SPONSORING / MONITORING AGENCY REPORT NUMBER
NASA CR-4685

11. SUPPLEMENTARY NOTES
Langley Technical Monitor: Dana J. Dunham
Final Report

12a. DISTRIBUTION / AVAILABILITY STATEMENT
Unclassified - Unlimited
Subject Category 08

12b. DISTRIBUTION CODE

13. ABSTRACT *(Maximum 200 words)*

Low-speed wind-tunnel tests were conducted in the Langley 12-Foot Low-Speed Tunnel on a model of the Boeing Multirole Fighter (BMRF) aircraft. This single-seat, single-engine configuration was intended to be an F-16 replacement that would incorporate many of the design goals and advanced technologies of the F-22. Its mission requirements included supersonic cruise without afterburner, reduced observability, and the ability to attack both air-to-air and air-to-ground targets. So that it would be effective in all phases of air combat, the ability to maneuver at angles of attack up to and beyond maximum lift was also desired. Traditional aerodynamic yaw controls, such as rudders, are typically ineffective at these higher angles of attack because they are usually located in the wake from the wings and fuselage. For this reason, this study focused on investigating forebody-mounted controls that produce yawing moments by modifying the strong vortex flowfield being shed from the forebody at high angles of attack. Two forebody strakes were tested that varied in planform and chordwise location. Various patterns of porosity in the forebody skin were also tested that differed in their radial coverage and chordwise location. The tests were performed at a dynamic pressure of 4 lb/ft2 over an angle-of-attack range of -4° to 72° and a sideslip range of -10° to 10°. Static force data, static pressures on the surface of the forebody, and videotapes of flow-visualization using laser-illuminated smoke were obtained.

14. SUBJECT TERMS
High Angle of Attack; Yaw Control; Nose Strakes; Forebody Skin Porosity
Stability and Control; Fighter Aircraft

15. NUMBER OF PAGES
89

16. PRICE CODE
A05

17. SECURITY CLASSIFICATION OF REPORT	18. SECURITY CLASSIFICATION OF THIS PAGE	19. SECURITY CLASSIFICATION OF ABSTRACT	20. LIMITATION OF ABSTRACT
Unclassified	Unclassified		